

# Full Spectrum Ultrahigh Efficiency Photovoltaics: System Design, Integration, and Characterization

Thesis by  
Cristofer Addison Flowers

In Partial Fulfillment of the Requirements for the  
degree of  
Doctor of Philosophy in Chemical Engineering

The logo for the California Institute of Technology (Caltech), featuring the word "Caltech" in a bold, orange, sans-serif font.

CALIFORNIA INSTITUTE OF TECHNOLOGY  
Pasadena, California

2017  
Defended 11 January 2017

© 2017

Cristofer Addison Flowers  
ORCID: 0000-0001-7864-3629

All rights reserved

## ACKNOWLEDGEMENTS

The information, data, or work presented herein was supported in part by the Advanced Research Projects Agency-Energy (ARPA-E), U.S. Department of Energy, under Open 2012 Award Number DE-AR0000333. The author would like to thank the Dow Chemical Company for funding through the University Partnership Program.

## ABSTRACT

The sun is an immense source of power, radiating more energy than all known non-renewable reserves onto the Earth every year in the form of sunlight. In spite of this abundant availability, photovoltaic electricity conversion provides less than 1% of the of the global energy consumption. This lack of deployment is largely a consequence of the cost of photovoltaics relative to other technologies, but increased efficiency is a strong driver for cost reduction due to its ability to impact both photovoltaic module and balance of systems costs. In this thesis, we present enabling technologies for achieving increased efficiency and energy yield for photovoltaic conversion of sunlight. First, we develop finite element cell modeling and electrical contact optimization tools. These models are used to deploy unconstrained optimization techniques that expand the design space of solar cell contacts. Additionally, constrained optimization techniques are used to design solar cell electrical contacts for lateral spectrum-splitting photovoltaic submodules. The lateral spectrum-splitting submodule uses a series of filters to divide broadband sunlight into seven wavelength bands, sending each onto a solar cell with bandgap chosen to minimize thermalization and sub-bandgap transmission losses. By employing a holistic design model covering limiting efficiency, material constraints, optical ray tracing, and electrical modeling, we generate designs capable of ultrahigh (>50%) efficiency. We then design, integrate, and prototype the first photovoltaic converter with seven unique bandgaps. Characterization of this prototype and its constituent components shows an integrated 84.5% optical efficiency and 30.2% submodule efficiency. The exemplary optical performance highlights the promise of the design with further development of the cells. Finally, we develop module circuit and power combination topologies that enable independent electrical connection to two or more subcells in a multijunction photovoltaic converter. This circuit architecture enables independent power production from each device, which reduces the module sensitivity to diurnal and seasonal spectral changes and increases panel annual energy yield. The photovoltaic technologies developed herein often break with convention and demonstrate a feasible pathway to very high (>40%) and ultrahigh (>50%) efficiency modules.

## PUBLISHED CONTENT AND CONTRIBUTIONS

- [1] C. A. Flowers\*, J. V. Lloyd\*, C. N. Eisler, S. Darbe, P. Espinet-Gonzalez, and H. A. Atwater, “A spectrum-splitting photovoltaic submodule with seven independent junctions and 84% optical efficiency,” *In preparation*, 2017, C.A.F participated in the conception of the project, performed the optical and system prototyping and characterization, and is co-authoring the manuscript with J.V.L.
- [2] C. N. Eisler, C. A. Flowers, E. C. Warmann, J. Lloyd, P. Espinet-Gonzalez, S. Darbe, M. Dee, M. Escarra, E. D. Kosten, W. Zhou, and H. A. Atwater, “The polyhedral specular reflector: A spectrum-splitting multijunction design to achieve ultrahigh (>50%) solar module efficiency,” *In preparation*, 2016, C.A.F participated in the conception of the project, performed the electrical simulations, contributed writing, and edited the manuscript.
- [3] E. C. Warmann, C. A. Flowers, J. Lloyd, C. N. Eisler, M. D. Escarra, and H. A. Atwater, “Energy production advantage of independent subcell connection for multijunction photovoltaics,” *Energy Science & Engineering*, submitted, C.A.F. contributed electrical simulations, a resistive loss approach to refining the paper models, prepared accompanying equations and figures, and edited the manuscript.
- [4] C. A. Flowers, C. N. Eisler, and H. A. Atwater, “Electrically independent sub-circuits for a seven-junction spectrum splitting photovoltaic module,” in *2014 IEEE 40th Photovoltaic Specialist Conference (PVSC)*, Jun. 2014, pp. 1339–1343. DOI: 10.1109/PVSC.2014.6925165, C.A.F. participated in the conception of the project, designed the module electrical architecture, performed contact optimization and module electrical simulations, and prepared the manuscript.
- [5] C. A. Flowers, S. Darbe, C. N. Eisler, J. He, and H. A. Atwater, “Positional irradiance measurement: Characterization of spectrum-splitting and concentrating optics for photovoltaics,” in *High and Low Concentrator Systems for Solar Energy Applications IX*, A. P. Plesniak and C. Pfefferkorn, Eds., Proceedings of SPIE, vol. 9175, Bellingham, WA: SPIE, 2014, 91750F-1–91750F-9. DOI: 10.1117/12.2062245, C.A.F participated in the conception of the project, built the measurement system, acquired and analyzed the data, and authored the manuscript.

## TABLE OF CONTENTS

Acknowledgements . . . . .	iii
Abstract . . . . .	iv
Published Content and Contributions . . . . .	v
Table of Contents . . . . .	vi
List of Illustrations . . . . .	viii
List of Tables . . . . .	x
Nomenclature . . . . .	xi
List of Symbols . . . . .	xii
Chapter I: Introduction . . . . .	1
1.1 Fundamental principles of solar cell operation . . . . .	2
1.2 Detailed balance limiting efficiency . . . . .	5
1.3 Multijunction photovoltaics . . . . .	7
1.4 State of the art multijunction photovoltaics . . . . .	9
1.5 Thesis overview . . . . .	10
Chapter II: Three dimensional distributed circuit modeling of solar cells . . . . .	12
2.1 Details of the electrical simulations . . . . .	13
2.2 Extracting series resistance parameters to refine modified detailed balance modeling . . . . .	18
2.3 Optimizing contacts for a prototype spectrum splitting photovoltaic . . . . .	20
2.4 Unconstrained optimization of top contact geometry using a genetic algorithm . . . . .	23
Chapter III: Wholistic system design and modeling of spectrum splitting photovoltaics . . . . .	27
3.1 Modified detailed balance . . . . .	28
3.2 Optical efficiency . . . . .	28
3.3 Bandgap selection . . . . .	29
3.4 Optical Design . . . . .	32
3.5 Electrical Design . . . . .	39
3.6 Thermal modeling . . . . .	53
Chapter IV: Component prototyping and integration for spectrum splitting photovoltaic submodules . . . . .	59
4.1 Polyhedral specular reflector submodule with 100× light pipe con- centrators . . . . .	59
4.2 Optics prototyping and integration . . . . .	61
4.3 Cell processing and mounting . . . . .	63
4.4 Circuit and mechanical component design and prototyping . . . . .	64
4.5 Submodule prototype integration . . . . .	68
4.6 Concluding remarks . . . . .	69
Chapter V: Characterization of spectrum splitting photovoltaic submodules . . . . .	72

5.1	Optoelectronic characterization system . . . . .	72
5.2	Performance of spectrum-splitting and concentrating optics . . . . .	77
5.3	PSR submodule current collection . . . . .	79
5.4	Power production and efficiency . . . . .	82
5.5	Opportunities for efficiency enhancement . . . . .	85
5.6	Conclusion . . . . .	87
Chapter VI: Design of an independently electrically connected spectrum splitting photovoltaic module . . . . .		88
6.1	Introduction . . . . .	88
6.2	Methods . . . . .	90
6.3	Results and Discussion . . . . .	91
6.4	Conclusions . . . . .	96
Chapter VII: Conclusions . . . . .		97
Bibliography . . . . .		100
Appendix A: Positional irradiance measurement: characterization of spectrum-splitting and concentrating optics for photovoltaics . . . . .		108
A.1	Introduction . . . . .	109
A.2	Experimental . . . . .	109
A.3	Results and discussion . . . . .	111
A.4	Conclusions . . . . .	117

## LIST OF ILLUSTRATIONS

<i>Number</i>	<i>Page</i>
1.1 Photovoltaic system costs in 2015 . . . . .	2
1.2 Optoelectronic processes in semiconductors . . . . .	3
1.3 Current-voltage performance curves . . . . .	4
1.4 AM1.5D solar spectrum and limiting efficiency . . . . .	6
1.5 Energetic and entropic losses in a solar cell . . . . .	7
1.6 Multijunction solar cell architectures . . . . .	8
2.1 Solar cell schematic . . . . .	13
2.2 Solar cell equivalent circuit . . . . .	14
2.3 Inverted square contact geometry examples . . . . .	15
2.4 Three-dimensional distributed circuit model of a solar cell. . . . .	15
2.5 Optimized solar cell lumped series resistance . . . . .	19
2.6 Binary representation of cell contact geometry . . . . .	24
2.7 Contact geometries optimized by genetic algorithm . . . . .	25
2.8 Performance of genetic optimization . . . . .	26
3.1 Polyhedral specular reflector submodule schematics . . . . .	33
3.2 PSR filter allocation to each subcell . . . . .	35
3.3 Contactless device efficiency landscape . . . . .	42
3.4 Trimmed PSR contactless device efficiency . . . . .	43
3.5 Simulated module efficiency with optimized contact grids. . . . .	51
3.6 COMSOL PSR simulation geometry . . . . .	55
3.7 PSR surface temperature map . . . . .	55
3.8 PSR subcell temperature rise in operation . . . . .	56
3.9 PSR cooling air velocity map . . . . .	57
3.10 PSR surface temperature map . . . . .	57
3.11 PSR subcell temperature rise in operation . . . . .	58
3.12 PSR cooling air velocity map . . . . .	58
4.1 Polyhedral specular reflector representations . . . . .	62
4.2 AR-coated subcell reflection . . . . .	65
4.3 Submodule printed circuit board . . . . .	66
4.4 Light pipe-to-subcell attachment holder . . . . .	67
4.5 Light pipe-to-filter stack attachment holder . . . . .	67

4.6	Subcell aligned to light pipe . . . . .	69
4.7	Attaching subcell to light pipe . . . . .	70
4.8	Attaching light pipe to filter stack . . . . .	71
5.1	Optical characterization system schematic . . . . .	73
5.2	Optical characterization uncertainty . . . . .	74
5.3	Performance of PSR optical components . . . . .	78
5.4	PSR submodule current collection . . . . .	80
5.5	Optimized contact geometry for GaAs-based subcells . . . . .	80
5.6	PSR submodule current-voltage characteristics . . . . .	83
5.7	Niobate antireflection coating performance . . . . .	86
6.1	PSR submodule with circuit schematics . . . . .	89
6.2	Module circuit efficiency versus lumped series resistance . . . . .	93
6.3	Subcell contact resistive loss contributions . . . . .	94
6.4	Module circuit efficiency with extended design space . . . . .	95
A.1	Positional irradiance measurement system solid model. . . . .	110
A.2	Schematics of various spectrum splitting submodule optics characterized by PIMS. . . . .	111
A.3	Diffraction efficiency of a transmission hologram. . . . .	112
A.4	Theoretical and measured transmission of dichroic filters in air. . . . .	113
A.5	Aspheric lens spectral transmission versus focal length. . . . .	116

## LIST OF TABLES

<i>Number</i>	<i>Page</i>
2.1 Elementary unit cell parameter definitions for the 3D distributed circuit model . . . . .	17
2.2 Bandgap-dependent parameters used in elementary unit cell parameter calculations . . . . .	17
2.3 Bandgap-independent parameters used in elementary unit cell parameter calculations . . . . .	18
2.4 Prototype PSR bandgaps and photocurrent density . . . . .	21
2.5 Prototype PSR optimized contact parameters . . . . .	22
3.1 Optimized bandgaps and suggested III-V alloys . . . . .	30
3.2 Modified detailed balance efficiency with 7 subcells . . . . .	32
3.3 Point Design Cases for Module Efficiency Prediction . . . . .	44
3.4 Submodule interconnection circuit resistive loss contributions . . . . .	46
3.5 Module interconnection circuit topology parameters using DC-DC converters . . . . .	49
4.1 PSR prototype submodule design specifications . . . . .	61
4.2 Subcell anti-reflection coating properties . . . . .	64
5.1 Optimized contact geometry parameters . . . . .	81
5.2 PSR submodule experimental cell performance parameters . . . . .	84
6.1 Module interconnection circuit topology parameters using microinverters . . . . .	92

## NOMENCLATURE

- AM1.5D** Air mass 1.5 direct reference solar spectrum, which corresponds to the irradiance at the Earth's surface within  $3^\circ$  of the solar disk that has passed through 1.5 times the absorption length of a normal incidence atmosphere
- ARC** Anti-reflection coating
- BOS** Balance of systems
- busbar** a central current conductor designed to carry current from a number of smaller conductors over a short distance
- CPC** Compound parabolic concentrator
- DUT** Device under test
- EQE** External quantum efficiency, a measure of a solar cell's current collection efficacy as a function of wavelength; also called IPCE
- ERE** External radiative efficiency, the probability that the recombination of an electron hole pair emits a photon that is emitted to the exterior of the solar cell; also called  $\eta_{\text{ext}}$
- IPCE** Incident photon-to-current efficiency; also called EQE
- LCOE** Levelized cost of electricity
- MOCVD** Metal organic chemical vapor deposition
- MPPT** Maximum power point tracking
- PCB** Printed circuit board
- PDMS** Polydimethylsiloxane, a silicone elastomer with excellent optical transmission for thicknesses  $< 1$  cm
- PIMS** Positional irradiance measurement system
- PMMA** Poly(methyl methacrylate)
- PSR** Polyhedral specular reflector
- SMU** Source measure unit instrument for simultaneously sourcing and measuring current and voltage
- submodule** The minimum tileable sub-unit of optics and cells comprising a photovoltaic module

## LIST OF SYMBOLS

$A$	area	$\text{m}^2$
$C$	optical concentration	suns
$C_p$	heat capacity at constant pressure	$\text{J kg}^{-1} \text{K}^{-1}$
$c$	speed of light in vacuum, $2.998 \times 10^8$	$\text{m s}^{-1}$
$D_x$	diffusivity of species $x$	$\text{m}^2 \text{s}^{-1}$
$\eta$	efficiency	
$\eta_{ext}$	external luminescence efficiency (ERE)	
$E$	energy	eV
$E_g$	semiconductor bandgap	eV
$e$	Euler's number, 2.718	
$\mathbf{F}$	body force tensor	Pa
$FF$	fill factor	
$f_x$	fraction of quantity $x$	
$h = (2\pi) \hbar$	Planck's constant, $4.135 \times 10^{-15}$	eV s
$I$	electrical current	A
$\mathbf{I}$	identity tensor	
$J$	electrical current density	$\text{A m}^{-2}$
$J_0$	electrical recombination current density prefactor	$\text{A m}^{-2}$
$k$	extinction coefficient	
$\mathbf{k}$	thermal conductivity	$\text{W m}^{-1} \text{K}^{-1}$
$k_B$	Boltzmann coefficient, $8.617 \times 10^{-5}$	eV $\text{K}^{-1}$
$\lambda$	wavelength	m
$L_x$	diffusion length of species $x$	m
	length in $x$ direction	m
$l$	length	m
$\mu$	dynamic viscosity	Pa s
$n$	refractive index	
	diode ideality factor	
$n_x$	carrier concentration of type $x$	$\text{m}^{-3}$
	number of species $x$	
$N$	particle flux	$\text{m}^{-2} \text{eV}^{-1}$
$N_x$	number density of species $x$	$\text{m}^{-3}$
	number of subcells electrically connected in $x$ configuration	

$P$	power	W
	perimeter length	m
$p$	pressure	Pa
$Q$	volumetric heat generation rate	$\text{W m}^{-3}$
$q$	electron charge, $1.602 \times 10^{-19}$	C
$\rho$	density	$\text{kg m}^{-3}$
$\rho_x$	resistivity of component $x$	$\Omega \text{ m}, \Omega \text{ m}^2$
$R$	optical reflection	
	electrical resistance	$\Omega$
$r_x$	series resistance area product of component $x$	$\Omega \text{ m}^2$
$T$	optical transmission	
	temperature	K
$t$	time	s
	thickness	m
$\mathbf{u}$	fluid velocity	$\text{m s}^{-1}$
$V$	voltage	V
$W$	bandgap voltage offset	V
$w$	width	m
$X^{DB}$	detailed balance predicted value of quantity $X$	[ $X$ ]

## *Chapter 1*

### INTRODUCTION

Global power consumption in 2012 totaled 18.4 TW, and demand is predicted to rise by 48% to 27.3 TW by 2040 [1]. This level of consumption is dwarfed by the constant flux of photons reaching the Earth’s surface, which totals  $1.7 \times 10^5$  TW [2]. Moreover, the entrained energy of sunlight in a single year far exceeds the cumulative energy reserves of all other known energy sources [3]. In spite of this availability, solar power capture and conversion does not yet constitute a significant fraction of global energy generation, amounting to only about 0.6% in the United States (~1% if distributed generation is included) [4], [5].

Photovoltaics, or solar cells, are devices that directly convert incident radiative energy into electrical energy. Since around 2011, photovoltaics have made up the lion’s share of solar power conversion [5], and in 2016 the industry has grown into the largest source of new electricity generation capacity [6]. Additionally, 6.9% of all utility-scale electricity generation in California (~10% including distributed generation) was generated by photovoltaics in 2015 [7]. Despite the significant headway of the industry in the last five years, however, leaders in the field predict significant global market penetration will require another order of magnitude reduction in the levelized cost of electricity [8].

The levelized cost of electricity (LCOE) is a time-valued metric that incorporates the full life cycle costs and power production of an electricity generating source as

$$\text{LCOE} = \frac{\text{Total life cycle costs}}{\text{Total lifetime electricity production}}. \quad (1.1)$$

Current estimates for the United States place solar between 6.6–12.6 ¢/kWh for new utility scale plants going into service in 2022, with a need to reach as low as 1–2 ¢/kWh to exceed 30% market penetration [8], [9]. The total lifetime electricity production is directly proportional to the photovoltaic module efficiency, while nearly all of the life cycle costs are independent of the efficiency. Consequently, photovoltaic efficiency is a strong lever for effecting cost reduction of electricity.

We will now make one more point to emphasize the importance of photovoltaic efficiency. Fig. 1.1 shows the cost of an installed solar system in various market segments in 2010, 2015, and projected in 2020. The large reductions in cost achieved

from 2010 to date have been dominated by manufacturing cost reductions in the price of the module, to the point where the module itself constitutes only about a third of the overall system cost. Consequently, further reductions in module cost will have relatively smaller impact on the overall installed system. However, this presents a sizable opportunity for efficiency improvements, which are leveraged across the full system costs. Any improvement in efficiency that adds less to the module cost than the net reduction in balance of systems (BOS) costs will result in a reduction in installed system cost, expanding the market available to photovoltaics.

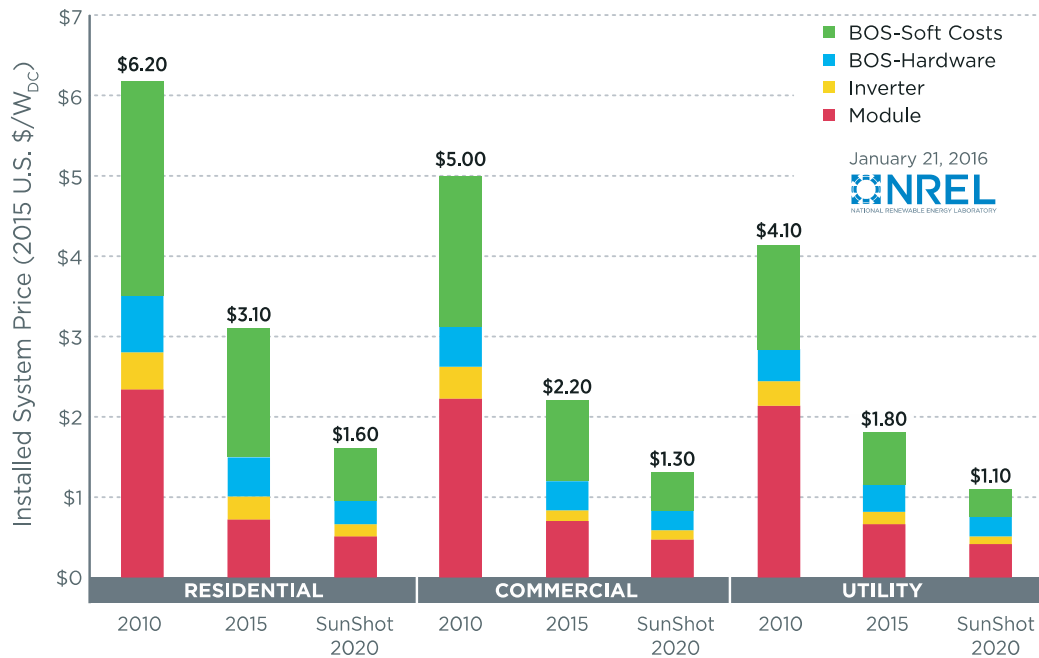


Figure 1.1: Historical, current, and SunShot 2020 target photovoltaic system prices for the utility, commercial, and residential sectors (weighted national average for fixed-tilt systems). Reproduced from [10].

## 1.1 Fundamental principles of solar cell operation

The most prevalent type of photovoltaic device is the single junction solar cell, for which Shockley and Queisser famously described the limiting efficiency in 1961 [11]. This solar cell is composed of a single absorbing semiconductor material in a p-n homojunction configuration and illustrated in energy space in Fig. 1.2. The semiconductor has a valence band of occupied electronic states and a conduction band of unoccupied electronic states separated by a bandgap  $E_g$  over which no electronic states exist. When light is absorbed by the semiconductor, an electron is promoted from a bound state in the valence band to a conducting state in the

conduction band, leaving behind a vacancy quasiparticle in the valence band known as a hole. For a photon to be absorbed and produce these conducting particles, it must have energy greater than or equal to the bandgap of the semiconductor; photons of lower energy are not absorbed. In addition, photons with energy in excess of the bandgap promote electrons to higher energy states, but that excess energy is rapidly lost through electron-phonon coupling, due to crystal lattice vibrations, in a process known as thermalization. The reciprocal process to absorption, known as radiative emission, also occurs, wherein an excited electron in the conduction band can recombine with a hole in the valence band to emit a photon. This photon can be reabsorbed by the cell or emitted back to the environment. In a perfect absorber, all recombination is radiative. However, for realistic materials there exist non-radiative recombination pathways, such as defect-mediated recombination at electronic trap sites or at dangling bonds along the crystal perimeter. These non-radiative mechanisms lack the potential for re-absorption of a photon in the device, and consequently reduce its performance. Therefore, it is advantageous to minimize non-radiative recombination.

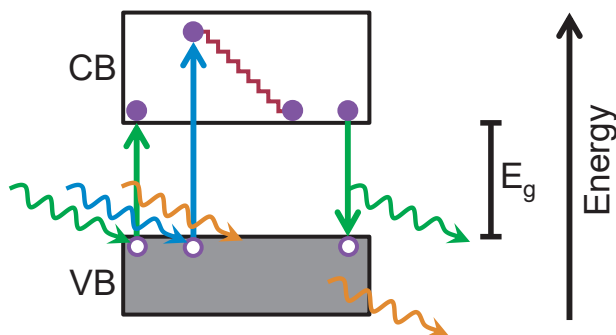


Figure 1.2: Absorption, thermalization, and recombination in a simplified semiconductor band diagram. The cell has a bandgap  $E_g$  equivalent to  $h\nu_{\text{green}}$  and absorbs green and shorter wavelengths of light by promoting an electron (filled circle) from the valence band (VB) to the conduction band (CB). A hole (empty circle) is left behind in the valence band. A blue photon has excess energy beyond the bandgap, and thermalization rapidly transfers that excess to the semiconductor lattice. Additionally, an electron and hole can recombine across the gap, emitting a photon with energy equal to the bandgap energy in the process. An orange photon is not absorbed.

The absorption of light and generation of steady state electron and hole populations builds up an electrochemical potential in the solar cell. This is the cell voltage. The voltage is limited to the bandgap of the solar cell because of the thermalization processes described earlier, and is generally lower in practice. Recombination

is voltage-dependent, and the current density response to applied voltage for an ideal solar cell in the light and dark can be seen in Fig. 1.3. At short circuit, there is zero voltage and electrons can freely flow from the conduction band into the valence band through an external conductor, delivering no power. The short circuit current  $J_{sc}$  directly indicates the absorption efficacy, because each absorbed photon results in one conduction band electron. At open circuit ( $V = V_{oc}$ ), there is no conduction pathway, so recombination processes within the cell must perfectly balance absorption and generation. The  $V_{oc}$  is indicative of the material quality and will be higher for a cell with less non-radiative recombination. Between short circuit and open circuit, the cell produces power equal to the product of the current and the voltage. The efficiency of a solar cell is obtained by dividing the maximum power the cell is capable of generating by the total power in the incident solar spectrum. The fill factor  $FF$  is given by the ratio of the maximum power produced by the cell (dark gray box) to the  $J_{sc} \times V_{oc}$  product (light gray box), and is an indicator of resistive losses and non-radiative recombination.

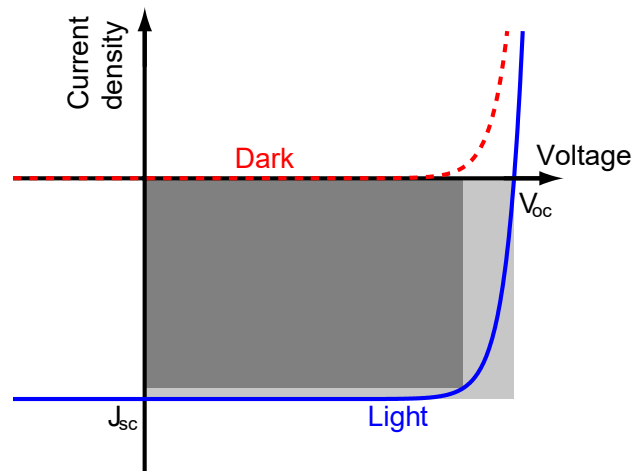


Figure 1.3: Current density-voltage performance curve for an ideal solar cell. Radiative recombination has an exponential voltage dependence, leading to the turn-on of the dark curve at high applied bias. The light curve is a superposition of the absorbed photocurrent and the dark curve. Power is produced in the fourth quadrant of the J-V axes, and the maximum power produced by the cell is indicated by the dark gray area. The open circuit voltage occurs where the light curve crosses the abscissa and indicates that the photocurrent is perfectly balanced by the recombination current. The short circuit current density is equal to the absorbed photocurrent density and is dependent on the semiconductor bandgap.

## 1.2 Detailed balance limiting efficiency

Power conversion by an ideal solar cell is given by the product of the operating current and voltage,

$$P^{\text{DB}}(V) = J^{\text{DB}} \times V = qV \left[ \int_{E_g}^{\infty} N_{\text{incident}}(E) dE - \frac{1}{4\pi^2 \hbar^3 c^2} \int_{E_g}^{\infty} \frac{E^2}{e^{\left(\frac{E-qV}{kT}\right)} - 1} dE \right], \quad (1.2)$$

where  $J$  is given by the difference in the absorbed and emitted photon fluxes and  $N_{\text{incident}}(E)$  is the incident photon flux. This is the equation of detailed balance for a solar cell, so called because the absorbed and emitted fluxes perfectly balance at the open circuit voltage ( $V_{oc}$ ) [11]. It assumes (i) zero sub-bandgap absorption and perfect absorption of above bandgap photons; (ii) infinite carrier mobility such that every absorbed photon results in collected current; and (iii) the only recombination is radiative, as necessitated by thermodynamics. Under these assumptions we can calculate the maximum possible efficiency for a single fixed-bandgap absorber under any incident spectrum. The detailed balance efficiency  $\eta^{\text{DB}}$  is obtained by maximizing  $P^{\text{DB}}(V)$ , as is illustrated schematically in Fig. 1.3, and dividing by the power in the incident solar spectrum,

$$\eta_{\text{incident}}^{\text{DB}} = \frac{P_{\text{max}}^{\text{DB}}}{P_{\text{incident}}} = \frac{J_{\text{max}}^{\text{DB}} V_{\text{max}}}{P_{\text{incident}}}. \quad (1.3)$$

The general expression for efficiency is given by equation 1.3 with the detailed balance indicators removed.

Let us consider maximizing the efficiency of a solar cell in the detailed balance limit. There are competing driving forces for selecting an optimal bandgap because the  $V_{oc}$  increases as the bandgap increases, but the  $J_{sc}$  then decreases. In combination with the spectral profile of the incident illumination, this competition gives rise to an optimal bandgap for a photovoltaic converter. Fig. 1.4a shows the AM1.5D (air mass 1.5 direct) solar spectrum flux. Air mass 1.5 refers to a location at  $37^\circ$  latitude such that sunlight passes through 1.5 equivalent lengths of atmospheric absorption before reaching the Earth's surface. Direct refers to collection of sunlight from within only  $\pm 3^\circ$  of the center of the solar disk, as opposed to the global spectrum which includes the full sky hemisphere. AM1.5D is the appropriate spectrum for cells designed to be integrated with concentrating optics that have a narrow acceptance angle, as is the case for all of the devices that will be developed in this thesis. Under this spectrum, we plot the detailed balance limiting efficiency for a single junction photovoltaic as

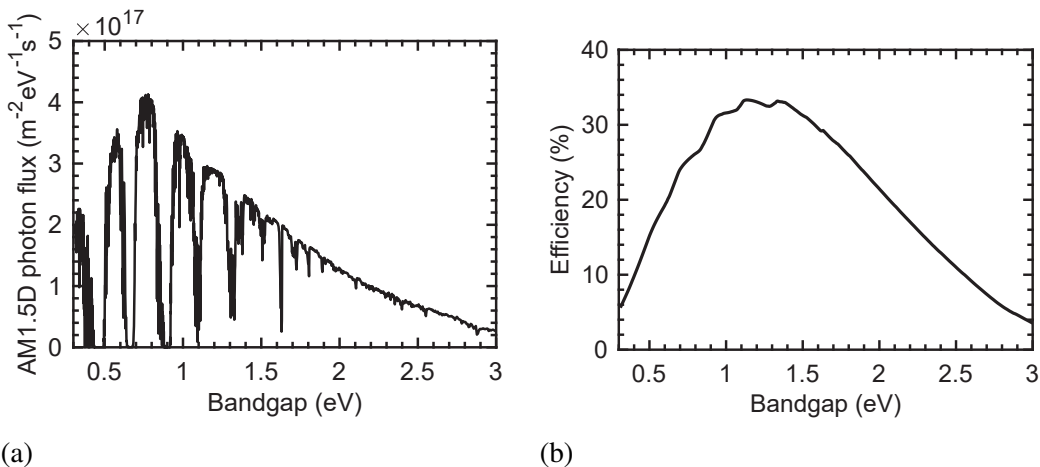


Figure 1.4: (a) Photon flux versus photon energy for the AM1.5D spectrum. Dips correspond to atmospheric absorption bands. (b) Efficiency for an ideal converter under the AM1.5D solar spectrum as a function of bandgap, as calculated by equation 1.2. The peak efficiency is 33.3% at 1.14 eV, and there is a fairly broad plateau of >30% efficiency between 1–1.6 eV.

a function of bandgap. There are multiple peaks owing to the shape of the spectrum, with a maximum efficiency of 33.3% at a bandgap of 1.14 eV.

The current world record single junction photovoltaic cell is a 1.42 eV GaAs solar cell with 28.8% efficiency [12]. It incorporates a high quality mirror at the back of the cell to prevent photons from escaping into the underlying substrate where they cannot be usefully used further. This serves to increase the radiative emission of the cell at open circuit, which necessarily increases the cell operating voltage.

Before we conclude our discussion of single junctions, let us consider briefly how to treat the power production of imperfect devices, such as the champion cell just discussed. We can generalize equation 1.2 to account for non-ideal device performance, for example to account for experimental material quality manifested as sub-unity absorption or the presence of non-radiative recombination pathways for excited carriers.

$$P^{DB}(V, f_{\text{abs}}, \eta_{\text{ext}}, \theta_c, n) = qV \left[ f_{\text{abs}} \int_{E_g}^{\infty} N_{\text{incident}}(E) dE - \frac{1}{\eta_{\text{ext}}} \frac{n^2 \sin^2 \theta_c}{4\pi^2 \hbar^3 c^2} \int_{E_g}^{\infty} \frac{E^2}{e^{\left(\frac{E-qV}{kT}\right)} - 1} dE \right]. \quad (1.4)$$

This version includes the fraction of incident photons absorbed ( $f_{\text{abs}}$ ) and the fraction of radiative recombination ( $\eta_{\text{ext}}$ ), also known as the external radiative efficiency

(ERE) [13] to modify the absorbed and recombined carrier fluxes, respectively. Additionally, the emitted photon flux is reduced by the presence of optical concentration ( $n^2 \sin^2 \theta_c$ ), which reduces the entropy of the emitted flux by confining it to a smaller solid angle. In the case of an ideal flat plate solar cell in air,  $\eta_{ext} = f_{abs} = n = 1$  and  $\theta_c = 90^\circ$  so that we return to the case of equation 1.2.

### 1.3 Multijunction photovoltaics

While experimental devices have already approached the theoretical limit for single junction photovoltaics, much higher efficiencies are possible. Fig. 1.5 shows a breakdown of the energy content in sunlight and its allocation in a single junction solar cell. The performance of the world record single junction is shown in green, balanced by the energetic and entropic losses that make up the remainder of the energetic content of sunlight in yellow and orange, respectively. While losses in the Carnot and Landsberg efficiency limits are unavoidable, there are significant opportunities for drastically increasing photovoltaic efficiency by addressing thermalization of charge carriers to the band edge and transmission of sub-bandgap light with multijunction cells.

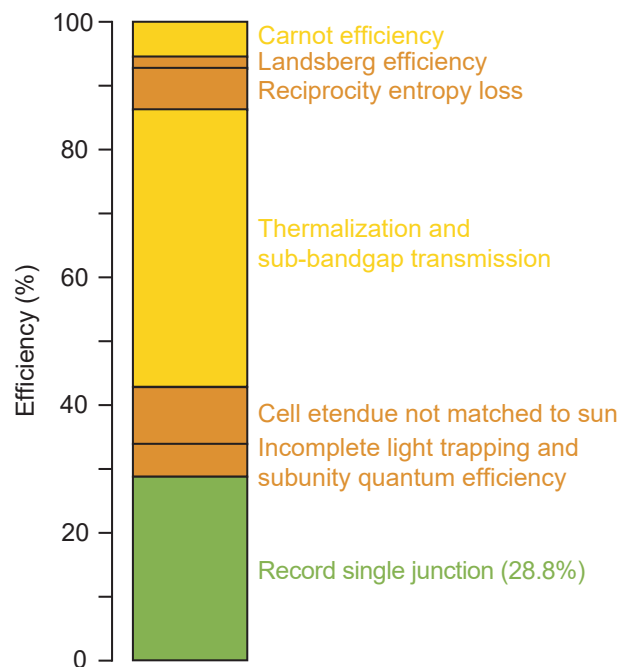


Figure 1.5: Energetic and entropic losses in a solar cell comprising the balance of power in sunlight. Energetic losses and their sources are shown in yellow. Entropic losses and their sources are shown in orange. The current world record single junction cell efficiency (28.8%) is shown in green. Adapted from [14].

Multijunction solar cells are photovoltaics with multiple unique bandgap absorbers, where each absorbs the portion of the solar spectrum between its bandgap and that of the nearest higher bandgap absorber. Thermalization is reduced because on average each photon is absorbed nearer the band edge of its absorber. Sub-bandgap transmission is reduced because absorbers of lower bandgap can be integrated to absorb photons of lower energy than the optimum gap for a single junction under AM1.5D. Moreover, if concentrating optics are used, then the etendue (or angular extent) of light emitted by the cell will more closely match the etendue of light emitted toward the cell by the sun, thus reducing the photon entropy and further increasing the conversion efficiency.

We will now consider two classes of multijunction solar cell. Fig. 1.6a shows a lateral spectrum-splitting multijunction configuration. Each cell is grown and processed independently, and an external optical system (here a cascade of dichroic filters) is used to direct above-bandgap light onto each of the cells.

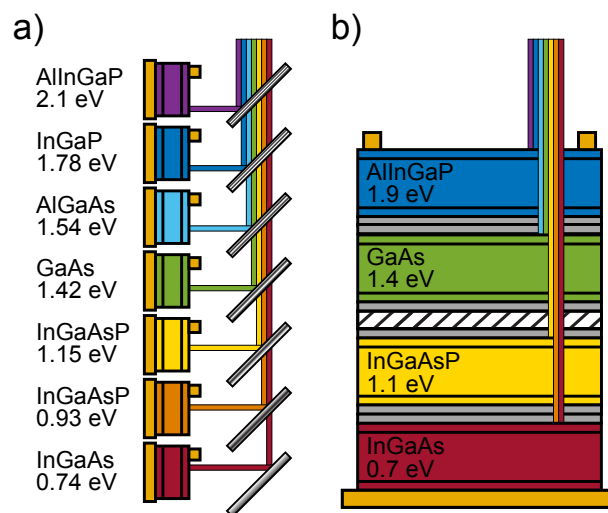


Figure 1.6: (a) Lateral spectrum-splitting and (b) monolithic multijunction device architectures. Bandgap, III–V material alloy, and light absorption is shown for each subcell. Lateral subcells incorporate back mirrors and consequently are half as thick as the monolithic absorbers. Optics divide the incident spectrum onto the lateral subcells, while the monolithic device allocates each spectral band by absorptive filtering. The monolithic architecture is adapted from [15].

Fig. 1.6b shows a schematic of a monolithic multijunction cell. In a monolithic device, all of the bandgaps are integrated sequentially from high to low energy on a common substrate. Light that is incident on the front surface is separated by absorptive filtering; the highest bandgap cell absorbs the highest energy light and transmits

the remaining spectrum to the underlying lower energy absorbers. The junctions are connected in series by a highly doped polarity-switching tunnel junction (shown in gray) that allows the current to tunnel through a sharp energetic barrier and the voltages of each of the junctions sum. This imposes a current-matching constraint between each of the junctions; the current produced by the device is constrained by the junction that produces the least. While this can be designed around under any particular spectrum, diurnal and seasonal variations in the incident solar spectrum lead to lost power production in any practical implementation [16], [17]. In contrast, the lateral spectrum-splitting multijunction has no such current matching constraint as long as the subcells operate electrically independently of one another. Electrical independence can yield an annual power production benefit on the order of 15% relative to a current-matched device [16].

In addition to current matching, monolithic multijunction photovoltaics are constrained by lattice matching. Sequential growth of junctions requires growth at the same lattice spacing in order to minimize the formation of defects that give rise to non-radiative recombination. Growth of disparate lattice constant junctions in the same monolith requires a graded buffer layer to gradually change the lattice constant and internally terminate induced defects [18]. This constrains the bandgaps and number of junctions that can easily be incorporated, and at present state-of-the-art monolithic multijunction cells for concentrator photovoltaic applications consist of four junctions [15], [19]. Lateral spectrum-splitting photovoltaics additionally relax this constraint due to the ability to grow each junction independently. This enables incorporation of an arbitrarily large number of junctions at the expense of increasing cost to manufacture.

Finally, lateral spectrum-splitting multijunctions benefit from improved heat spreading and dissipation due to their physically decentralized layout. Challenges exist in designing the highly efficient optics to allocate photons by wavelength to the appropriate junction and in designing new module circuit architectures to effectively combine and extract power from junctions operating electrically independently of one another.

#### **1.4 State of the art multijunction photovoltaics**

A wide array of lateral spectrum-splitting designs have been proposed [20], [21]. Here, we will focus on only a few notable examples. The lateral spectrum-splitting multijunction of Fig. 1.6a is a simplified schematic of the polyhedral specular re-

flector (PSR), the modeling, design, prototyping, and characterization of which will be the focus of much of this thesis. Record lateral spectrum-splitting multijunctions have incorporated four junctions comprised of one three-junction monolithic subcell and one independent single junction subcell (40.4% submodule efficiency) [22] or two dual-junction monolithic subcells (38.9% minimodule efficiency) [23]. Here a "submodule" is one or more canonical repeat units of optics and cells without the need for environmental sealing required for "module" classification, and a "minimodule" is virtually equivalent to a submodule but with a small ( $<1 \text{ cm}^2$ ) input aperture area. In contrast, we have proposed a design with seven independent single junction devices and will demonstrate designs in excess of 50% submodule efficiency, the "ultrahigh" efficiency regime.

Monolithic multijunctions have likewise achieved exemplary cell and module efficiency. Fig. 1.6b shows the device schematic of the current world record cell achieving 46.0% cell efficiency under  $508\times$  optical concentration, produced by wafer bonding two dual-junction monolithic subcells of disparate lattice constant together into a single monolithic four-junction stack [15]. Similar results (45.6% cell efficiency under  $690\times$  concentration) have been demonstrated in single growth cells with graded buffer layers between lattice-mismatched junctions [19]. The record module efficiency is somewhat lower at 38.9% [24], [25]. This champion module is based on the 46.0% efficient cell technology, but suffers additional losses due to the concentrating optics transmission and misalignment, slight deviations in cell performance across the module, and electrical interconnections.

## 1.5 Thesis overview

The present work is focused around cell, submodule, and module technology modeling, design, prototyping, and characterization in order to enhance the photovoltaic efficiency and facilitate independent electrical operation of lateral spectrum-splitting photovoltaics. In Chapter 2 we describe a 3-dimensional distributed circuit finite element electrical model of a solar cell. The 3D distributed circuit model allows us to optimize the top electrical contact geometry robustly across many concentration levels and geometric shapes, including those generated dynamically via a genetic algorithm. In Chapter 3 we will integrate the 3D distributed circuit model with other device physics, optical, electrical, and thermal modeling tools to wholistically model spectrum splitting photovoltaics capable of ultrahigh ( $>50\%$ ) solar conversion efficiency. Chapter 4 uses the developed model and additional tools to design a polyhedral specular reflector submodule for prototyping and proof-of-concept. It

further details the prototype components and integration processes before Chapter 5 covers the characterization of an integrated prototype and each of its constituent components. The modeled performance is compared to the individual component performance and integrated prototype to identify opportunities for future efficiency enhancement. Chapter 6 expands the field of view from a single submodule to an integrated spectrum splitting module. It describes a module circuit point design to facilitate two-terminal electrical power output where subcells at each bandgap operate electrically independently of all others, thereby enabling the aforementioned boost to annual energy production. Finally, we conclude in Chapter 7 by summarizing these contributions and providing an outlook for future research on lateral spectrum splitting photovoltaics.

**Important note on efficiency**

There are many flavors of efficiency discussed in this text. For consistency, "percentage points" will be used to denote *absolute* solar conversion efficiency scaled against the incident power in a specified reference spectrum, such as AM1.5D. "Percent" or "%" will be used to denote *relative* efficiency numbers. This includes electrical, optical, and relative solar conversion efficiencies, as well as non-efficiency quantities such as current, voltage, and fill factor, among others.

*Chapter 2***THREE DIMENSIONAL DISTRIBUTED CIRCUIT MODELING  
OF SOLAR CELLS**

Balancing accuracy and computational complexity is a substantial challenge when modeling and designing photovoltaic devices. Limiting conversion efficiencies can be rapidly assessed for single junction solar cells as we saw from the detailed balance calculation, but the design space grows exponentially as independent junctions are added. We will investigate this further in §3.3. Translating from a generic converter at a given bandgap to a specific optoelectronic device design requires invoking more complex device physics models, most commonly in the form of charge neutrality (Poisson equation), and the drift-diffusion and continuity equations for electrons and holes. One-dimensional device physics models may be sufficient for design purposes, but they will fail to capture the impact of charge carrier recombination at the crystal edges that becomes increasingly significant for small cells (typically  $<1 \text{ cm}^2$ ). Additionally, spatial variations in light intensity or current collection due to optical elements or the top electrical contact (or electrode) geometry produce a spatially-varying response that requires higher dimensionality device physics equations to accurately model.

In this chapter we are interested in understanding how to model, design, and optimize the solar cell top electrode geometry in the context of concentrating and spectrum splitting optical illumination. To that end, we develop a three-dimensional distributed circuit electrical model of a solar cell that represents the device as a finite element network of fundamental electrical circuit components. This model strikes a balance between achieving sufficiently high spatial resolution to accurately capture the local physics and a short computational time that facilitates use as a flexible design tool, the latter condition of which was not satisfied by three-dimensional device physics solvers. We first describe the model and the contact geometry optimization procedure, and then discuss its application to refining annual energy production predictions made by modified detailed balance calculations, constrained optimization of contact geometry for a prototype spectrum splitting photovoltaic submodule, and unconstrained optimization of top electrode geometry via a genetic algorithm. Additionally, application of the model to broadly designing record efficiency spectrum-splitting photovoltaic submodule receivers will be discussed in

Chapter 3, with additional insights into the model trade-offs presented therein.

## 2.1 Details of the electrical simulations

The typical structure of a single-junction III–V (GaAs) solar cell is illustrated schematically in Fig. 2.1. At the top of the device is a patterned metallic contact,

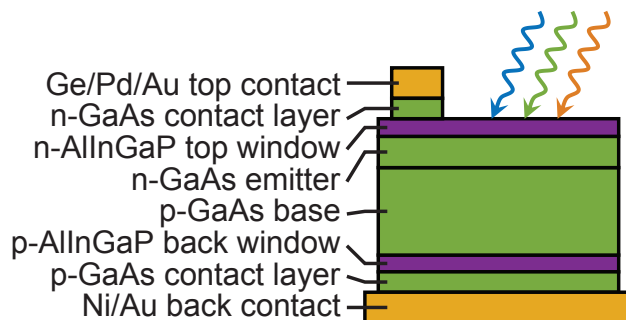


Figure 2.1: Single junction solar cell schematic of device layers, including a planar back contact/mirror for photon recycling and  $\eta_{\text{ext}}$  enhancement.

the primary function of which is to balance collection of charge carriers generated by absorption in the emitter and base layers against the fraction of light reflected by the metallic front surface, also known as shadowing. The top contact layer provides a low interfacial resistance with the metallic top contact. The top window and back surface field layers are generally wide bandgap, minimally absorbing layers that preferentially conduct majority carriers, thereby preventing rapid recombination at dangling bonds at the exposed front surface and at the back contact/semiconductor interface. The  $p$ - $n$  junction lies at the interface of the absorbing emitter and base layers, and electrochemical potential gradients drive each carrier type to the respective metal contact electrode for collection. Some devices additionally incorporate a back contact layer (not pictured) to reduce the interfacial resistance between the back surface field and the back contact, but in many cases this is not necessary.

Additionally, this device has been processed to function off-substrate, and the back contact also serves as a mirror to reflect any non-absorbed or radiatively re-emitted light back into the bulk of the cell. In addition to reducing the thickness of base and emitter needed to absorb all of the incident light, photon recycling within the cell increases the steady state carrier population, thereby driving up the  $V_{oc}$  of the device[26].

Historically, single-junction solar cells have been modeled electrically using a 1-

dimensional double diode model,

$$J = J_L - J_{01} \left\{ \exp \left[ \frac{q(V + Jr_s)}{k_B T} \right] - 1 \right\} - \left[ J_{02b} + J_{02p} \frac{P}{A} \right] \left\{ \exp \left[ \frac{q(V + Jr_s)}{2k_B T} \right] - 1 \right\} - \frac{V + Jr_s}{r_{shunt}}, \quad (2.1)$$

where  $J_L$  is the photocurrent density,  $J_{01}$  is the recombination current density prefactor in the quasi-neutral region,  $J_{02b}$  is the recombination current density prefactor in the depletion region,  $J_{02p}$  is the recombination current density prefactor at the device perimeter,  $r_s$  is the series resistance area product, and  $r_{shunt}$  is the shunt resistance area product. This model is based on the circuit shown in Fig. 2.2, where

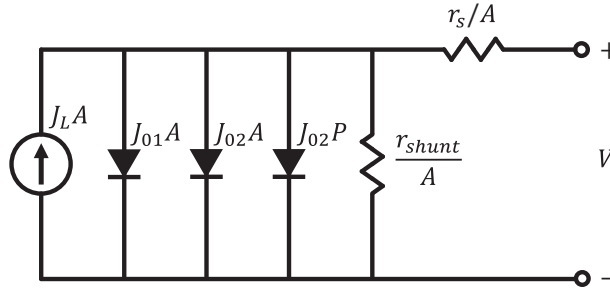


Figure 2.2: Solar cell equivalent double diode circuit including sidewall recombination.

$A$  is the device area and  $P$  is the device perimeter length. Incident sunlight acts as a constant current source balanced by quasi-neutral region recombination ( $J_{01}A$ ), depletion region recombination ( $J_{02b}A$ ), and sidewall recombination ( $J_{02p}P$ ). In addition, shunt pathways can allow current leakage around the junction, and any non-recombining current experiences a lumped series resistance associated with current transport in the semiconductor device layers and through the top electrode contact grid.

For solar cells under concentration, the accuracy of such a model is reduced as it neglects the spatially varying resistance and operating bias of the device. A 3-dimensional distributed circuit model was employed to overcome this limitation.

For the sake of this discussion, we will focus solely on the class of contact geometries known as "inverted square" patterns [27]. This contact geometry heuristic is particularly attractive for solar cells designed for high concentration because it minimizes the current conduction pathway to a high conductivity busbar and has been shown to outperform more traditional linear contact patterns [27]–[31]. Fig. 2.3 shows

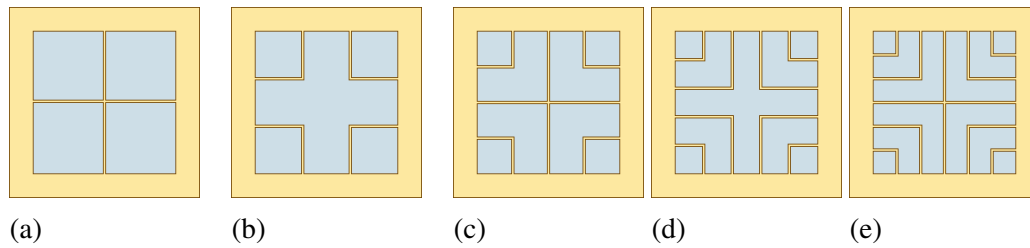


Figure 2.3: Inverted square contact geometry examples with 1, 2, 3, 4, and 5 fingers in (2.3a)-(2.3e), respectively.

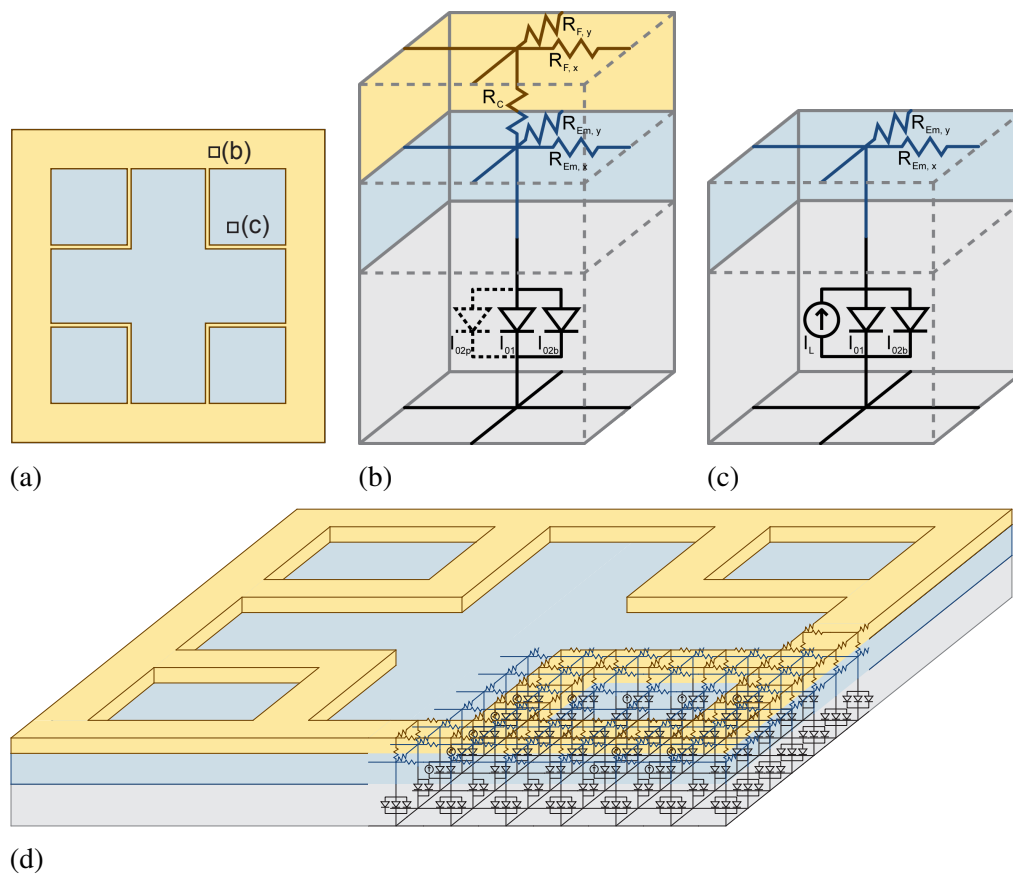


Figure 2.4: Three-dimensional distributed circuit model of a solar cell.

top-down projections of solar cells (blue) contacted with metal (yellow) arranged in each of the five simplest inverted square contact patterns, as quantified by the number of contact finger features. The number of fingers is extracted from the number of unique features that contact any given busbar edge, and in all cases the fingers are assumed to be spaced equidistant from one another to minimize the conduction distance an electron must travel laterally through the semiconductor before being extracted into the metal contact.

In order to develop the 3-dimensional distributed circuit solar cell model, we constrain our focus to the two-finger inverted square contact geometry case, shown again in Fig. 2.4a. In this figure, elementary electrical unit cells representing illuminated and contacted regions in the bulk and at the perimeter of the device are shown in Fig. 2.4b and c, corresponding to the highlighted regions in the contact image. Each elementary unit cell consists of a quasi-neutral recombination diode with ideality of 1, a depletion region recombination diode with ideality of 2, a resistance to lateral conduction in the emitter in the  $x$ -direction, and a resistance to lateral conduction in the emitter in the  $y$ -direction. Additionally, contacted unit cells contain a contact resistance at the metal-semiconductor interface and resistances to lateral conduction in the metal in the  $x$ - and  $y$ -directions. Illuminated unit cells contain a current generation source in parallel with the recombination diodes to represent light absorption in the semiconductor. Lastly, elementary unit cells on the device perimeter contain a perimeter length-dependent perimeter recombination diode with ideality of 2. The parameters associated with each of these elementary circuit units are calculated based on the area of the elementary unit cell according to the formulas in Table 2.1 and the parameters in Tables 2.2 and 2.3.  $\rho_M$  is the contact metal resistivity,  $t_M$  the contact thickness,  $l_x$  the unit cell width,  $l_y$  the unit cell height,  $R_{Em, sheet}$  the emitter (or electron collector) lateral sheet resistance,  $\rho_c$  the front contact resistivity,  $\rho_{bulk}$  the semiconductor bulk resistivity,  $t_{bulk}$  the device thickness,  $L_x$  the cell width,  $L_y$  the cell height, and  $\rho_{bc}$  the back contact resistivity. In general, the photocurrent density is design case dependent. The values reported in Tables 2.2 and 2.3 are for Case 2a with a  $3 \mu\text{m}$  finger size and corresponding shadow loss.

Elementary unit cells are arrayed and interconnected to build up the subcell circuit for simulation, as shown in Fig. 2.4d. In addition, lumped resistances corresponding to conduction through the base and back contact were connected in series with the rear of the subcell. The back contact facilitates lateral transport, so using lumped rather than distributed parameters maintains simulation accuracy while significantly decreasing the computational complexity.

We simulated the contacted subcell electrical performance using the software package HSPICE and optimized the number of inverted square contact fingers [32]. Symmetry was exploited to reduce computational complexity by simulating one quarter of the subcell. A voltage bias was applied between the back contact and the outermost node of the busbar corner and swept to determine each subcell  $I-V$  response curve. The illumination current density is taken from an associated optical

Table 2.1: Elementary unit cell parameter definitions for the 3D distributed circuit model

Parameter (Units)	Formula
Metal lateral resistance ( $\Omega$ )	$R_{f,x} = \rho_M \frac{t_M l_y}{l_x}$ or $R_{f,y} = \rho_M \frac{t_M l_x}{l_y}$
Emitter lateral resistance ( $\Omega$ )	$R_{Em,x} = R_{Em, sheet} \frac{l_x}{l_y}$ or $R_{Em,y} = R_{Em, sheet} \frac{l_y}{l_x}$
Front contact resistance ( $\Omega$ )	$R_c = \frac{\rho_c}{l_x l_y}$
Vertical resistance ( $\Omega$ )	$R_v = \rho_{bulk} \frac{t_{cell}}{L_x L_y}$
Back contact resistance ( $\Omega$ )	$R_{bc} = \frac{\rho_{bc}}{L_x L_y}$
Quasi-neutral recombination current prefactor (A)	$I_{01} = J_{01} l_x l_y$
Depletion recombination current prefactor (A)	$I_{02b} = J_{02b} l_x l_y$
Sidewall recombination current prefactor (A)	$I_{02p} = J_{02p} P = J_{02p} l_x$ or $J_{02p} l_y$ or $J_{02p} (l_x + l_y)$

Table 2.2: Bandgap-dependent parameters used in elementary unit cell parameter calculations

Bandgap (eV)	$R_{Em, sheet}$ ( $\Omega/\square$ )	$J_{01}$ ( $A/m^{-2}$ )	$J_{02b}$ ( $A/m^{-2}$ )	$J_{02p}$ ( $A/m^{-2}$ )	$J_L$ ( $A/m^{-2}$ )
2.13	8191	$1.1 \times 10^{-26}$	$9.5 \times 10^{-12}$	$3.8 \times 10^{-15}$	71.9
1.78	8367	$1.0 \times 10^{-21}$	$3.0 \times 10^{-9}$	$1.2 \times 10^{-12}$	67.3
1.58	3934	$1.6 \times 10^{-19}$	$3.1 \times 10^{-9}$	$1.2 \times 10^{-12}$	47.0
1.42	323	$3.0 \times 10^{-16}$	$2.5 \times 10^{-7}$	$1.0 \times 10^{-10}$	45.2
1.15	3844	$1.5 \times 10^{-11}$	$6.7 \times 10^{-5}$	$2.7 \times 10^{-8}$	83.6
0.94	672	$3.3 \times 10^{-8}$	$2.4 \times 10^{-3}$	$9.7 \times 10^{-7}$	76.0
0.74	86	$4.6 \times 10^{-6}$	$6.8 \times 10^{-3}$	$2.7 \times 10^{-6}$	69.8

simulation with no shadowed area due to an obscuring contact. The shadowed area defined by each optimized contact geometry is then passed back into the optical model to determine a self-consistent efficiency when models are coupled in subsequent Chapter 3.

Table 2.3: Bandgap-independent parameters used in elementary unit cell parameter calculations

Parameter (Units)	Value
$\rho_M$ ( $\Omega \cdot \text{m}$ )	$3.5 \times 10^{-8}$
$\rho_{\text{bulk}}$ ( $\Omega \cdot \text{m}$ )	$2.4 \times 10^{-2}$
$\rho_c$ ( $\Omega \cdot \text{m}^2$ )	$3.7 \times 10^{-10}$
$\rho_{bc}$ ( $\Omega \cdot \text{m}^2$ )	$8.0 \times 10^{-9}$

## 2.2 Extracting series resistance parameters to refine modified detailed balance modeling

The modified detailed balance model presented earlier is a fast computational predictor of realistic subcell performance. Contained within are independent levers for adjusting the  $J_{sc}$  ( $f_{\text{abs}}$ ) and  $V_{oc}$  ( $\eta_{\text{ext}}$ ). However, the model as presented assumes infinite carrier mobility, the relevant effect of which in this context being that no resistive losses are considered. Additionally, it assumes that  $\eta_{\text{ext}}$  is invariant with applied bias, which can only be true for an ideal diode where both radiative and non-radiative recombination occur with an ideality  $n = 1$ . This is an acceptable assumption for high quality III–V solar cells operating in an  $n = 1$  regime spanning the maximum power point and open circuit voltage. However, an independent lever for impacting the device fill factor would lend additional utility to the model.

We used the 3D distributed circuit model to simulate the performance seven single-junction solar cells off-substrate solar cells with backside mirrors. The model was used to optimize the cell top contact geometry under concentrations ranging from 1–1000 suns, incorporating realistic resistive loss and contact grid shadowing. Additionally, a generalized resistance function must be extracted from the distributed circuit simulations in order to generate a useful parameter for incorporation into the computationally fast modified detailed balance calculation. Ideally, the resistance function would be applicable across a range of modeled device materials and concentrations.

A lumped series resistance was identified as a useful parameter to independently modify the cell fill factor. The lumped value was extracted from each of the individual cell simulations as follows: The power loss was summed across all of the resistors in the cell equivalent circuit network. This was set equal to the power loss associated with the current in the full cell area passing through a single lumped

resistor:

$$\sum_{i=1}^N I_i^2 R_i = I_{\text{cell}}^2 R_s. \quad (2.2)$$

Solving for  $R_s$  yields a single parameter that captures the fill factor for any given solar cell optimized for a particular concentration level.

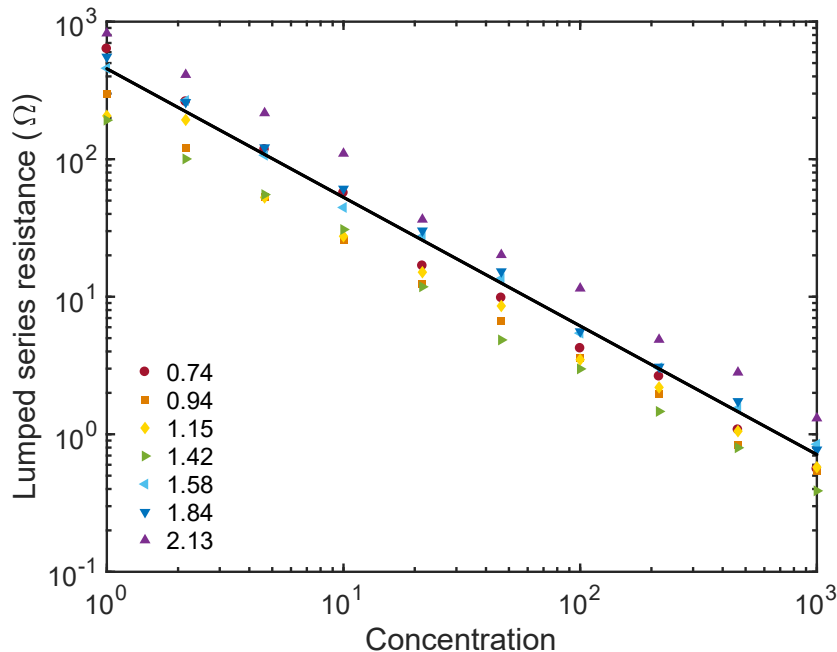


Figure 2.5: Optimized solar cell lumped series resistance as a function of concentration for a 7-subcell spectrum-splitting ensemble. Figure adapted from [33].

Fig. 2.5 shows the lumped series resistance values extracted from a concentration sweep across all seven bandgaps of interest. The contact optimization self-selects for lower series resistance at higher concentration due to the increasing current. This results in the negative slope visible in the data and the fit to the geometric mean, plotted in the solid blue line. The least squares fit to the data geometric mean takes the form

$$R_s(C) = 454C^{0.9352}. \quad (2.3)$$

This fit value can be incorporated into the modified detailed balance calculation by generating the  $I$ - $V$  curve as normal and then subtracting  $\Delta V = I(V)R_s$  from each operating point. Performing this operation yields a predicted performance varying from the optimized value by as much as 12% relative. However, the maximum deviation across the ensemble of subcells is limited to only 2%. This error bound constitutes a meaningful improvement over the modified detailed balance calculation alone.

One previously nonintuitive insight regarding the relative performance of electrically independent and series-connected cell ensembles was gained as a consequence of the resistive loss analysis. It had been obfuscated by the exclusion of any resistive loss in the models comparing the two electrical classes of spectrum-splitting devices. Electrically independent cell ensembles suffer approximately  $n$  times the resistive power loss of a series-connected counterpart, where  $n$  is the number of cells in the ensemble. This is because we are subdividing the power into  $n$  circuits with approximately equal current and resistance  $R_s$ . Consequently,

$$P_{\text{tot}}^{\text{independent}} = \sum_{i=1}^N I_i^2 R_{s,i} \approx NI^2 R_s,$$

whereas for the series connected ensemble, the resistive power loss to the contacts is simply  $I^2 R_s$ .

Finally, let us consider the implications of this insight. We find generally that the presence of these series resistance losses decreases the predicted ensemble efficiency of electrically independent subcells below that of the analogous series-connected ensemble. This is in spite of the superior detailed balance efficiency of electrically independent ensembles originating from superior flexibility in matching bandgaps to the incident solar spectrum. This reemphasizes the unique opportunities of lateral spectrum splitting designs, namely the incorporation of a high reflectivity back mirror for increased photon recycling and  $\eta_{\text{ext}}$ . Additionally, in spite of their lower efficiency, electrically independent ensembles are still expected to yield greater annual electricity production due to their adaptability to changing diurnal and seasonal incident spectra in any given location. This indicates a retention by lateral spectrum splitting photovoltaics of the attractive potential for lower LCOE than concentrating photovoltaics with series-connected absorbers.

### 2.3 Optimizing contacts for a prototype spectrum splitting photovoltaic

In Chapters 3 and 4 we will discuss the design, optimization, and prototyping of spectrum-splitting photovoltaic submodules. Inherent to each of these designs is a contact optimization across a seven subcell ensemble, much like that of §2.2. In this section, we will apply the 3D distributed circuit model to the design of inverted square contact geometries by a hill climbing optimization. We will focus on the optical illumination conditions of the prototype spectrum-splitting photovoltaic of Chapter 4, but note that the method is easily extensible to other optical splitting designs and numbers of subcells, given the availability of suitable materials

parameters.

Each of the subcells in an electrically independent spectrum-splitting photovoltaic submodule has unique illumination intensity and electrical device and materials parameters. The consequence of electrical independence is that each subcell must be independently optimized to balance its unique illumination current, which is linear in the area, with the material-specific resistive losses, which are approximately quadratic in the area ( $P = I^2R$ ). Device input parameters were taken as given in Table 2.2, with the exception of the emitter sheet resistance  $R_{\text{Em, sheet}}$  and the light current density  $J_L$ . The emitter sheet resistance took the value of  $1000 \text{ } \Omega/\square$  uniformly across all subcells, as suggested by our experimental cell grower, Spectrolab, Inc. The expected photocurrent densities in this optical design are listed in Table 2.4. The design assumes a  $1 \text{ mm} \times 1 \text{ mm}$  square illuminated area on a  $1.2 \text{ mm} \times 1.2 \text{ mm}$

Table 2.4: Prototype PSR bandgaps and photocurrent density

Bandgap (eV)	$J_L$ (A/m <sup>2</sup> )
2.10	70.1
1.78	68.1
1.54	47.6
1.42	45.7
1.15	84.6
0.93	76.9
0.74	70.6

active area device with an external busbar, as shown later in Fig. 5.5.

The contact optimization proceeded by the following hill-climbing algorithm:

- (1) Simulate the structure with a finger-less, external busbar-only contact geometry.
- (2) Add a finger in the inverted square configuration, and simulate the performance of the cell with the new contact geometry.
- (3) Check the slope of the  $\eta_{\text{mod}}^{\text{DB}}(n_{\text{fingers}})$  curve.
- (4) Repeat (2) and (3) as long as the slope remains positive.
- (5) Return  $n_{\text{fingers}}$  for the optimum performer when a decrease in efficiency has occurred across at least two consecutive additions of additional fingers.

We chose this simple linear ascent approach because it is increasingly computationally expensive to simulate larger numbers of contact features. Overshooting the optimum by any substantial amount would lead to computational times in excess of the cumulative simulation time of all cases up to the optimal value. An improved algorithm would add a number of contact fingers such that the minimum termination case is simulated, and then refine locally once a change in slope is observed.

Table 2.5: Optimized number of fingers for power conversion in a prototype PSR

$w_f$ ( $\mu\text{m}$ )	<b>Bandgap (eV)</b>						
	2.10	1.78	1.54	1.42	1.15	0.93	0.74
1	5	5	5	5	9	7	9
2	3	5	4	4	5	7	7
3	3	3	3	3	5	5	7
4	3	3	3	3	5	5	6
5	3	3	3	3	5	5	5
6	3	3	3	3	4	5	5
8	1	1	1	1	4	4	5
10	1	1	1	1	3	4	5
25	1	1	1	1	3	3	3
100	0	1	0	0	1	1	1

We list the optimized number of contact fingers as a function of the finger width  $w_f$  and bandgap in Table 2.5. As the finger width decreases, the finger resistance increases and the optimization drives the geometry to a larger number of fingers in order to parallelize the current and reduce resistive losses. Under most conditions, efficiency increases as finger width decreases, and we will expand on this further in §3.5. Contacts employed in the concentrating photovoltaic industry commonly employ a minimum feature size in the 3-10  $\mu\text{m}$  range, though features as small as 1  $\mu\text{m}$  and below are achievable with photolithography [30], [34]–[37]. Since we are interested in prototyping devices in-house, designing broadly across many feature sizes will afford flexibility in actualizing the contacts during subsequent prototyping efforts.

Lastly, we will comment on the areal shadow fraction of the contact geometries. At the largest feature size considered (100  $\mu\text{m}$ ), a single feature constitutes 19% obscuration of the device front surface by metal. This drives several of the subcells

to optimize for zero contact fingers, and for the others constitutes directly a 19% reduction on the maximum achievable efficiency of the submodule. Reducing the finger width to  $25\ \mu\text{m}$  is a substantial improvement, with a power-weighted average shadow fraction of 6.12%. Further shrinking the fingers to  $5\ \mu\text{m}$  reduces the shadowing below 2.5%, which at the design targets considered is equivalent to over 1.5 percentage points of efficiency increase. In summary, we can design optimal contact geometries across a broad range of finger widths, and it is highly advantageous to push the limits of our lithographic capabilities.

#### **2.4 Unconstrained optimization of top contact geometry using a genetic algorithm**

All of the previous sections have described optimizations within the inverted square family of contact geometries. Many other such families exist, ranging from linear patterns to radial networks to sub-wavelength fractal networks [27], [34], [38], [39]. While each of these designs has achieved high performance across one or more class of devices, they are all constrained in their search of the optimization landscape because they prescribe a geometric heuristic. Consequently, we expect an unconstrained optimization of the top contact geometry of a solar cell to uniquely be able to find a global optimum. Additionally, because much of the possible design space has been unexplored previously, this optimum has the potential to outperform devices optimized under a contact geometry heuristic.

We propose to search the design space via genetic algorithm. A genetic algorithm is an optimization algorithm that mimics the biological processes of evolution and natural selection. Evolution is the process of modifying chromosomes in such a way as to impart new features at the point of reproduction, and natural selection is the forcing that causes more fit members of a population to reproduce more frequently than their less fit counterparts [40], where fitness remains to be defined. A chromosome encodes the traits of an individual member of the population, and evolution occurs on the chromosome; natural selection occurs on the individual. As the population moves from generation to generation, traits associated with high fitness are expected to be passed on to new offspring at a high rate, driving the population to superior performance. Additionally, mutation serves to introduce new features into the population that will quickly die out if detrimental or proliferate if advantageous. With random mutation, a genetic algorithm can effectively explore a broad design space and self-select down to a global optimum.

In the present context, the population members are solar cells and their chromosomes encode the geometry of the top contact. We chose to represent the cell by discretizing the input aperture into a square lattice. The location and presence or lack of contact metallization is encoded into a binary array representing each element of the discretized cell lattice. A simplified example can be seen in Fig. 2.6. For a given cell type, this fully defines the cell characteristics and the 3D distributed circuit model can be used to evaluate its performance. The fitness of the contact design is consequently the associated cell efficiency. We note that this relaxes the adherence to any particular design heuristic.

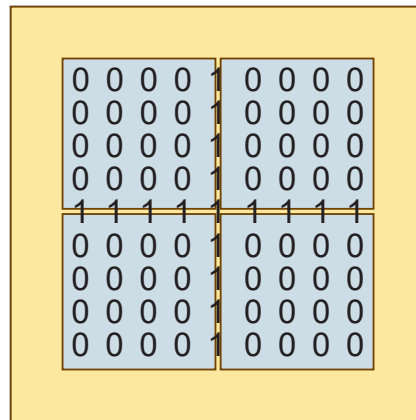


Figure 2.6: Binary representation of a solar cell with a one-finger inverted square contact geometry.

The algorithm proceeds as follows:

- (1) Seed a population of  $N$  members with randomly generated chromosomes.
- (2) Evaluate the fitness of each member of the population.
- (3)
  - (a) With selection probability dependent on the individual fitness, select two individuals from the population to reproduce.
  - (b) Combine aspects of their chromosomes by copying from one parent or the other to the child, switching which parent at each bit for which a normalized randomly generated number is less than the crossover probability.
  - (c) Mutate the offspring chromosome by flipping each bit for which a normalized randomly generated number is less than the mutation probability.
  - (d) Repeat (3a)-(3c) until a new  $N - 1$  members have been generated, replacing the parents into the population each time.

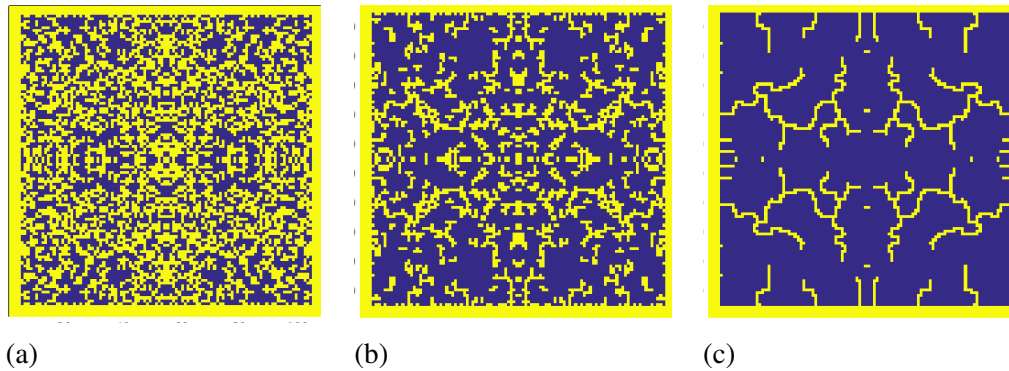


Figure 2.7: Top-down view of the contact geometry for the champion cell in a population after (a) 1, (b) 200, and (c) 1000 generations of genetic optimization.

- (e) Clone the best performing parent into the population of children. This new set of  $N$  members is the subsequent generation.
- (4) Repeat (2)-(3) until a stopping criterion, such as fitness stagnation or a maximum number of simulations has been met.

The progress of the algorithm can be visualized by looking at the contact geometry of the best performing ("champion") individual in any given generation, as well as by tracking the champion and generation average efficiency. Fig. 2.7 shows the champion contact geometry for a representative optimization using the genetic algorithm where our cell is assumed to be  $1 \text{ mm} \times 1 \text{ mm}$  active area and we have discretized it into  $10 \mu\text{m} \times 10 \mu\text{m}$  unit cells. Initially, the contact is a random distribution of metal. After 200 generations, it begins to develop structure, favoring contiguous metal conductors to extract current to the busbar and net removal of metallized area to absorb more of the incident illumination. This is further refined over subsequent generations, culminating in the structure shown in Fig. 2.7c.

The final contact geometry was generated by simulating a population of 64 solar cells for 1000 generations, at which point it terminated. The champion cell developed a contact geometry with many features reminiscent of heuristically designed solar cells: thin contact features extending into the center of the absorbing area and separating approximately equidistantly to minimize conduction length in the semiconductor layer.

Fig. 2.8 shows the efficiency of the champion performer and the population average across the entire optimization. Both efficiencies generally trend upward, with occasional large upticks associated with the introduction of a new feature into the

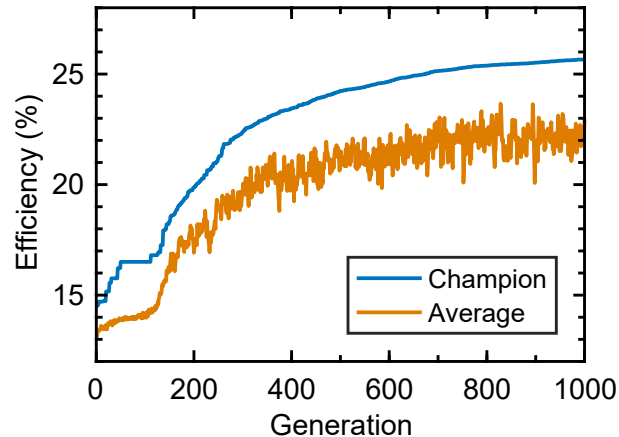


Figure 2.8: Performance progress versus generation number for both the champion performer in each generation and the population average. Each generation consists of 64 cells, where one is the champion performer from the previous round and the remainder were generated by recombination and mutation of chromosomes from the previous generation.

population that leads to rapid improvement. Additionally, the probability of mutation is relatively low, so it becomes difficult in late generation to remove islanded contact metal that likely has minimal beneficial conductance and reflects a not insignificant amount of light. The champion efficiency terminates at 25.7%, which is well below the efficiency of an equivalent cell optimized within heuristic constraints (28.6%) [34].

While we have not yet demonstrated an efficiency improvement relative to conventional contact optimization strategies, the preceding work serves as a demonstration of an unconstrained contact optimization, which to our knowledge has not been previously demonstrated by any approach, genetic or otherwise. Unconstrained optimization opens additional design space up to the photovoltaic device designer, which is crucial in the context of an industry fighting for valuable incremental efficiency gains. We leave changes in approach, including nearly four decades of refinement in the genetic optimization space, as future work and an opportunity to continue pushing the limits of solar energy conversion.

*Chapter 3***WHOLISTIC SYSTEM DESIGN AND MODELING OF  
SPECTRUM SPLITTING PHOTOVOLTAICS**

Comprehensive design of a spectrum splitting photovoltaic receiver requires a multifaceted model to capture the myriad physics occurring within the system. The previous chapter described a detailed model for a solar cell using basic electrical elements to build up a finite element network and recreate cell behavior under a variety of conditions. Further, it enabled optimization of the top contact geometry through successive simulations and local or global optimization algorithms. This cell model is a single piece of a manifold model used in the simulation, design, and optimization of a spectrum splitting receiver for conversion of sunlight into electricity. In addition to the subcell model, tools are needed to select the number and bandgaps of the photovoltaic absorbers; predict the performance of the concentrating and spectrum-splitting optics; predict the limiting performance of cell absorption and power output, especially for cases where there is little precedent for off-substrate devices incorporating a rear mirror; account for electrical and power combination losses when tiling submodules into a module; and predict the operating temperature of each of the subcells under operation. In this chapter we will describe each of these models and how they are integrated to give a comprehensive design tool capable of predicting the performance of a large variety of photovoltaic submodules.

Several of these design components were developed by colleagues Emily Warmann and Carissa Eisler, with additional contributions by John Lloyd and Matthew Escarra. They have been reported in [41] and [42], [43], and are included here for completeness of the model. In particular, much of this content has been prepared for peer-reviewed publication as

E. C. Warmann, C. A. Flowers, J. Lloyd, C. N. Eisler, M. D. Escarra, and H. A. Atwater, "Energy production advantage of independent subcell connection for multijunction photovoltaics," *Energy Science & Engineering*, submitted,

and

C. N. Eisler, C. A. Flowers, E. C. Warmann, J. Lloyd, P. Espinet-Gonzalez, S. Darbe, M. Dee, M. Escarra, E. D. Kosten, W. Zhou, and H. A. Atwater, “The polyhedral specular reflector: A spectrum-splitting multijunction design to achieve ultrahigh (>50%) solar module efficiency,” *In preparation*, 2016,

Personal contributions include numerous discussions regarding optimization approaches spanning all of the physics models; interpolation of the contactless device efficiency space; refinement of interfaces and feedback between various models; and development and implementation of the cell electrical model (Chapter 2), submodule and module electrical models, power conversion model (Chapter 6), and thermal model.

### 3.1 Modified detailed balance

The calculation of modified detailed balance efficiency was described in detail in the Introduction (§1.2). This calculation can be extended to ensembles of many bandgaps by summing the power equation over each cell:

$$\eta_{\text{mod}}^{DB} = \sum_{i=1}^N \eta_{\text{mod},i}^{DB}. \quad (3.1)$$

The modified detailed balance efficiency is used to refine the device bandgap selection, an essential component of the optical efficiency calculation (equation 3.2), and an intermediate merit function for submodule optical designs. Additionally, the modified detailed balance calculation provides the short circuit current density  $J_{sc}$  for the cell electrical model and top contact geometry optimization, as well as the total dissipated power in each subcell for thermal modeling.

### 3.2 Optical efficiency

An important benchmark in considering each of the optical components and coatings in the polyhedral specular reflector is the optical efficiency. We define optical efficiency as ratio of the modified detailed balance ensemble efficiency with as-designed or as-characterized optical performance to the modified detailed balance ensemble efficiency with perfect illumination band allocation,

$$\eta_{\text{optical}} = \frac{\eta_{\text{transmitted}}^{DB}(f_{\text{abs}}, \eta_{\text{ext}}, \theta_c, n)}{\eta_{\text{incident}}^{DB}(f_{\text{abs}}, \eta_{\text{ext}}, \theta_c, n)}, \quad (3.2)$$

such that the total optical efficiency is the product of component optical efficiencies, and the submodule efficiency is the product of the ideal detailed balance efficiency with the total optical efficiency.

### 3.3 Bandgap selection

A spectrum splitting subcell ensemble accrues an efficiency advantage relative to single-junction photovoltaics by reducing (i) the amount of incident energy lost to thermal dissipation of excited carrier energy to the crystal lattice, and (ii) the number of photons below the lowest absorber bandgap that are not absorbed. The selection of optimal bandgaps to minimize these losses results generally in an  $n$ -dimensional optimization over the bandgap energies for an ensemble consisting of  $n$  subcells with unique bandgaps. For monolithic multijunction devices, series connection imposes a current matching constraint between subcells that drastically reduces the design space, making an exhaustive sweep feasible to optimize the ensemble bandgaps [44]. Each proposed ensemble is evaluated via a detailed balance efficiency calculation that simultaneously imposes the current matching constraint between subcells, effectively limiting the current in every subcell to that of the lowest current-producing subcell in the ensemble. Lateral spectrum splitting ensembles have no such constraint, and the design space grows exponentially with the number of subcells in the ensemble. Consequently, the bandgap selection requires a more sophisticated optimization algorithm.

#### Simulated annealing

Simulated annealing is a Monte Carlo probabilistic optimization algorithm that emulates metallurgical annealing and crystallization in order to search a large design space and find a global optimum. Given an initial random seed ensemble of  $n$  bandgaps, a perturbation is applied to each of the bandgap values and accepted as the new basis for further perturbation if the resulting ensemble outperforms the initial state, as determined by the ensemble unmodified detailed balance efficiency. Additionally, a worse performing ensemble can be accepted as a new basis with a probability proportional to the "temperature" of the system, which is necessary to broadly explore the design space. Initially, the "temperature" of the system is high and the bandgaps are allowed to freely vary over a large range and quickly explore a large design space. As the system is "cooled," the probability of accepting a worse solution slowly decreases until it becomes trapped in the vicinity of a local optimum.

The bandgap selection optimization was carried out across two distinct stages of the simulated annealing algorithm. In the early stage of the optimization, thoroughly searching the design space to find the global optimum requires the perturbations of the ensemble bandgaps to be large. Conversely, in the latter stage of the simulation it is desirable to search in the immediate vicinity of the global optimum, which requires

a reduction in the perturbation that is distinct from the probability of accepting an inferior solution. With the optimization proceeding in two distinct steps, Emily was able to repeatably identify the same optimal design for spectrum splitting ensemble bandgaps, which is a necessary but insufficient condition for the identified optimum to be globally optimal. The optimized values for an eight-subcell ensemble are shown in the first column of Table 3.1. We chose to focus on ensembles of  $\geq 7$  subcells due to their ability to produce designs in excess of 50% efficiency when accounting for optical and electrical losses as will be discussed in the following sections.

Table 3.1: Optimized bandgaps and suggested III-V alloys

Optimized $E_g^{\text{DB}}$ (eV)	Lattice matched $E_g^{\text{modDB}}$ (eV)	III–V alloy	Growth wafer	$\eta_{\text{ext}}$ (%)
2.61				
2.13	2.13	$\text{Al}_{0.20}\text{Ga}_{0.32}\text{In}_{0.48}\text{P}$	GaAs	0.19
1.74	1.78	$\text{Ga}_{0.37}\text{In}_{0.63}\text{P}$	GaAs	8 [45]
1.43	1.54	$\text{Al}_{0.1}\text{Ga}_{0.9}\text{As}$	GaAs	3
1.15	1.42	GaAs	GaAs	22.5 [46]
0.94	1.15	$\text{In}_{0.87}\text{Ga}_{0.13}\text{As}_{0.28}\text{P}_{0.72}$	InP	1.2
0.70	0.94	$\text{In}_{0.71}\text{Ga}_{0.29}\text{As}_{0.62}\text{P}_{0.38}$	InP	1.6
0.50	0.74	$\text{In}_{0.53}\text{Ga}_{0.47}\text{As}$	InP	11

The unmodified detailed balance efficiency of equation 1.2 was used in the preceding calculations because it is difficult to prescribe  $\eta_{\text{ext}}$  a priori, which is in general a function of growth process development and material quality. Additionally, the  $\eta_{\text{ext}}$  is dependent on the device design, which is intractable to simulate via device physics models with realistic materials parameters for many of the bandgaps considered because measured values simply do not exist. Moreover, the optimized set of bandgaps included values for which there is little or no precedent of high quality III–V photovoltaic device growth (2.61 eV, 0.50 eV). We chose to use only III–V alloys due to their demonstrated high material quality growth and the possibility of incorporating high photon recycling with the inclusion of a high reflectivity back-side mirror on off-substrate devices [26]. Consequently, the optimal set of bandgaps was modified as follows:

- (1) 2.61 eV and 0.50 eV subcells were eliminated.

- (2) A seventh subcell was added to increase the ensemble efficiency.
- (3) The ensemble was re-optimized with the acceptable bandgap range clamped between 0.7–2.13 eV.
- (4) Each bandgap was minimally shifted to that of the nearest III–V alloy lattice matched to either GaAs or InP.

The choice to select only lattice-matched device compositions was motivated by ease of growth and a desire to minimize crystal defects and avoid lattice-graded buffer layers in order to maximize the  $\eta_{\text{ext}}$  [47].

The final set of bandgaps determined for a seven-junction spectrum splitting photovoltaic are shown in the second column of Table 3.1. Subsequent columns show the alloy composition and the growth substrate to which each can be grown lattice-matched. These compositions were used as the basis for one dimensional device designs and device physics simulations in AFORS-HET [48], which is both free and built expressly for photovoltaics. Realistic doping-dependent lifetime and mobility data were incorporated with each of the modeled subcells in order to optimize the thickness and doping of each of the device layers[49]–[52]. Devices were assumed to be comprised of an off-substrate epitaxial stack with a high reflectivity back reflector. The results of these designs have been previously reported by Warmann [41], [33], and were used to extract  $\eta_{\text{ext}}$  for each of the subcells. The extracted  $\eta_{\text{ext}}$  values are reported in the final column of Table 3.1 with the exception of the 1.78 eV InGaP and 1.42 eV GaAs subcells where experimental values are reported instead. The experimental values of the external radiative efficiency are higher than those predicted by our modeling, indicating a conservative choice of material parameters in the models.

### Limiting efficiency prediction

The EQE for a state-of-the-art GaAs subcell [12] was analyzed to determine that 92% of in-band photons striking the active device area are converted into current. This fraction of ideal absorption  $f_{\text{abs}}$  was taken as a design target and simulation assumption for each of the III–V subcells. Incorporating the  $f_{\text{abs}}$  and  $\eta_{\text{ext}}$  values thus determined into a modified detailed balance calculation yields an efficiency ceiling on any submodule employing this ensemble of bandgaps as a function of only the concentration, and is reported in Table 3.2. Based on the recorded efficiency projections, >50% module efficiency cells should be possible with high quality optics and a high efficiency power conditioning system.

Table 3.2: Modified detailed balance efficiency for a 7-subcell lateral spectrum splitting ensemble

Concentration (suns)	$\eta_{\text{mod}}^{\text{DB}}$ (%)
1	47.2
10	50.3
100	53.4
1000	56.5

### 3.4 Optical Design

After the subcell bandgaps have been designed, the concentrating and splitting optics must be designed and modeled. Any spectrum-splitting photovoltaic submodule design achieving ultrahigh (>50%) efficiency with realistic subcell parameters ( $f_{\text{abs}}$ ,  $\eta_{\text{ext}}$ ) and a tractable number of subcells requires both (i) sufficiently high concentration to elevate the subcell voltages and fill factors, and (ii) a highly efficient method of dividing the incident broadband spectrum into discrete wavelength bands. Though several designs have been considered throughout the duration of this project [53]–[55], we direct our focus here onto the only one to meet both of these criteria across a broad design space: the polyhedral specular reflector (PSR).

#### Polyhedral specular reflector

Fig. 3.1a shows schematics of the polyhedral specular reflector design. It achieves both high concentration and high efficiency by employing a series of multilayer dielectric filters to divide the incident spectrum and two stages of concentration. Incident light enters the primary concentrator, either a hollow, mirrored compound parabolic concentrator (CPC) or an acrylic nonimaging lens. The output of the primary concentrator feeds directly into a solid glass prism with seven longpass filters. The filters are oriented at  $45^\circ$  with respect to the incident light and ordered to sequentially reflect away the highest energy photons. As a result, the incident spectrum is divided into seven bands with the highest energy photons at the top of the prism and the lowest energy photons at the bottom, as shown in Fig. 3.1b. Each spectral band is then further concentrated by a solid glass secondary CPC before it is converted by one of the seven subcells. Depending on the relative sizes of the primary and secondary concentrators, these individual units can pack horizontally in-plane as in Fig. 3.1c or vertically if the length of the secondary concentrators

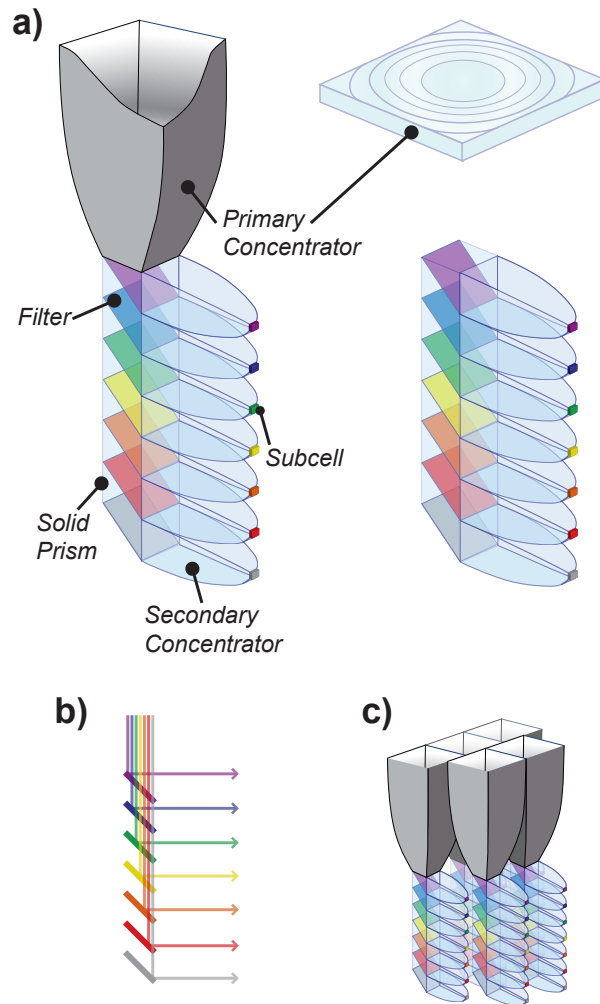


Figure 3.1: (a) Schematics of the polyhedral specular reflector (PSR) submodule. Incident light is divided through reflection and transmission by a series of filters embedded in a solid glass prism. Concentration is achieved in two stages. (b) Schematic of light splitting process of the PSR. Longpass filters sequentially reflect away high-to-low energy light for conversion in the appropriate subcell. (c) Schematic of an example horizontal packing of PSR submodules. Schematics were generated by Carissa Eisler.

cannot be properly accommodated in a planar configuration [56], [57].

### Optical Splitting

The optical splitting components were designed by Carissa Eisler to define the wavelength band allocation of the submodules. The spectrum-splitting filter stack is the most critical optical component of the PSR design because effective division of the solar spectrum is required to prevent misallocation of photons among the subcells

that result in increased thermalization or nonabsorption losses. We designed seven aperiodic dielectric filters using alternating layers of  $\text{SiO}_2$  and  $\text{TiO}_2$  due to their high refractive index contrast and capacity for forming filters with high reflectivity. The number and thicknesses of these layers were optimized in OpenFilters to maximize reflection of photons with energies above the bandgap of the corresponding subcell and minimize reflection of photons with energies below the bandgap [58]. Typically, these filters had a few hundred layers and a total thickness of 20-35  $\mu\text{m}$  [43]. The simulated spectrum-splitting of the as-designed filters at  $45^\circ$  angle of incidence is shown by the solid curves in Fig. 3.2. Excellent division of incident broadband illumination is observed due to the high reflectivity for photons with energies greater than the corresponding subcell bandgap and near-zero reflectivity for longer wavelengths. The percent of incident photons allocated to each subcell band decreases as the wavelength approaches the long wavelength filter cutoff as a result of *s*- and *p*- polarization splitting of the filters. This polarization splitting drove the design to place the cutoff slightly above the subcell bandgap in order to ensure that minimal low energy photons are misallocated to a higher bandgap subcell that cannot convert them. As a consequence, some high energy photons are allocated to lower energy subcells and converted at a lower voltage, which generally harvests 59-98% of the power that would have been captured in the optimal absorber. The dashed lines in Fig. 3.2 show the resulting spectrum-splitting of a fabricated filter stack using a similar design and materials, where  $\text{Ta}_2\text{O}_5$  (filter #1) or  $\text{Nb}_2\text{O}_5$  (remaining filters) was substituted for  $\text{TiO}_2$ . Each filter was deposited by Chroma Technology on a fused silica (Corning HPFS 7980) triangular (filter #1) or parallelepiped (remaining filters) prism via reactive DC sputtering [59]. The change of the high index material used slightly altered the reflectivity profile, resulting in 97% of the design optical efficiency based on  $\text{TiO}_2$ . Additionally, the fused silica substrate has an O-H absorption band near 1400 nm, but this negligibly affects the overall efficiency since atmospheric water vapor has already absorbed this light from the incident solar spectrum. This demonstrates that excellent spectrum-splitting can be achieved in practice.

### **Concentration**

Further optical design work is required to produce a submodule efficiency  $>50\%$ . Carissa Eisler designed the primary and secondary concentrators to maximize the conversion efficiency of the subcells. For this study, we employed a compound parabolic concentrator (CPC) as the primary concentrator, which has a parabolic

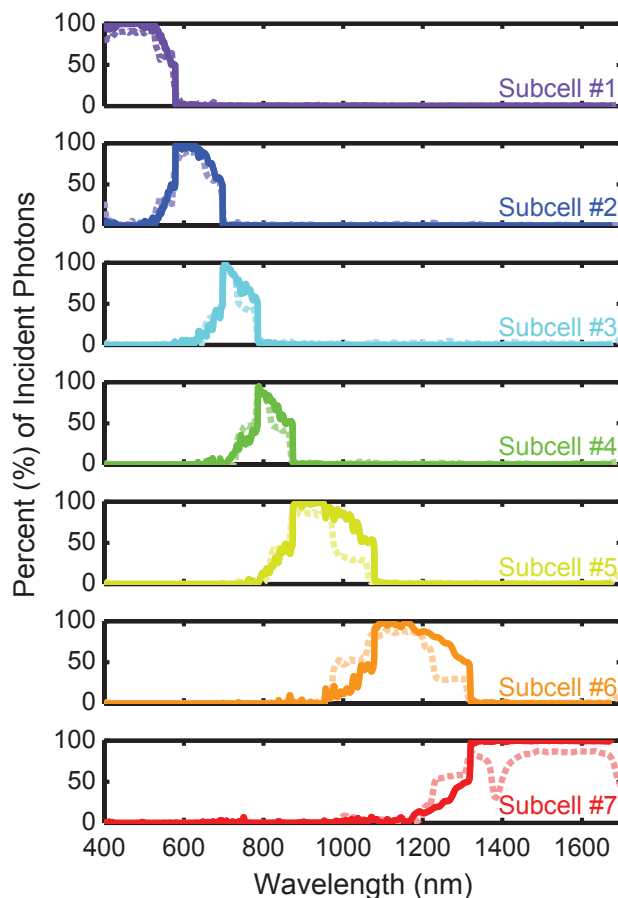


Figure 3.2: Theoretical (solid) and experimental (dashed) spectrum splitting by filter stacks. Filters consist of alternating layers of  $\text{SiO}_2$  and  $\text{TiO}_2$  (solid) or  $\text{SiO}_2/\text{Nb}_2\text{O}_5$  or  $\text{Ta}_2\text{O}_5$  (dashed). The experimental filters were deposited by Chroma Technology based on the theoretical designs and will be described in detail later (§4.1). The fabricated filters are expected to achieve 97% of the designed optical efficiency, showing good agreement and high performance. Designs and figure were generated by Carissa Eisler.

sidewall profile with the parabola focus at the opposite edge of the output face. While Fresnel lenses are more common in deployed multijunction cells, we focused on CPCs in this design work because these concentrators can achieve thermodynamically limited maximum concentration by transferring all photons within a designed acceptance angle to the output face within a designed output angle [60]. We will later explore Fresnel and plano-convex lenses as primary concentrators for select point designs, as well as straight-walled truncated pyramid light pipes when designing to prototype in §4.1.

In general for concentrating optics, the degree of concentration is increased when

the acceptance angle decreases or when the output angle increases. This relationship between acceptance and output angle underlies all design trade-offs in this optical spectrum splitting architecture. The PSR submodule must accept all photons from the sun. Therefore, acceptance angle of the primary concentrator was defined to be  $1.8^\circ$ , which captures the overwhelming majority of the direct ( $0.267^\circ$ ) and circumsolar ( $1.5^\circ$ ) radiation reaching earth at  $37^\circ$  latitude. This is the AM1.5D solar reference spectrum. The large acceptance beyond the solar disk allows for both capture of circumsolar radiation and compensation of tracking error as the sun moves position throughout the day and year.

Additionally, the output angle of the primary concentrator will affect the spectrum-splitting efficiency because the aperiodic dielectric filters, which operate based on constructive and destructive interference, are sensitive to the angle of incident light. Increasing the primary concentration, and thereby increasing the output angle of the primary concentrator, will alter the filter performance and generally decrease the optical efficiency of the filter stack.

Lastly, if the acceptance angle of the secondary concentrator is smaller than the output angle of the primary concentrator, light will be rejected by the secondary concentrators and the optical efficiency will decrease. Consequently, the geometries of the primary and secondary concentrators must be co-optimized to maximize transmission into the most desirable subcell for each wavelength.

The entire integrated PSR structure was modeled via ray tracing simulation. Each ray trace included a realistic set of optical properties for bulk fused silica, the front fused silica face broadband antireflection coating (ARC), subcell ARCs, mirror surfaces, and filter reflection, absorption, and transmission. The incident light source was assumed to be broadband with  $1.5^\circ$  divergence to account for circumsolar radiation. The size of the optical splitting prism was fixed with a  $1\text{ cm} \times 1\text{ cm}$  input aperture, allowing the primary concentrator input size and secondary concentrator output size to vary in order to change the geometric concentration [43], [61]. The photon flux determined from the ray trace was passed to the modified detailed balance calculation to determine both the overall conversion efficiency and the optical efficiency of each optical configuration. Optimizing the contact geometry of each design is computationally intensive, so we calculated a contactless device efficiency,  $\eta_{\text{contactless}}$ , instead of the full submodule efficiency. The contactless device efficiency includes optical and modified detailed balance cell losses, but excludes electrical losses. These electrical losses will be reported for a few select cases in

§3.5. We define the contactless device efficiency as

$$\begin{aligned}\eta_{\text{contactless}} &= \eta_{\text{Opt,TOT}}\eta_{\text{DB}}(E_g, C, \eta_{\text{ext}}, f_{\text{abs}}) \\ &= \eta_{\text{Opt,PC}}\eta_{\text{Opt,PSR}}\eta_{\text{Opt,SC}}k\eta_{\text{DB}},\end{aligned}\tag{3.3}$$

where  $\eta_{\text{Opt,TOT}}$  is the optical efficiency of the entire PSR submodule and  $\eta_{\text{mod}}^{\text{DB}}$  is the modified detailed balance efficiency assuming perfect spectrum-splitting optics and concentrators for the set of seven bandgaps ( $E_g$ ), concentrations ( $C$ ), external radiative efficiencies ( $\eta_{\text{ext}}$ ), and fractions of ideal  $J_{sc}$  ( $f_{\text{abs}}$ ).

The optical efficiency represents the electrical energy conversion with simulated photon allocation relative to that of perfect spectrum-splitting and concentration. The optical efficiency can be further expanded into the individual multiplicative contributions of the primary concentrator ( $\eta_{\text{Opt,PC}}$ ), the spectrum-splitting filter stack ( $\eta_{\text{Opt,PSR}}$ ), the secondary concentrators ( $\eta_{\text{Opt,SC}}$ ), as well as a coupling factor ( $k$ ) to account for any skew rays that are collected given the unique combination of primary output angle and secondary concentrator shape, which will be discussed with regards to Fig. 3.4. Equation 3.3 encapsulates the challenges associated with spectrum-splitting designs: all optical components must be efficient at transferring photons to the correct location; otherwise, the total conversion efficiency will reduce significantly. Concentration can increase the subcell power, but it can also reduce the optical efficiency by altering the light path. Therefore, it is important to co-optimize the two stages of concentration to maximize total efficiency.

Fig. 3.3a and b show different perspectives of the contactless device efficiency of the PSR (color,  $z$ -axis) as a function of secondary concentration ( $x$ -axis) and primary concentration ( $y$ -axis). Each square data point represents an individual simulation for a PSR with a CPC for the primary and secondary concentrators. The projected contour map represents the estimated contactless device efficiency for any concentration combination generated by a natural neighbor fit between the simulated data. Based on previous electrical simulations of spectrum splitting photovoltaic modules (Chapter 6) [62], the efficiency of the power conditioning electronics is expected to be 95-98%. Consequently, contactless device efficiencies exceeding 52% should be able to achieve >50% submodule efficiencies. Indeed, we see that ultrahigh (>50%) efficiency designs are possible with this architecture, with the highest efficiency designs achieved with the combination of low primary concentration and high secondary concentration. Higher primary concentration corresponds to an increased angular distribution on the filter stack (Fig. 3.3 legend), which reduces the optical splitting efficiency. A higher secondary concentration

does not affect the performance of the filters, so in general increasing the secondary concentration increases the efficiency to the point that the acceptance angle of the secondary concentrators approaches the output angle from the primary concentrator. This can be seen in the efficiency roll-off at high secondary concentration, and occurs at lower secondary concentration for larger primary concentration because of the angle matching criterion. It should now be intuitive that a low primary concentration and high secondary concentration will yield the highest optical and contactless device efficiencies. It is also important to note that designs with higher primary concentration ( $>36$  suns) are capable of record module efficiencies ( $>40\%$ ), and are attractive as possible lower cost alternatives that reduce the expensive filter area and secondary concentrator volume. We conclude that the PSR architecture offers a wide range of design regimes that will exceed current photovoltaic module efficiencies.

### **Concentrator truncation**

While the PSR architecture has many designs capable of  $>50\%$  efficiency, many are impractical to fabricate. The optimal design with  $53.6\%$  contactless device efficiency ( $2.25$  suns primary concentration and  $664$  suns secondary concentration) has a hollow primary CPC that is  $398$  mm tall and solid secondary concentrators that are  $595$  mm in length. The secondary concentrators have too high of an aspect ratio for fabrication. Moreover, even vertical packing is impractical when the PSR submodule width exceeds its height. In response, we investigated trimming the primary and secondary CPCs to maintain high efficiency designs with lower aspect ratio concentrators. The CPCs were trimmed by removing length on the input side where the CPC sidewalls are nearly vertical, resulting in minimally reduced concentration. Trimming the primary concentrator reduces the input aperture as the output angle is held constant, which decreases the geometric concentration. The geometric concentration of the secondary concentrator is similarly affected. Additionally, the secondary CPC must be scaled up after trimming to fit onto the  $1\text{ cm} \times 1\text{ cm}$  output face of the filter stack. We repeated the optimization of the concentrators to achieve high efficiency designs with shorter concentrators whose aspect ratio is at least an order of magnitude smaller than the highest concentration design (length  $< 60$  mm).

Fig. 3.4 shows the contactless device efficiencies of trimmed structures based on a low ( $2.25\times$ ) primary concentration (Fig. 3.4a) and a high ( $81\times$ ) primary concentration (Fig. 3.4b). In these structures the output angle of the primary concentrator is

fixed at the value corresponding to the untrimmed CPC ( $2.7^\circ$  for the  $2.25\times$  cases and  $16.4^\circ$  for the  $81\times$  cases), and the different concentration values correspond to different trimmed CPC lengths. The same trend with respect to primary concentration (series colors) is observable across both concentration regimes: at fixed output angle, a longer primary concentrator, and therefore higher primary concentration, results in higher efficiency.

A significantly different trend is observed with respect to secondary concentration length between the two concentration regimes. With a low output angle from the primary concentrator, efficiency increases with increased secondary concentration (length), as in Fig. 3.4a. Contactless device efficiency  $>52\%$ , which we expect to be capable of  $>50\%$  submodule efficiency, is still possible with significantly trimmed secondary concentrators ( $<60$  mm).

With a high output angle from the primary concentrator, efficiency no longer increases monotonically with secondary concentration, but instead peaks at significantly lower secondary concentration than for the untrimmed counterpart submodule designs. Moreover, the efficiencies for the trimmed structures are higher than the corresponding untrimmed structures by as much as 3 percentage points. This is a result of the geometry of the trimmed secondary CPCs. In strongly trimmed cases, the secondary concentrators resemble a light pipe with straight sidewalls (Fig. 3.4c, left), and can refract light erroneously outcoupled into a secondary concentrator near the top of the filter stack back into the filter stack for subsequent reflection and conversion in a lower energy subcell. Submodules with untrimmed concentrators have a negligible likelihood of achieving the same recapture due to the more flat surface profile of the secondary concentrators near the filter stack interface (Fig. 3.4c, right). While none of the trimmed structures based on high primary concentration ( $\geq 36\times$ ) designs achieves  $>50\%$  contactless device efficiency, it is important to note that several can achieve record submodule efficiency exceeding that of their untrimmed counterparts.

### 3.5 Electrical Design

We modeled the subcell, submodule, and module level electrical circuits to determine module efficiencies for seven cases of interest. These cases span two regimes from the previous concentration optimization: (1) ultrahigh efficiency ( $>50\%$  contactless device efficiency) designs and (2) high primary concentration ( $\geq 50$  suns) designs that could be lower cost alternatives. We also included two cases that em-

ploy a lens (Fresnel or plano-convex) as the primary concentrator for comparison. Table 3.3 shows the contactless device efficiency, optical efficiency, and optimized geometries for these designs. Cases 1 and 1a are representative ultrahigh efficiency submodule designs, where Case 1 is a design for prototyping (trimmed) and Case 1a is the maximum efficiency design for comparison (untrimmed). Although Case 1 has a much smaller concentration than Case 1a ( $336\times$  compared to  $1495\times$ ), Case 1 (52.4%) has a contactless device efficiency very close to Case 1a (53.6%) owing to its very high optical efficiency. The optical efficiencies of the primary concentrator and the spectrum-splitting are nearly identical for Case 1 and Case 1a because the primary concentrator is nearly the same geometry between the two designs, yielding a high efficiency spectrum-splitting profile (94%). However the optical efficiency of the secondary concentration stage is higher for Case 1 because Case 1 has trimmed concentrators, opening the acceptance angle of the secondary concentrators and allowing for collection of more photons at the cost of a lower concentration. Therefore, correct allocation of photons is an important metric for high efficiency and should be considered in addition to concentration to optimize spectrum-splitting designs.

Cases 2, 2a, and 2b correspond to the high primary concentration regime balancing performance with the expected cost of manufacturing. Case 2 is an optimized trimmed design based on the  $81\times$  primary concentrator structure. Case 2 is compared to Case 2a, the highest efficiency design for the untrimmed  $81\times$  primary concentration series, and Case 2b, the optimum design from the untrimmed  $49\times$  primary concentration series. Although the geometry of Case 2 was derived from Case 2a, the contactless device efficiency of Case 2 is more similar to that of Case 2b as a result of recapturing light by refraction. This is also reflected in the optical efficiency. Cases 2, 2a, and 2b have similar optical efficiencies through the primary concentration stage (around 98%) as the transfer of photons is mostly affected by the reflectivity of the silver coating and not the angle. We note that this is also similar to the ultrahigh efficiency Cases 1 and 1a. The spectrum-splitting optical efficiency is almost identical between Case 2 and Case 2a (78.2 and 79.6%, respectively) because these two designs have the same angular spread exiting the primary concentration. Consequently, these optical efficiencies are lower than Case 2b (84.2%), which has a lower angular spread exiting the primary concentrator and therefore is more efficient at dividing the incident spectrum. However, while the optical efficiency of the secondary concentrators is very similar for all the high primary concentration cases, the coupling factor is greater than 1 for Case 2 because the refraction in

the secondary concentrators leads to significant recapture of photons that would be otherwise lost. Thus, the optical efficiency for Case 2 (78.5%) more closely matches Case 2b (76.2%) over Case 2a (69.5%), demonstrating a higher efficiency overall despite a significantly lower concentration. While none of the other CPC case study designs exhibits this effect and hence have  $k = 1$ , the effect is pervasive and increasingly effective at reduced secondary length for the simulated designs in Fig. 3.4b.

We additionally investigated a lens as a substitute primary concentrating optic as lenses are far more commonly deployed in concentrator multijunction modules. We designed plano-convex and Fresnel lenses substituted them in the ray tracing simulation file of the existing designs to determine the new contactless device efficiency and optical efficiencies. Cases 1L and 2L are the primary concentrator lens analogs of Cases 1 and 2, respectively, and use poly(methyl methacrylate) (PMMA) lenses. Case 2L employs a Fresnel lens while Case 1L employs a plano-convex lens. In both cases the acceptance angle is slightly reduced to  $1^\circ$  (versus  $1.8^\circ$  in the CPC cases) to more closely replicate current CPV technologies [63]. For a consistent comparison, the output angle of the lens is the same as the original CPC and the secondary concentrator sizes and angles are the same. As a result, the spectrum-splitting and secondary concentrator optical efficiencies between Cases 1 and 1L and Cases 2 and 2L are very similar. Additionally, the optical coupling of Case 2L (1.14) is nearly identical to that of Case 2 (1.13) because the refractive light recapture is present for designs that employ highly trimmed secondary concentrators with a high output angle primary concentrator. However, the total optical efficiencies of the lens cases are significantly less than the original designs. The optical efficiency of the primary CPC is limited mostly by the high reflectivity of the metal surface ( $\sim 98\%$ ), while the optical efficiency of a lens is lower ( $\sim 92\%$ ) owing to the Fresnel reflection and PMMA absorption losses. This results in lower contactless device efficiencies for Cases 1L and 2L by a few percentage points. However, we note that (1) Case 2L is still more efficient than the untrimmed Case 2a because the refraction coupling effect is stronger than the lens losses and (2) that both Case 1L and 2L are capable of record module efficiencies. This shows the versatility of the PSR design and its many high efficiency permutations.

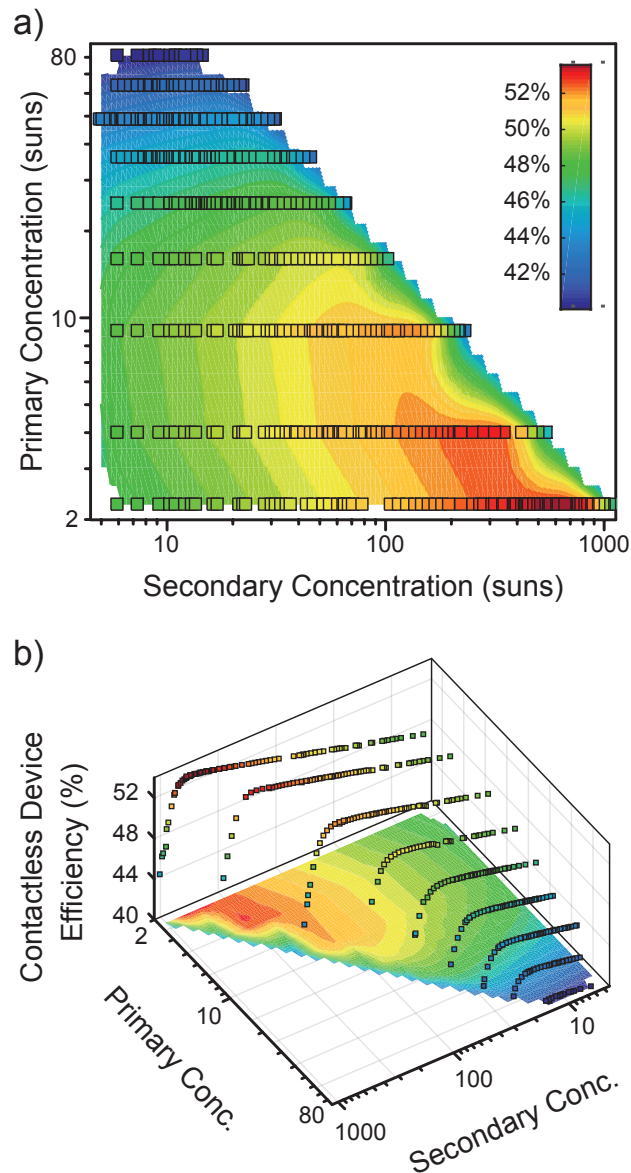


Figure 3.3: Contactless device efficiency landscape as a function of primary and secondary concentration. Each square point represents a ray tracing simulation performed with a CPC for the primary concentrator. The projected contour represents the predicted efficiency for any arbitrary concentration based on these simulations. Contactless device efficiency generally increases with decreasing primary concentration and increasing secondary concentration. Simulations were performed by Carissa Eisler. Interpolation and figure generation were performed by Cristofer Flowers.

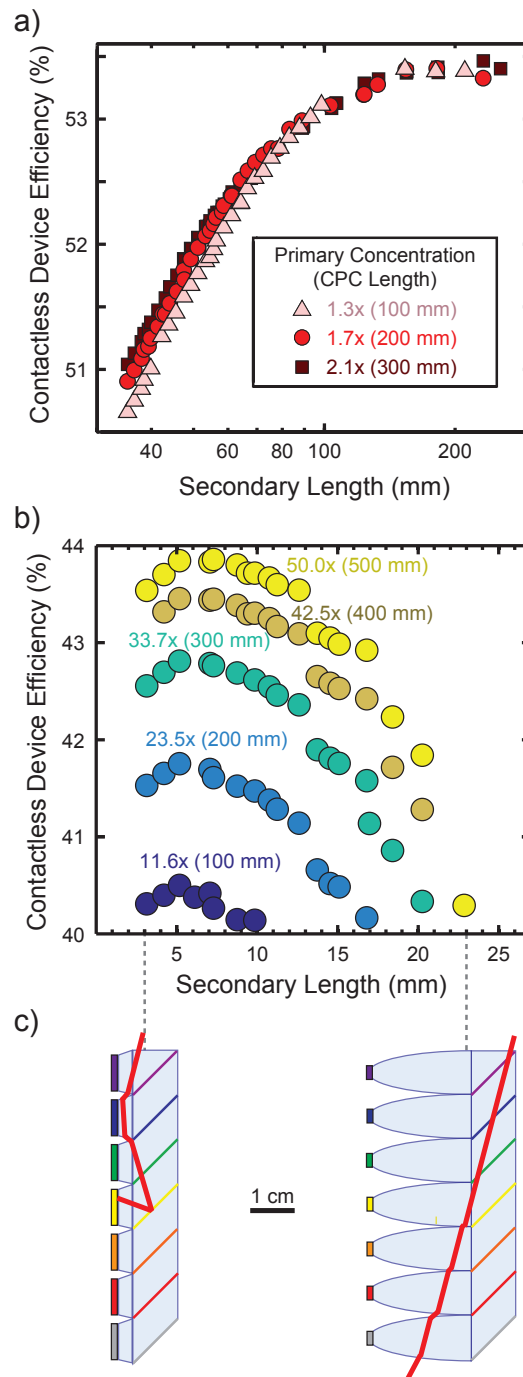


Figure 3.4: Trimmed PSR contactless device efficiency for trimmed PSR sub-modules based on (a)  $2.25\times$  primary concentrator designs and (b)  $81\times$  primary concentrator designs. (c) Light is able to refract back into the PSR and be recaptured in a lower bandgap subcell for highly trimmed concentrators. Simulations and figure generation were performed by Carissa Eisler.

Table 3.3: Point Design Cases for Module Efficiency Prediction

		<b>High Efficiency</b>			<b>High Primary Concentration</b>			
		<b>1</b>	1a	1L	<b>2</b>	2a	2b	2L
<b>Efficiency</b> (%)	<b>Case</b>							
	<b>Contactless Device Efficiency</b>	52.4	53.6	48.0	43.9	40.8	44.5	42.2
	<b>Optical Efficiency Total</b>	91.6	90.8	83.4	78.5	69.5	76.2	74.4
	<i>Primary Concentrator</i>	98.4	98.3	92.2	98.0	97.9	97.9	91.5
	<i>Spectrum-Splitting Optic</i>	94.3	94.3	92.4	78.2	79.6	84.2	77.1
	<i>Secondary Concentrators</i>	98.5	97.6	97.0	90.5	89.2	92.4	91.5
	<i>Coupling Factor</i>	100	100	100	113	100	100	114
<b>Geometry</b> (suns or mm)	<i>Primary Concentrator</i>	1.73	2.25	2.25	50	81	49	90
	<i>(Height)</i>	200	398	265	500	1591	1273	178
	<i>Secondary Concentrator</i>	224	664	224	3	12	20	3
	<i>(Height)</i>	64	595	64	7	52	70	7
	<i>Overall Concentration</i>	386	1495	504	155	974	985	180
	<i>Cell Size</i>	0.67	0.39	0.67	5.69	2.88	2.23	5.69

We then calculated the electrical losses for each case study using (1) a three dimensional distributed circuit model for top contact geometry optimization and resistive losses, (2) analytic determination of resistive interconnection losses, and (3) California Energy Commission (CEC) weighted efficiency specifications for commercially available power conditioning and circuit combination losses.

The contacted subcell electrical performance was simulated in HSPICE as described in Chapter 2 [32], [34]. The contact geometry was independently optimized for every subcell in each case study for contact features with square cross-sections ranging in width from 1-5  $\mu\text{m}$ . Contacts employed in the concentrating photovoltaic industry commonly employ a minimum feature size in the 3-10  $\mu\text{m}$  range, though features as small as 1  $\mu\text{m}$  and below are achievable with photolithography [30], [34]–[37]. Contact designs were constrained to inverted square geometries [27]. The optimization was performed by varying the number of contact fingers at the interior of the cell in order to balance resistive losses from lateral conduction in the semiconductor and metallic grid with optical shading from the grid features. Symmetry was exploited to reduce computational complexity by simulating one quarter of the subcell. The illumination current density is taken from the optical simulation with no shadowed area. The shadowed area from each optimized contact geometry is then passed back into the optical model to determine a self-consistent contactless device efficiency.

The contactless device efficiency intrinsically accounts for recombination current losses because it incorporates the modified detailed balance calculation (3.4). These recombination current losses are also present in the electrical simulations. Therefore, the electrical simulations need to isolate the resistive losses from the recombination losses. This was accomplished by normalizing the performance of the optimized contact case to an ideal collector distributed circuit simulation case. In the ideal case the entire front surface of the device was covered with a perfectly transparent and conductive contact layer that replicates the performance from the contactless device efficiency in the case of zero shadowing. Normalizing the optimized electrical performance by the ideal performance and the shadowed area fraction yields the contact electrical efficiency:

$$\eta_{E,\text{contact}} = \frac{\eta_{\text{optimal}}}{\eta_{\text{contactless}}^{\text{shadowless}} (1 - f_{\text{shadow}})}. \quad (3.4)$$

Multiplication of the contact electrical efficiency, submodule interconnection efficiency, and power conditioning efficiency with the contactless device efficiency

Table 3.4: Submodule interconnection circuit resistive loss contributions

Component	Resistance per Subcell ( $10^{-2} \Omega$ )	Relative Loss ( $10^{-2} \%$ )
Subcell chip carrier leads	0.3	0.5
Chip carrier solder	0.1	0.1
PCB traces	9.7	14.2
Submodule interconnects	4.1	6.0
Interconnect solder	0.3	0.4
String bus	6.5	9.5
Total	20.9	30.7

yields the module efficiency:

$$\eta_{\text{module}} = \eta_{\text{E,contact}} \eta_{\text{E,submodule}} \eta_{\text{E,DC-DC}} \eta_{\text{contactless}} \quad (3.5)$$

### Submodule interconnection efficiency

The submodule interconnection efficiency,  $\eta_{\text{E,submodule}}$ , is the 14-terminal DC power output from the interconnected submodule relative to the 14-terminal DC power output from the contacted subcells. This takes into account resistances due to wire-bonds and solder between subcells and chip carriers, solder between chip carriers and the submodule printed circuit board (PCB), copper traces on the PCB, solder between the PCB and submodule interconnecting wires, interconnect wires, and the electrical bus connecting series submodule strings in parallel arrays. The resistive losses are calculated on a per-subcell basis and subsequently normalized to the subcell output power and weighted by the overall power output at each bandgap to determine the relative power loss contribution. These contributions are enumerated in Table 3.4 for the Case 1 design. The total loss is approximately 0.3%, resulting in a submodule interconnection efficiency of 99.7%.

All resistances were calculated from the conductor geometry and the bulk resistivity by Pouillet's Law,

$$R = \rho_{\text{bulk}} \frac{L}{A_c}, \quad (3.6)$$

where  $\rho_{\text{bulk}}$  is the material-dependent bulk electrical resistivity,  $L$  is the conduction length, and  $A_c$  is the cross-sectional area for conduction. Resistances in series are summed according to Kirchoff's voltage law, while conductances ( $G \equiv 1/R$ ) in parallel are summed according to Kirchoff's current law. For all of the resistance

calculations, copper resistivity is taken equal to  $1.68 \times 10^{-8} \Omega \cdot \text{m}$  [64], and tin-lead solder resistivity is taken equal to  $1.65 \times 10^{-7} \Omega \cdot \text{m}$  [65].

The subcell chip carrier leads account for two series sets of four parallel copper wire bonds each 5 mm in length and  $100 \mu\text{m}$  in diameter, ignoring the macroscopic carrier feet whose resistance is negligible relative to the wire bonds. The chip carrier solder assumes wire bonds are bonded to a solder bump on the chip carrier with interfacial area equal to the wire diameter of  $100 \mu\text{m}$  and an overall thickness of  $100 \mu\text{m}$ , and two of these interfaces exist in parallel to accommodate two terminals for each subcell. Traces on standard “1 oz” copper-plated PCBs were 1 mm wide by  $34.7 \mu\text{m}$  thick. Each subcell has two series traces with average length of 10 cm. Adjacent submodules in series are interconnected with two 36 American wire gauge (AWG) copper wires ( $A_c = 0.0127\text{mm}^2$ ) with a length of 3 cm. These interconnect wires are soldered to the PCB with an assumed interfacial area equal to the wire cross-sectional area and  $100 \mu\text{m}$  thick solder. Two such solder joints in series account for the positive and negative interconnections to each subcell. Lastly, the bus is designed to consist of a  $1 \text{mm}^2$  cross section copper bar 1 m in length. While in practice the currents from each of the parallel strings would not traverse the entirety of the bus, I made a conservative limiting assumption that the entire parallel current density would experience the full resistive loss of the bus rather than specifying precise geometrical spacing of the strings. Consequently, the reported string bus resistive loss can be viewed as an upper bound.

The design space is in principle large for each of these losses due to freedom in selecting, the interconnection wire gauge, number of parallel wire bonds, and PCB copper plating thickness and trace width, among other parameters. Consequently, the specific assumptions and resulting values presented in Table 3.4 primarily serve to explain the design process. It is assumed that in each of the other design cases a comparable interconnection efficiency can be achieved by variation of the aforementioned parameters within a reasonable design space.

### **DC-DC power conditioning for two-terminal output**

Independent series-parallel circuits for each of the bandgaps comprise the module topology and are summarized in Table 3.5. Subcells at each bandgap are connected electrically independently to form strings  $N_{\text{series}}$  in length, and  $N_{\text{parallel}}$  parallel strings are connected through an electrical bus. Series subcells accumulate voltage and parallel strings accumulate current in order to match the nominal input speci-

fication range of the DC-DC power converter specified by “DC-DC Model”. Each independent series-parallel circuit connected to a DC power optimizer undergoes maximum power point tracking and output voltage synchronization with power conditioning efficiency,  $\eta_{E,DC-DC}$ . The California Energy Commission (CEC) weighted efficiency for a power converter is the operating efficiency averaged over an annual power distribution corresponding to irradiance in the United States desert southwest. The CEC efficiency for a SolarEdge P-300 DC power optimizer is specified at 98.8% and is taken to be a good representation of the power combination efficiency between a 14-terminal module and a 2-terminal module [62], [66]<sup>1</sup>. As for the submodule interconnection efficiency, DC-DC power conditioning efficiency was assumed constant across all design cases.

---

<sup>1</sup>The cited P-600 series DC power optimizer, which was used in the design, is no longer in production. A similar design can be performed with the P-300 series power converters.

Table 3.5: Module interconnection circuit topology parameters using DC-DC converters

$E_g$	$V_{\text{mpp}}$ (V)	$I_{\text{mpp}}$ (A)	$N_{\text{parallel}}$	$N_{\text{series}}$	$V_{\text{series}}$ (V)	$I_{\text{parallel}}$ (A)	$P_{\text{mpp}}$ Power (W)	$N_{\text{DC-DC}}$	DC-DC (W)	DC-DC Model
2.13	1.80	2.0E-02	250	40	71.9	5.1	1453	4	363	OP400-MV
1.78	1.51	1.2E-02	250	80	120.5	3.0	729	2	364	OP400-EV
1.58	1.26	1.4E-02	250	80	101.0	3.6	717	2	358	OP400-EV
1.42	1.11	1.1E-02	500	40	44.3	5.6	491	2	246	OP250-LV
1.15	0.84	2.2E-02	160	125	105.6	3.6	750	2	375	OP400-EV
0.94	0.66	1.5E-02	250	160	105.8	3.8	405	1	405	OP400-EV
0.74	0.49	1.2E-02	400	100	48.6	5.0	241	1	241	OP250-LV

### Comprehensive module performance

Fig. 3.5 shows the optimized module efficiency as a function of contact finger feature size for each of the case studies (Fig. 3.5a), along with the fractional contribution of each of the electrical and shadowing losses for contact optimizations with  $1\ \mu\text{m}$  and  $3\ \mu\text{m}$  features (Fig. 3.5b). Even with  $3\ \mu\text{m}$  wide fingers Case 1 is capable of producing an ultrahigh efficiency module, while employing smaller contact feature sizes broadens the ultrahigh efficiency design space for both Cases 1 and 1a. Additionally, Cases 2, 2b, and 2L illustrate a range of higher primary concentration designs with record module efficiencies. Each of the displayed cases approaches the corresponding contactless device efficiency at its peak.

The efficiency versus feature size curves in Fig. 3.5a can generally be divided into two regimes of negative and positive slope. To understand each of these regimes, first consider that the optimum contact geometry occurs where the rate of increase in obscured area, or “shadow”, losses from adding additional contact fingers equals the rate of decrease in contact resistive losses. Further, the contact resistive losses are comprised of resistance to lateral conduction in the emitter sheet, contact resistance at the semiconductor-metal interface, resistivity of the metal fingers, and resistivity of the busbar. The ratio of electrical to shadow loss varies by cell size and concentration regime. Lower concentration designs are less sensitive to contact feature sizes according to the quadratic relationship between current and resistive power loss in the contacts ( $P = I^2R$ ). This relationship dictates a steeper slope to the efficiency versus contact feature size curves for designs with higher overall concentration. For example, this quadratic loss relationship enables the trimmed, lower concentration Case 1 to outperform its untrimmed, higher concentration counterpart Case 1a for contact features  $\geq 2\ \mu\text{m}$ . Most of the cases considered fall within this regime of increasing efficiency with decreasing finger width. In this regime the resistive losses are dominated by the lateral sheet resistance of the device emitter layer. Thus, decreasing the finger width increases the optimal number of fingers to decrease finger-to-finger spacing, parallelizes current collection and reduces sheet resistance loss while simultaneously reducing the total shadowed area. The sheet resistance dominated loss regime is most apparent for cases 1, 1a, 1L, and 2b in Fig. 3.5b. These cases show mutual reduction of both resistive and shadow loss for  $1\ \mu\text{m}$  optimized contact features relative to  $3\ \mu\text{m}$  optimized contact features.

In contrast, the regions of positive slope correspond to regimes where the finger and

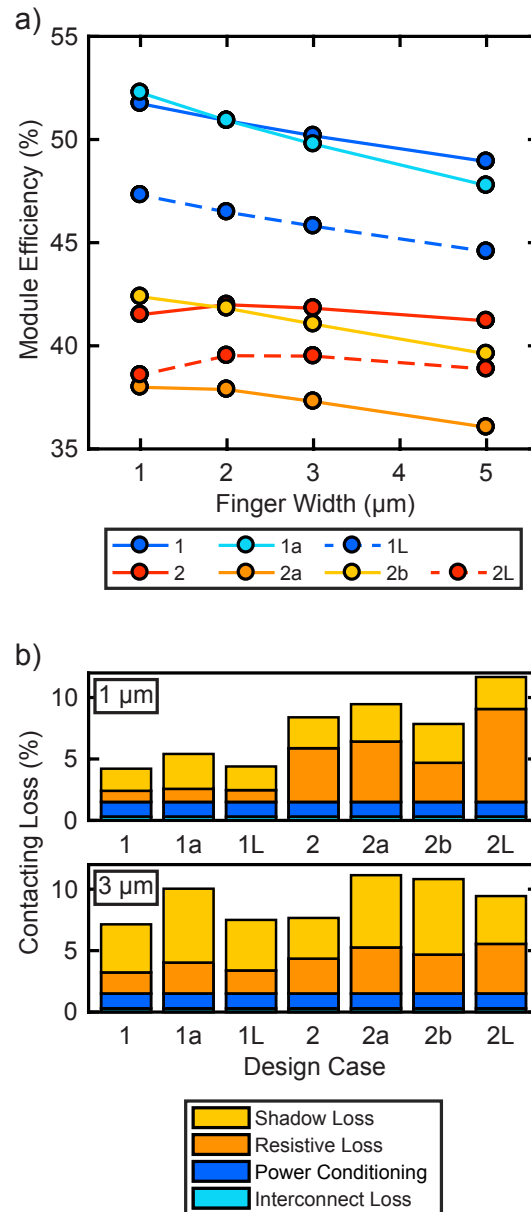


Figure 3.5: Simulated module efficiency with optimized contact grids.

busbar resistive losses are sufficiently large to dominate the aggregate shadow and resistive loss. Maintaining constant aspect ratio has the side effect of constraining the entire contact metallization thickness, thereby increasing the finger and busbar resistances. In cases of high current, most notably in those with larger cell sizes that have higher resistance due to conduction length, decreasing the feature size results in reduced shadow and emitter sheet resistive loss but a net increase to resistive and cumulative loss, and consequently lower efficiency. Cases 2 and 2L exhibit resistive loss dominated contact metallization; both the ratio of resistive to shadow loss and

the net loss increase as the feature size is decreased. Lastly, Case 2a represents a transitional case between the aforementioned regimes. The ratio of resistive to shadow loss increases significantly with decreasing feature size, but the net loss is reduced. This transitional region at the smallest feature size considered corresponds to the leveling out of slope of the Case 2a curve in Fig. 3.5a.

These mechanisms serve to identify a few areas of future interest broadly applicable to concentrating photovoltaics. First, there is substantial potential for increased efficiency by driving toward small cells and fine contact features. Second, an optimum contact feature size exists given the specific aspect ratio constraints of a given contact patterning process and the geometrical parameters of the cell and concentration employed. Finally, this optimum can be improved by developing processes for higher aspect ratio contacts, thereby reducing resistive loss in the contact metallization and expanding the potential for improved efficiency.

### **Optical and electrical modeling conclusions**

Thus far, we have accounted quantitatively for each of the optical and electrical losses in a spectrum splitting photovoltaic module by integrating modified detailed balance subcell performance calculations, wave optical filter simulations, ray tracing optical allocation simulations, 3-dimensional distributed circuit subcell resistive loss modeling, inter-subcell resistive loss modeling, and power combination loss modeling. This culminates in the predictive parametric equation for module efficiency,

$$\eta_{\text{module}} = \eta_{\text{E,contact}} \eta_{\text{E,submodule}} \eta_{\text{E,DC-DC}} \eta_{\text{Opt,PC}} \eta_{\text{Opt,PSR}} \eta_{\text{Opt,SC}} k \eta_{\text{DB}}, \quad (3.7)$$

which enables us to map out a wide design space. From this integrated modeling we conclude that both record (>40.4%) and ultrahigh (>50%) module efficiencies are achievable using existing cell, optical, and electrical technologies. A submodule with seven subcells can exceed 50% efficiency if (i) the ensemble averaged subcell external radiative efficiency is at least 3%, (ii) the splitting and concentrating optical efficiency is  $\geq 90\%$  with (iii) low (<10 $\times$ ) primary and high (>100 $\times$ ) secondary concentration, and (iv) the submodule incorporates a high electrical efficiency (>96%) including subcell contact resistive losses, interconnection losses, and power combination losses. The required external radiative efficiencies are possible with very low-defect, off-substrate solar cells experimentally demonstrated by the III–V cell growth field [45], [46]. Further, we have now demonstrated a broad range of designs that can achieve high optical efficiency with moderate to high concentration, as well as high electrical efficiency. We conclude that the polyhedral specular reflec-

tor architecture and the module modeling tools developed herein are enabling for ultrahigh efficiency modules.

### 3.6 Thermal modeling

An additional efficiency advantage is expected for lateral spectrum splitting photovoltaics over monolithic multijunctions due to a reduction in operating temperature. While an on-sun efficiency advantage is not generally incorporated in standard room temperature concentrator efficiency ratings, a lower operating temperature is an additional contributor to both increased annual energy production and reduced levelized cost of electricity. Increased operating temperature has two effects on photovoltaic devices. First, most semiconductors undergo bandgap narrowing with increasing temperature according to

$$E_g(T) \approx E_g(0) - \frac{\alpha T^2}{T + \beta}, \quad (3.8)$$

where  $\alpha$  and  $\beta$  are positive empirical parameters with units of eV/K and K, respectively. This narrowing tends to minimally increase current collection by facilitating absorption of photons with slightly lower energy than the room temperature bandgap. Second, the open circuit voltage drops substantially due to an increase in the recombination currents according to

$$V_{oc} = \frac{nkT}{q} \ln \left( \frac{J_{sc}}{J_0} + 1 \right), \quad (3.9)$$

assuming a single diode model for the solar cell. Expanding the dark saturation current

$$J_0 \equiv \frac{qD_p n_i^2}{L_p N_D} + \frac{qD_n n_i^2}{L_n N_A} \propto T^{3+\gamma/2} \exp \left( -\frac{E_g}{kT} \right), \quad (3.10)$$

which rapidly increases with increasing temperature across the typical operation range of photovoltaics (300-400 K). Both of these effects can be summarized by the empirical temperature coefficient, which is the absolute percentage change in efficiency per Kelvin with increasing temperature. A value of 0.08%/K is typical for III-V materials [67], so operating 12 K cooler translates to one absolute percentage point of efficiency increase. Efficiency gains of this magnitude are typically the outcome of multiple years of research and millions of dollars in funding.

We have modeled a >47% efficient module with passive thermal management maintaining cell temperature withing ~16 °C of ambient under AM1.5D illumination using COMSOL Multiphysics for thermal analysis. The model was developed for

a PSR using 25 mm long light pipe secondary concentrators to achieve 48.5% simulated module efficiency. The physical dimensions of the prototype must be abstracted slightly to enable proper meshing and compatible length scales between the cells and optics for simulation. The parallelepiped and light pipes are drawn at scale and composed of quartz. Subcells all have GaAs material properties. The chip carrier is abstracted to a thin planar copper layer equivalent in thickness to the metal thickness on the physical chip carrier. The printed circuit board is assumed to be made of FR-4 fiberglass epoxy laminate, and the submodule is surrounded by air and undergoes forced convection at 1 cm/s average velocity. This model neglects PCB traces and vias, consequently reducing heat spreading. It also neglects radiative coupling between adjacent surfaces. Cumulatively, these assumptions will cause the simulated temperature to be greater than the actual temperature.

Heat transport is governed by the heat equation incorporating Fourier's law of conduction. In steady state, convected and conducted heat out of the simulation volume is balanced by heat generation within the volume:

$$\rho C_p \mathbf{u} \cdot \nabla T - \nabla \cdot (\mathbf{k} \cdot \nabla T) = Q. \quad (3.11)$$

Rather than approximate a convective heat transfer coefficient, we directly calculated the velocity field of the surrounding air medium. This was governed by the Cauchy momentum equation,

$$\rho (\mathbf{u} \cdot \nabla) \mathbf{u} = \nabla \cdot \left[ -p \mathbf{I} + \mu \left( \nabla \mathbf{u} + (\nabla \mathbf{u})^T \right) - \frac{2}{3} (\nabla \cdot \mathbf{u}) \mathbf{I} \right] + \mathbf{F} \quad (3.12)$$

and continuity,

$$\nabla \cdot (\rho \mathbf{u}) = 0. \quad (3.13)$$

We applied a no-slip boundary condition at the PSR surfaces and a periodic boundary condition at the simulation walls to capture the environment of an array of tiled PSR submodules within a larger photovoltaic module.

Figs. 3.6 and 3.7 show the simulated geometry and surface temperature map (K) map across the optics, subcells and printed circuit board in a periodic flow volume. The air inlet is fixed at ambient temperature (298.15 K), with whiter regions being hotter. We predict subcell maximum and minimum temperature rise of 16.5°C and 7°C across the seven subcells, as illustrated more precisely in the temperature cut through the cell plane in Fig. 3.8. Each of the peaks occurs within one of the seven subcells, with troughs occurring in the air intermediate between subcells.

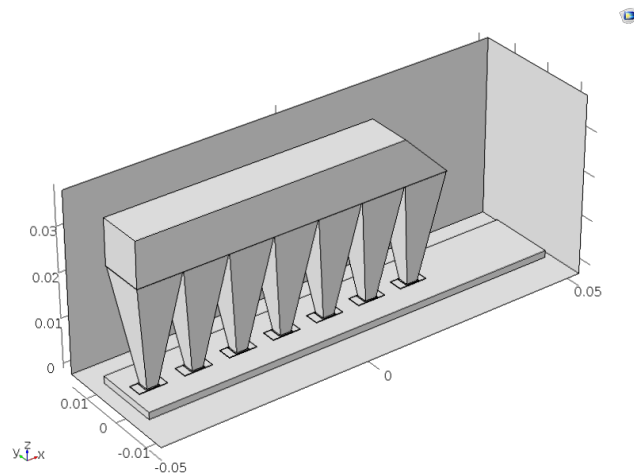


Figure 3.6: Polyhedral specular reflector geometry simulated in COMSOL including spectrum splitting optics, secondary concentrators, subcells, abstracted chip carriers, and a simplified printed circuit board.

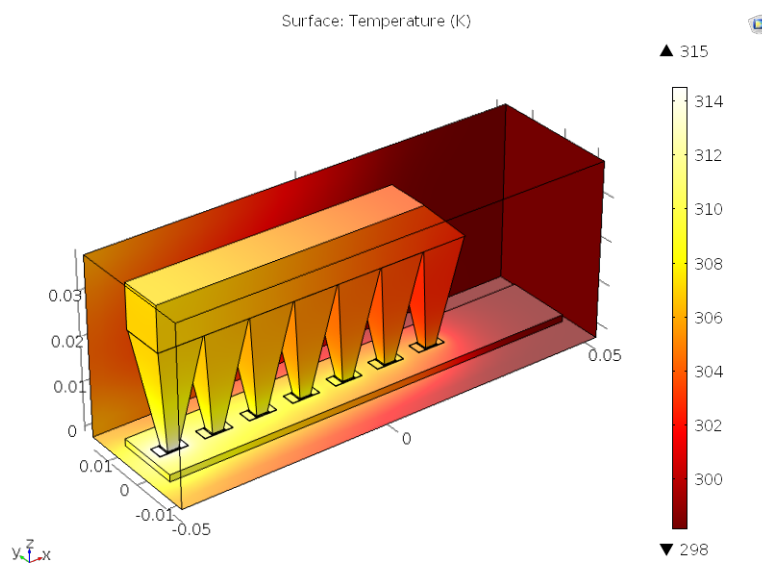


Figure 3.7: Surface temperature (K) map across the optics, subcells and printed circuit board in a periodic flow volume. The air inlet is fixed at ambient temperature (298.15 K), with whiter regions being hotter.

Lastly, slices of the air velocity profile are shown in Fig. 3.9. The maximum air velocity is 2.4 cm/s (0.054 mi/h), which is order of magnitude consistent with the velocity predicted according to equation (10.9-16) for recirculating free convection in Bird *et al.* [68]. Using the parameters relevant to the considered system ( $\nu = 0.16 \text{ cm}^2/\text{s}$ ,  $\bar{\beta} = 3.3 \times 10^{-3} \text{ K}^{-1}$ ,  $\Delta T = 16.5 \text{ K}$ ,  $B = 1 \text{ cm}$ ) estimates an average velocity of 7 cm/s in the vicinity of the highest temperature subcell.

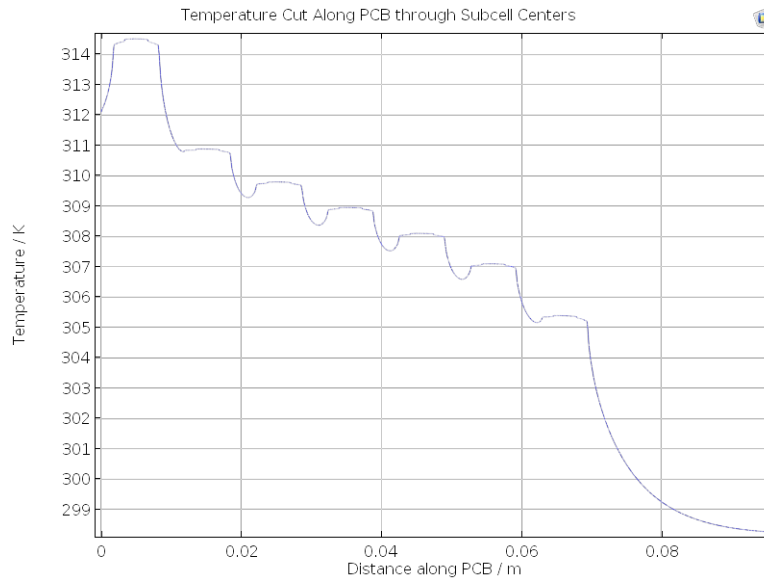


Figure 3.8: Temperature profile (K) along a cross-sectional cut through the subcells' centers. Each of the peaks occurs within one of the seven subcells, with troughs occurring in the air intermediate between subcells. Maximum and minimum temperature rises of 16.5 K and 7 K above ambient are determined.

Figs. 3.10, 3.11, and 3.12 show the equivalent surface temperature maps, cell temperature cut, and velocity slice map for a monolithic multijunction under a solid secondary concentrator. Total concentration and power dissipated were assumed to be the same as the PSR submodule case, but the heat generation is confined to a single cell volume. Consequently, the temperature rise above ambient is over twice as large as that of the hottest subcell in the PSR submodule.

While the absolute value of the temperature rise is dependent on the assumed air flow rate (1 cm/s), the relative temperature rise is less than half of that of a traditional monolithic multijunction. Conventional CPV modules typically operate between 30-80°C above ambient [69]. Consequently, we expect a substantial efficiency advantage for lateral spectrum splitting designs on the order of multiple percentage points at concentrator standard operating conditions (CSOC). Lastly, assuming a temperature coefficient of 0.08%/K, as for flat plate GaAs [67], our simulated module efficiency including temperature degradation is 47.1%.

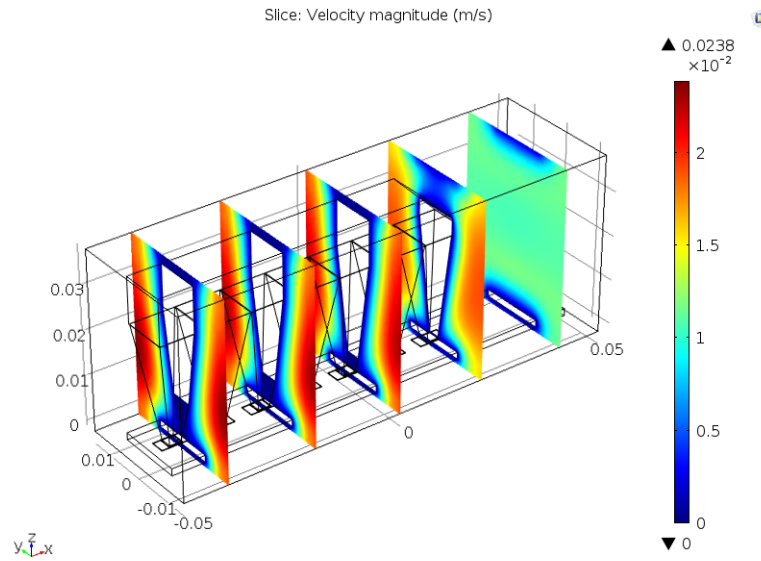


Figure 3.9: Velocity profile (m/s) slices along the length of the PSR used to determine convective heat transport away from the subcells.

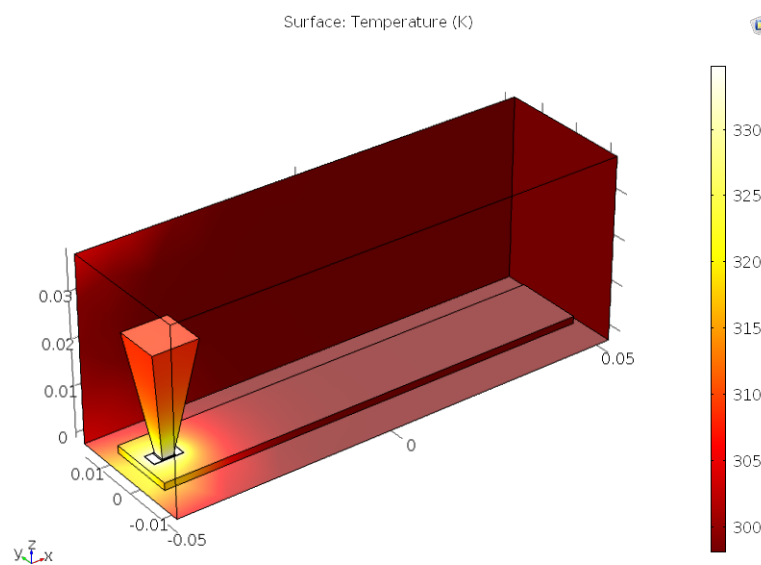


Figure 3.10: Surface temperature (K) for a monolithic multijunction of identical size and concentration to the spectrum-splitting case studied above, with whiter regions being hotter.

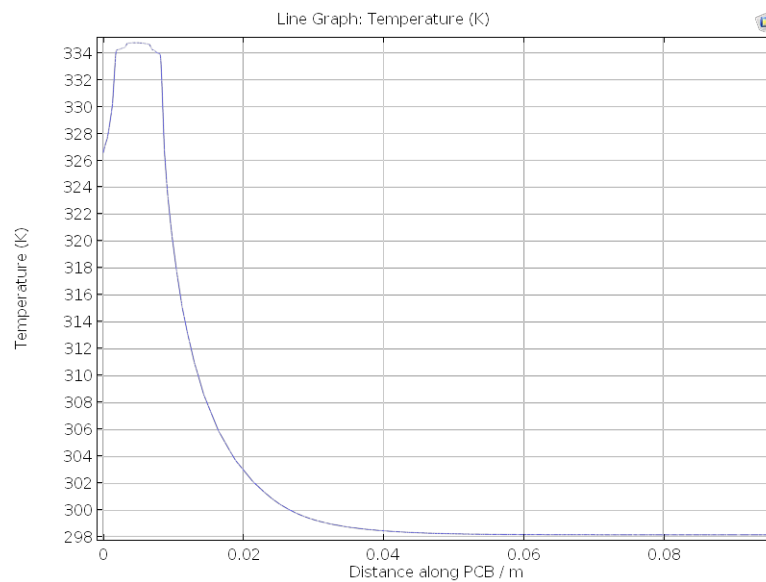


Figure 3.11: Temperature profile (K) along a cross-sectional cut through the monolithic cell's center. The peak occurs within the cell. A maximum temperature rise of 36.5 K above ambient is determined.

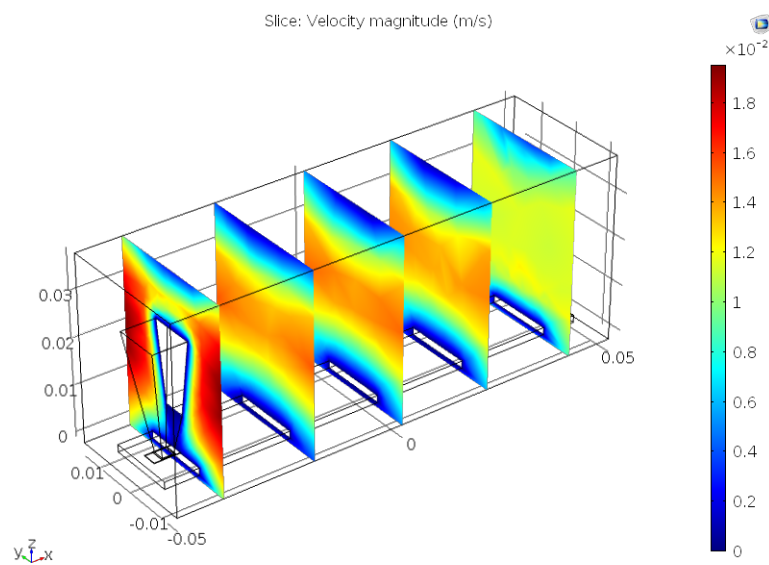


Figure 3.12: Velocity profile (m/s) slices along the length of the monolithic equivalent device used to determine convective heat transport away from the cell. The maximum air velocity is 2 cm/s (0.045 mi/h).

*Chapter 4***COMPONENT PROTOTYPING AND INTEGRATION FOR SPECTRUM SPLITTING PHOTOVOLTAIC SUBMODULES**

The previous chapter detailed the computational modeling and design of a class spectrum splitting photovoltaic submodules capable of achieving unprecedented sunlight conversion efficiency. Coupling individual models for optical throughput, cell power conversion, electrical collection and interconnection, and thermal performance enabled a robust probe of the design space available to the polyhedral specular reflector. In particular, this coupled model provided critical insight into the trade-offs between achievable efficiency (PSR Case 1a) and component simplification for practical implementation (Case 1). In this chapter we discuss an additional point design polyhedral specular reflector which makes additional design simplifications and efficiency concessions for manufacturing feasibility. Additionally, we describe in detail the prototype assembly procedure for this submodule point design. This integration procedure is inclusive of optics, cells, and additional electrical and mechanical components to support the submodule and facilitate power extraction.

Characterization of the integrated prototype will be reported in Chapter 5, so the focus herein will be the design and integration procedure. To that end, we will describe in sequence (§4.1) the point design specifications of the submodule to be prototyped, (§4.2) the fabrication and integration of the optical components, (§4.3) fabrication, processing, and mounting of the subcells at all seven bandgaps, (§4.4) design and fabrication of the printed circuit board and mechanical components, and (§4.5) final integration of the submodule optical and electronic components.

**4.1 Polyhedral specular reflector submodule with 100× light pipe concentrators**

The prototype design of the polyhedral specular reflector consists of a 1 cm × 1 cm input aperture with a broadband anti-reflection coating (ARC). A broadband anti-reflection (AR) coating is needed on the front surface of the filter stack in order to minimize Fresnel reflection at the air-fused silica interface, which otherwise amounts to ~4% optical loss. The coating is a multilayer dielectric stack on a 1 cm × 1 cm × 1 mm Corning UVFS 7980 slide, designed, deposited, and measured by Reynard Corporation. Reynard Corp. chose not to disclose the materials and

thicknesses used in the filter deposition, but a broadband anti-reflection coating of comparable performance composed of  $\text{MgF}_2$ ,  $\text{SiO}_2$ , and  $\text{TiO}_2$  was previously designed and reported by Eisler *et al.* [53]. Design targeted  $<1.5\%$  broadband reflectivity loss as defined by the optical efficiency formula in equation 3.2 (§3.2).

The ARC is attached to a longpass filter stack consisting of six parallelepipeds and one triangular prism composed of fused silica (Corning UVFS 7980). embedded in fused silica (Corning UVFS 7980) that separates incident white sunlight into a cascade of wavelength bands. The  $45^\circ$  oriented lower diagonal face of each piece is coated with a multilayer dichroic long-pass filter consisting of alternating layers of  $\text{SiO}_2$  and  $\text{Ta}_2\text{O}_5$  (triangular prism, top filter) or  $\text{Nb}_2\text{O}_5$  (parallelepipeds). The filters were deposited using reactive DC sputtering by Chroma Technology, and the stack was assembled at Caltech. Each of the prisms was oversized to a  $10.4 \text{ mm} \times 10.4 \text{ mm}$  top-down projected area to allow for  $0.2 \text{ mm}$  bevels along all of the edges with  $\geq 90^\circ$  angles. This decreased the design optical efficiency by  $\sim 1\%$  [61], but helps to prevent the formation of chips along the sharp edges which would deleteriously impact the optical performance.

Successively, each wavelength band is reflected through a secondary light pipe concentrator to a small subcell comprised of a III-V material with bandgap closely matched to the minimum illuminating wavelength. Each light pipe is a truncated, straight-walled pyramid  $100 \text{ mm}$  long with a  $10 \text{ mm} \times 10 \text{ mm}$  input face, a  $1 \text{ mm} \times 1 \text{ mm}$  output face, and provides  $100\times$  geometrical concentration. The light pipes are composed of Corning 7980 UVFS and were ground and polished into the described dimensions by Isuzu Glass Ltd.

A subcell is attached to each of the light pipe output faces with subcell bandgap decreasing while moving away from the input aperture. Subcells at each of the seven lattice matched bandgaps listed in Table 3.1 (§3.3) were designed for epitaxial liftoff and two-pass absorption by Spectrolab, Inc. Spectrolab grew epitaxial material stacks via III–V metal-organic chemical vapor deposition (MOCVD) , performed basic testing, and delivered the wafers to Caltech for device processing. Processed subcells are mounted to chip carriers via wire bonding and conductive epoxy to minimize the number of times the contact pads directly atop the epitaxial material have to be electrically probed. Additionally, the chip carriers facilitate mounting the submodule to a printed circuit board (PCB) for submodule interconnection.

Fig. 4.1 shows the polyhedral specular reflector (PSR) spectrum splitting photovoltaic submodule. It includes each of the previously described components (less

the chip carriers) attached and configured for lateral spectrum splitting. Fig. 4.1b shows the same PSR implemented in ray tracing software with a demonstrative subset of rays being split by wavelength and directed to each of the subcells, including the chip carriers.

In total the predicted sunlight conversion efficiency is 47.9% under the AM1.5D solar reference spectrum. This calculation employs the models presented in Chapter 3 in conjunction with the geometric and materials information of the prototype described in this section. A summary of design parameters is presented in Table 4.1 for reference.

Table 4.1: PSR prototype submodule design specifications

Parameter (Units)	Value
$\rho_M$ ( $\Omega \cdot \text{m}$ )	$3.5 \times 10^{-8}$
$\rho_{\text{bulk}}$ ( $\Omega \cdot \text{m}$ )	$2.4 \times 10^{-2}$
$\rho_c$ ( $\Omega \cdot \text{m}^2$ )	$3.7 \times 10^{-10}$
$\rho_{bc}$ ( $\Omega \cdot \text{m}^2$ )	$8.0 \times 10^{-9}$

Fig. 4.1c is a photograph of the integrated submodule prototype following the procedure described from §4.2–4.5. The prototype submodule includes an input face broadband antireflection coating, all solid spectrum splitting and concentrating optics, and seven unique subcells on chip carriers.

## 4.2 Optics prototyping and integration

The filter stack was assembled in series from the longest wavelength cutoff (silver mirror) to the shortest (573 nm) on a 45° inclined assembly jig to provide alignment guides. Each filter was attached using 4  $\mu\text{L}$  of Sylgard 184 PDMS (2:1 base:curing agent) deposited by micropipette to form a thin optomechanical adhesive layer. Each of the prism exterior faces was precisely covered with Kapton tape to prevent excess PDMS wicking onto the sidewalls and reducing the efficacy of total internal reflection used to laterally confine the light. For each of the six attachment steps, the filter stack was placed in a desiccator under rough vacuum for  $\geq 15$  minutes to remove any trapped air bubbles and then baked in a laboratory oven at  $80 \pm 10^\circ\text{C}$  for 40 minutes to cure the PDMS.

Following all filter attachment steps, the stack was then mounted vertically in order to attach the broadband anti-reflection coating using the same the same PDMS

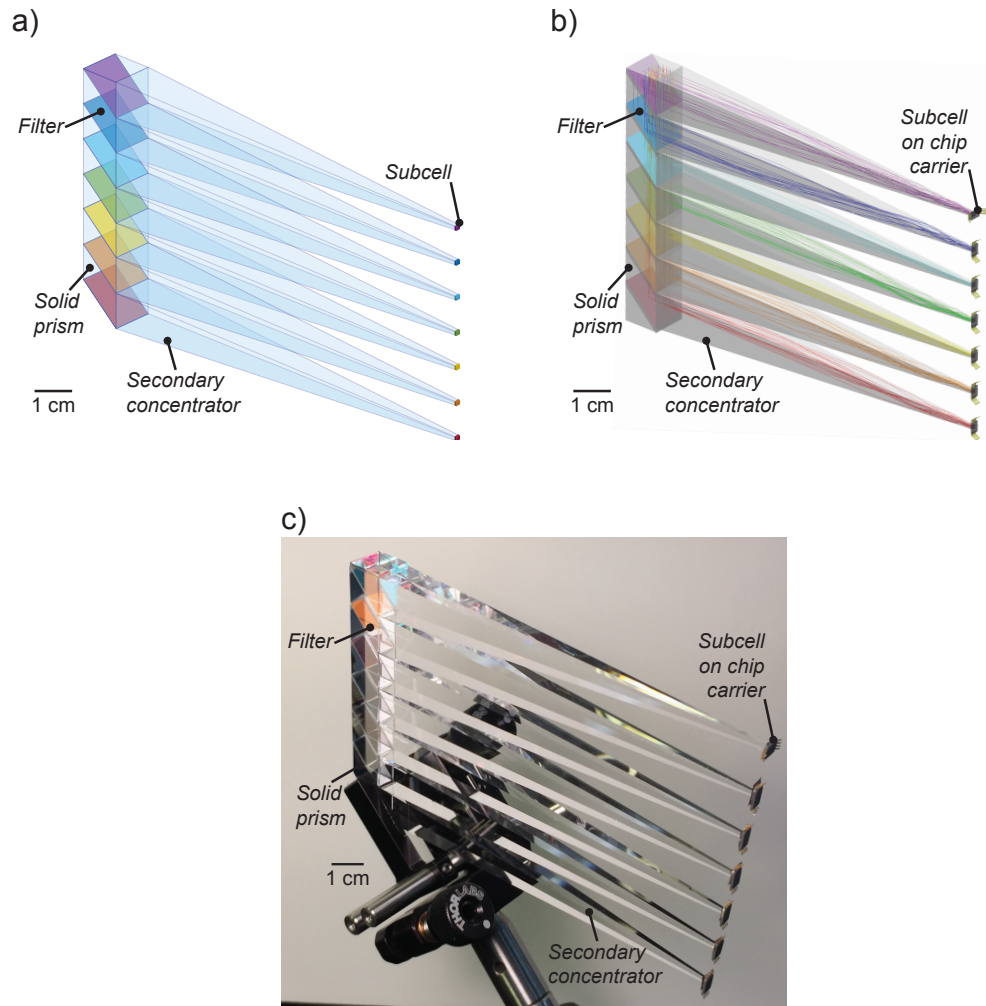


Figure 4.1: Three representations of the polyhedral specular reflector in concept, modeling and experiment. (a) Schematic illustration of the PSR highlighting the locations of solid optics, spectrum-splitting filters, and subcells. (b) Implementation of the PSR for ray tracing with split spectrum reaching each of the seven subcells. (c) Photograph of the integrated PSR submodule with equivalent components to the schematic and ray trace.

attachment, desiccation, and curing procedure. Kapton tape was removed and the filter stack was cleaned with acetone and isopropyl alcohol prior to optical characterization.

### 4.3 Cell processing and mounting

#### Cell processing

John Lloyd processed each of the seven III–V subcell wafers into functional on-film photovoltaics by the following procedure:

1. wafer singulation into  $\sim 1$  in<sup>2</sup> pieces;
2. back contact seed layer evaporation of Ni/Au 4/125 nm;
3. back contact Cu electroplating ( $\sim 100$   $\mu\text{m}$ );
4. epitaxial lift-off in concentrated hydrofluoric acid (HF) (GaAs-based subcells) or 1:1 concentrated HF:ethanol (InP-based subcells);
5. front contact photolithography (Shipley 1813 or nLOF 2020 photoresist, Karl Suss Model MJB3 mask aligner);
6. front contact electron beam evaporation of Pd/Ge/Au 10/50/500 nm (GaAs-based subcells) or Ni/Au 4/500 nm (InP-based subcells);
7. metal liftoff in Remover PG or acetone;
8. contact anneal at 200 °C for 24 h (GaAs-based subcells only);
9. contact layer etch in H<sub>3</sub>PO<sub>4</sub>:H<sub>2</sub>O<sub>2</sub>:H<sub>2</sub>O (GaAs-based subcells only);
10. mesa etch photolithography;
11. mesa etch in non-selective aqua regia (non-selective), H<sub>3</sub>PO<sub>4</sub>:H<sub>2</sub>O<sub>2</sub>:H<sub>2</sub>O (As-based layers), and HCl:H<sub>2</sub>O 1:1 (P-based layers);

#### Chip carrier mounting

After processing of the epitaxial stacks into subcells is complete, each cell on film is tested via light and dark *I-V* sweeps. Performance parameters are extracted from the sweeps to identify champion devices. These champion subcells are then singulated and mounted on chip carriers to reduce handling the subcell films directly and facilitate electrical connection to a printed circuit board. Singulation is performed manually with a scalpel, and subcells are mounted to chip carriers (Spectrum Semiconductor Model CSO008P4 08 TSSOP) via a  $< 50$   $\mu\text{m}$  layer of conductive silver epoxy (Epoxy Technology EPO-TEK H20E). The epoxy was cured by baking for 15 minutes at 120 °C. The Au-plated chip carrier feet and the Au busbar of the subcell were wirebonded using 25  $\mu\text{m}$  Al wire (Westbond Model 7476D-79). Following wirebonding, the subcell is electrically connected through the positive and

negative sets of the chip carrier feet and can be probed indirectly, reducing risk of damage to the epitaxial thin film comprising the cell active layers.

### Anti-reflection coatings

Applying an anti-reflection coating (ARC) to the subcells is the final step in processing them for integration with the spectrum-splitting and concentrating optics. Each subcell has an ARC consisting of a single 50-176 nm thick layer of  $\text{TiO}_2$ , which has a refractive index intermediate to fused silica and the III-V cell materials. The ARCs were deposited via electron beam evaporation. The thickness of each layer was optimized in the wave optical design software OpenFilters [58] to minimize in-band reflection out to  $30^\circ$  angle of incidence. The optimization incorporated refractive index  $n$  and extinction coefficient  $k$  data characterized by Kevin Chen during a Summer Undergraduate Research Fellowship (SURF) using electron beam evaporation, x-ray reflectometry, and ellipsometry. The designed and experimental thickness values are recorded in Table 4.2. Reflection curves for each of the seven subcells are plotted as simulated in Fig. 4.2. The reflections at each of the AR coated surfaces collectively average to less than 1% in band, with maximal values of 3%.

Table 4.2: PSRLP100v2 subcell anti-reflection coating properties

$E_g$ (eV)	Design $t_{\text{TiO}_2}$ (nm)	Experimental $t_{\text{TiO}_2}$ (nm)
2.10	50	50
1.78	69	71
1.54	86	86
1.42	99	99
1.15	118	118
0.94	142	142
0.74	176	176

## 4.4 Circuit and mechanical component design and prototyping

In addition to the subcells and optics, circuit and mechanical components are necessary for submodule integration and power extraction. We will outline each of these components and their use before describing the final prototype integration.

### Printed circuit board

A printed circuit board (PCB) is important to physically isolate the subcells on chip carriers from other wiring and facilitate independent electrical connection of

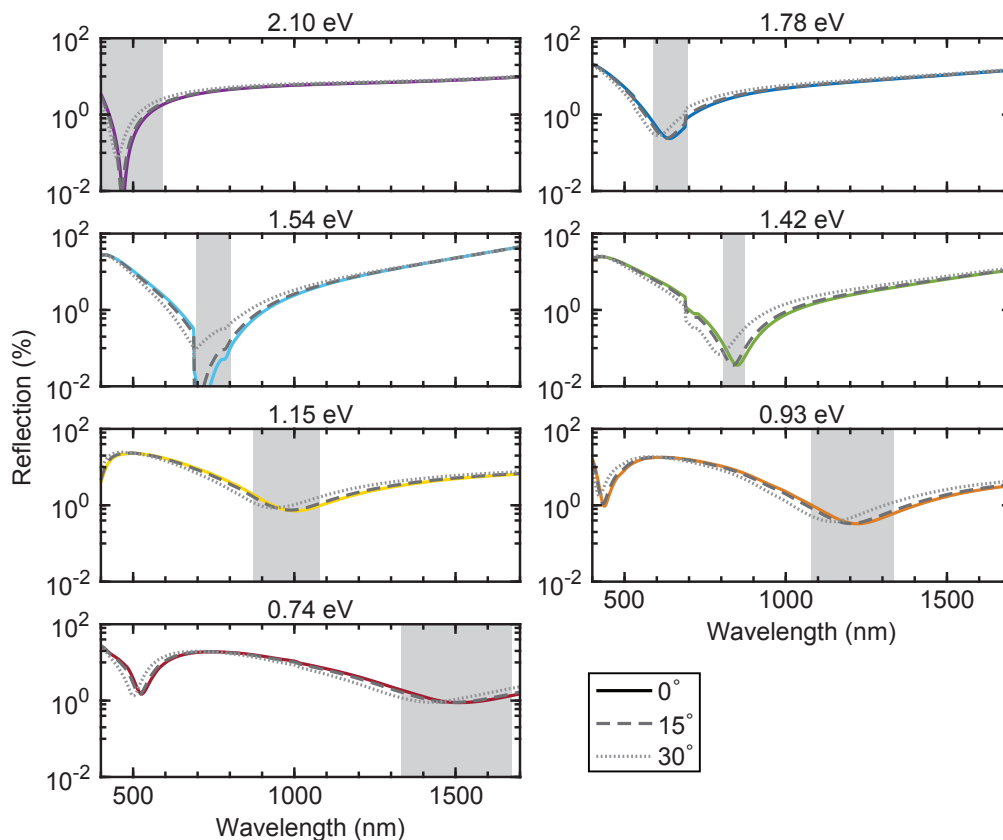


Figure 4.2: Simulated reflection from each of the AR-coated subcells as integrated in the prototype. Shaded gray regions indicate the subcell design band across which all subcells demonstrate  $<1\%$  reflection at most wavelengths. Solid, dashed, and finely dashed lines indicate  $0^\circ$ ,  $15^\circ$ , and  $30^\circ$  angles of incidence, respectively.

the bandgaps. Additionally, the PCB provides an electrical interface between the submodule and adjacent submodules, as well as between arrays of submodules and power conditioning components for eventual power combination and two-terminal power output to the electrical grid. Power conditioning and circuit topology will be discussed later in Chapter 6, and we will restrict our focus here to a single submodule PCB.

The PCB is shown in Fig. 4.3, both schematically and as prototyped. Independent traces run from the positive and negative terminals of each subcell to an individual pin of a surface mount connector (Molex Model 104141-1010) for a ribbon cable or freestanding wires (32 AWG). These cables will attach adjacent submodules in series directly or in parallel by use of an off-PCB connector. During testing, the output from each of the connector pins can be used to probe and measure each subcell independently. In addition, subcells can be wired in series to simulate the

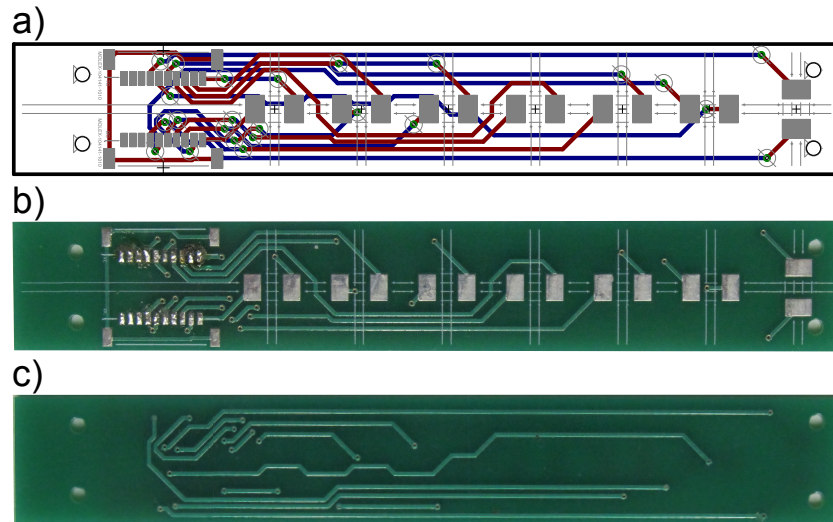


Figure 4.3: Submodule printed circuit board to electrically contact each of the subcells in a single repeat unit. (a) Board design schematic generated in EaglePCB. (b) Front and (c) back of the fabricated PCB based on the design of (a). Pads for a 10-pin external wire connector are at the far left, and bandgaps increase monotonically moving right along the circuit board.

performance of a monolithic multijunction comprised of similar bandgap absorbers constrained by current matching. Thus, the PCB provides a facile, flexible method of testing the subcells while keeping them mechanically isolated from electrical probes.

#### **Light pipe-to-subcell attachment holder**

Two additional pieces of hardware are needed to integrate the polyhedral specular reflector submodule. The first is a mechanical holder and positioner to align and attach each subcell to the  $1\text{ mm} \times 1\text{ mm}$  light pipe output face, and is shown in Fig. 4.4. The alignment tool was designed using standard optical translation (Newport Model TSX-1D) and rotation (ThorLabs Model PR01) stages in conjunction with a custom 3D-printed light pipe holder. The holder is attached to three linear translations stages and suspends the light pipe vertically above the subcell. The subcell is mounted to the rotation stage, which in combination with the light pipe degrees of freedom grants full control over alignment of the two pieces.

#### **Light pipe-to-filter stack attachment holder**

The second piece of alignment hardware needed for integration is a tool to mate each light pipe to the filter stack during attachment, providing both rotational alignment

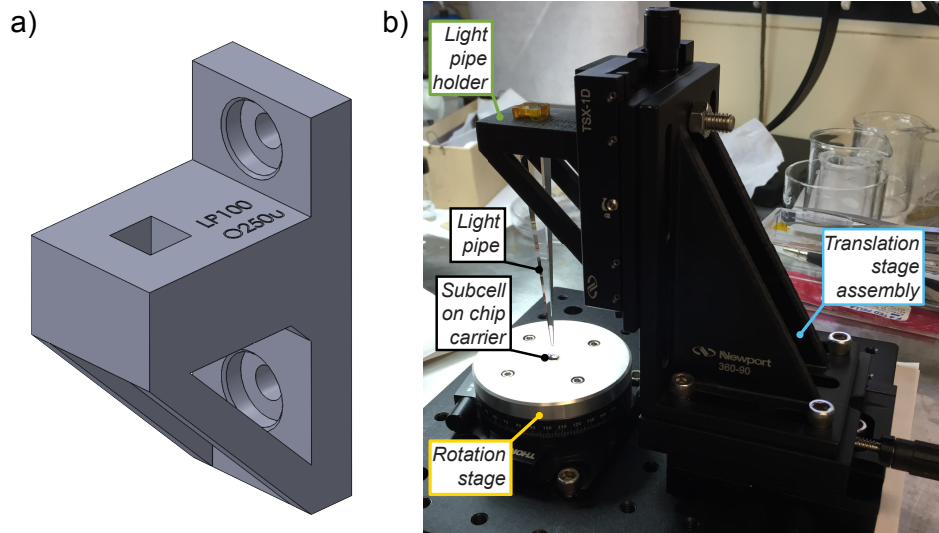


Figure 4.4: Light pipe-to-subcell attachment holder (a) as designed for 3D printing and (b) as integrated with linear and rotation stages. Three linear stages provide lateral alignment and height adjustment, and one rotational stage provides azimuthal alignment.

and stability before the interfacial adhesive (PDMS) is cured. This holder is shown in Fig. 4.5. The vertical arms are tapered to match the light pipe sidewalls, and they are slightly oversized to accommodate tape along the filter stack sides and at the light pipe base.

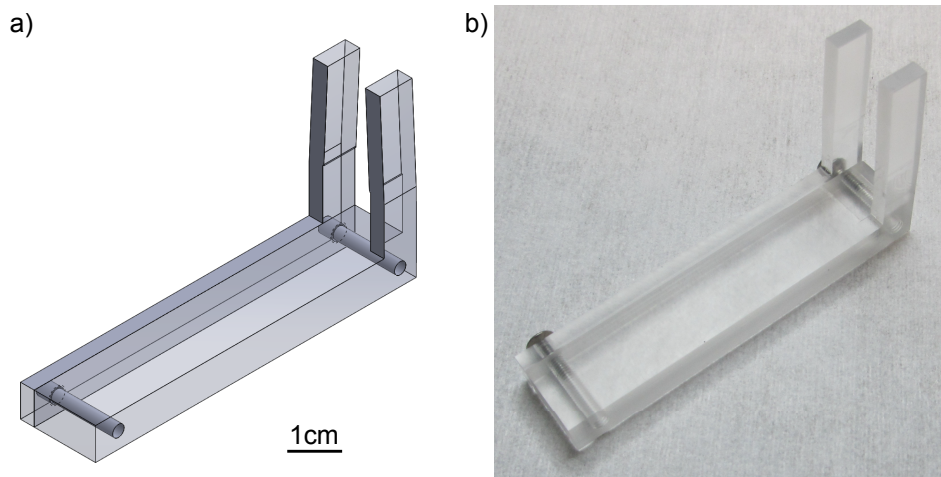


Figure 4.5: Light pipe-to-filter stack attachment holder (a) as designed for machining and (b) as machined in poly(methyl methacrylate) (PMMA). Two screws hold the left arm to the base and attached right arm to clamp the light pipe and filter stack firmly in place.

#### 4.5 Submodule prototype integration

With all of the components outlined we can now complete the submodule assembly.

##### **Light pipe-to-subcell attachment**

Each AR coated subcell on chip carrier is attached to a light pipe with PDMS. It is important that the PDMS layer is thin in order to prevent diverging light exiting the light pipe from spreading onto the subcell busbar and being lost by reflection. For subcells with an active area of  $1.2 \times 1.2$  mm coupled to the  $1 \text{ mm}^2$  light pipe output, a maximum gap thickness of  $100 \mu\text{m}$  can be tolerated. To achieve this gap thickness,  $0.5 \mu\text{L}$  PDMS is dispensed onto the cell active area and spun at 600 rpm for 60 s to conformally coat the surface with a thickness of  $\sim 20 \mu\text{m}$ . The wirebonds are robust to processing under these conditions.

The subcell is then secured on the rotation stage of the light pipe-to-subcell attachment holder, and the light pipe is brought down vertically into contact with the PDMS. There is a large change in reflection when the light pipe contacts the PDMS, which is visible by looking down the light pipe from above. The light pipe can then be aligned to the cell top contact pattern using the micropositioner stages, with alignment feedback given by the symmetry of the top contact pattern visible through the light pipe. Fig. 4.6 shows a well-aligned contact pattern view looking down through the light pipe.

With light pipe and subcell aligned, the PDMS interfacial layer needs to be cured. Avoiding thermal expansion that would cause an increase in separation between the light pipe and subcell is critical, so we locally applied heat using a heat gun and a thermocouple for temperature feedback (Fig. 4.7). The PDMS was heated to  $80 \pm 10 \text{ }^\circ\text{C}$  for 40 minutes to cure. Following the cure, the PDMS layer is mechanically robust enough to support a freestanding subcell on chip carrier. We observe between  $8\text{-}89 \mu\text{m}$  thick PDMS by optical microscopy.

##### **Light pipe-to-filter stack attachment**

With subcells attached, the light pipes are ready for attachment to the filter stack. The  $1 \text{ cm} \times 1 \text{ cm}$  input face of the light pipe is first cleaned using acetone, isopropanol, and dry nitrogen in sequence. Kapton tape is applied on the sides of the filter stack and on the filter stack output faces adjacent to the position where the light pipe will be attached. This prevents PDMS from wicking onto the other optical faces of the filter stack and prevents the light pipe from sliding onto an adjacent empty face during the desiccation and cure steps. PDMS is dispensed onto the output face of the filter

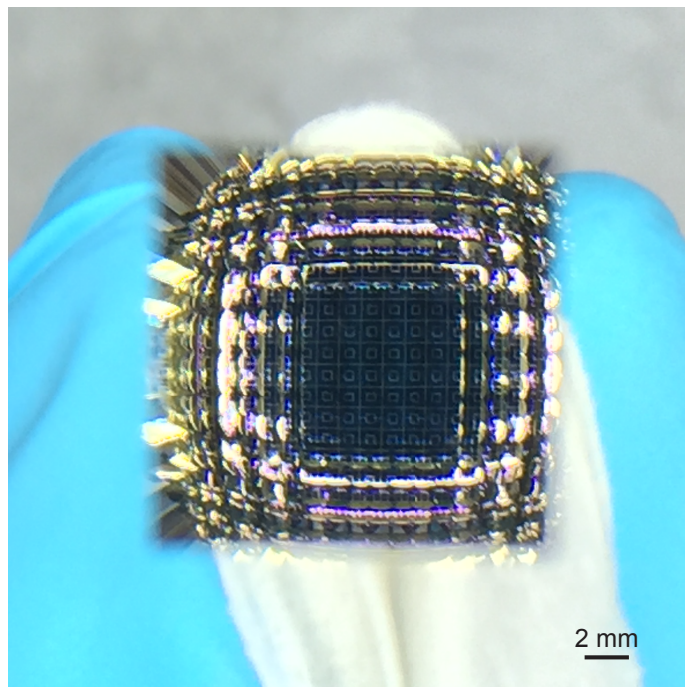


Figure 4.6: Top-down view through a light pipe of an attached subcell contact pattern demonstrating good alignment.

stack, and the light pipe is placed in contact with the PDMS and secured between the arms of the light pipe to filter stack alignment holder, as shown in Fig. 4.8. The entire optical assembly is placed into the desiccator to de-gas any entrapped bubbles and follows the attachment procedure of §4.2. This is repeated for each of the seven filters and corresponding subcells until the entire optoelectronic submodule has been fully assembled. The submodule spectrum splitting photovoltaic submodule is ready for characterization.

#### 4.6 Concluding remarks

Submodule characterization will be discussed in Chapter 5, but we will first make some qualitative observations about the integrated submodule of Fig. 4.1c. Looking through the structure at moderate angles to interfaces is a good identifier of any air gaps at those interfaces because total internal reflection will occur if an air gap exists. We see no such air gaps in our structure. Similarly, minimal scattering is visible from the structure bulk and only sparsely visible along faces and edges of the optics. Consequently, we expect comparable performance in the integrated submodule as compared to multiplying the optical performance by wavelength of the individual optical components.

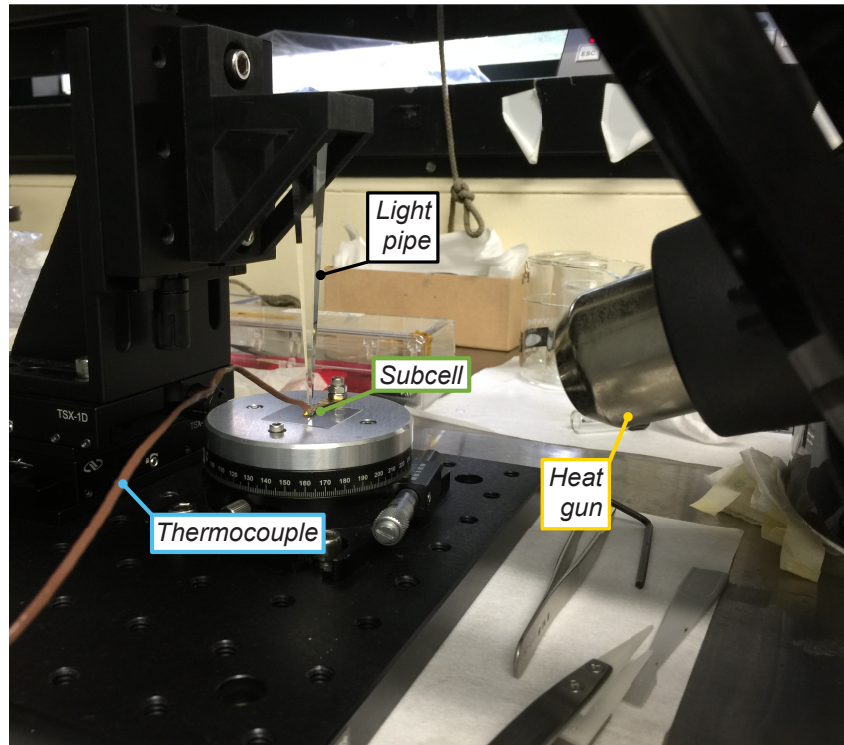


Figure 4.7: Light pipe-to-subcell interfacial adhesive cure. The cure is performed by locally heating the PDMS to 80 °C to minimize thermal expansion effects that would otherwise misalign the subcell to the concentrator and increase the PDMS layer thickness.

Additionally, the submodule was not integrated with the printed circuit board in this prototype submodule. It was not deemed critical to assessing the submodule performance with demonstrated negligible resistance contributions in past prototype iterations. Moreover, the long light pipes with relatively small interfacial area provide less mechanical support than previous iterations with lower concentration secondary concentrators. While external mechanical supports are fully capable of providing stability, we chose to forego adding them and the PCB to prevent the situation where the supports adversely impacted the optical performance.

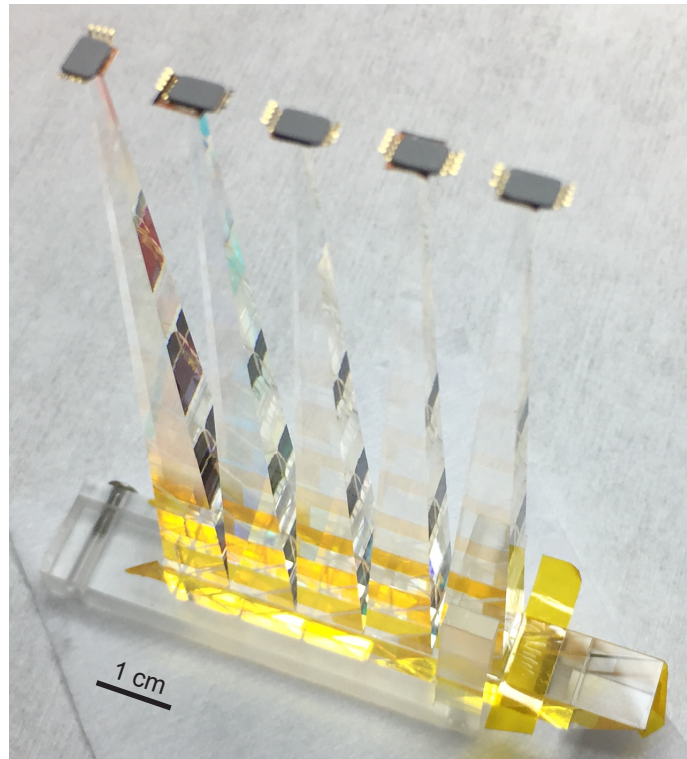


Figure 4.8: Light pipe-to-filter stack attachment for the fifth light pipe and subcell (1.15 eV InGaAsP). The light pipe being attached is clamped between the arms of the attachment holder. Kapton tape to prevent overflow of PDMS can be seen along the sides of the filter stack and on the adjacent sixth filter face at the bottom right of the image.

*Chapter 5***CHARACTERIZATION OF SPECTRUM SPLITTING  
PHOTOVOLTAIC SUBMODULES**

The previous chapter detailed integration and assembly of a polyhedral specular reflector submodule prototype. Here we will discuss the characterization of the integrated device and compare the performance of each component to its design values. We outline future research directions with the greatest potential to effect efficiency enhancement.

**5.1 Optoelectronic characterization system**

The spectrum splitting and concentrating optics, subcells, and integrated submodule were all characterized using the experimental system shown in Fig. 5.1. A super-continuum laser source (Fianium Model SC400) provides collimated broadband illumination from 400 nm to 1700 nm for measurement. This broadband light is coupled into a monochromator (ThermoOriel Instruments Model 77700) equipped with a filter wheel for single wavelength isolation. The monochromatic illumination beam is chopped into a square wave at a frequency between 10-100 Hz to allow steady-state background illumination and electrical line signals to be filtered out by the lock-in amplifier (Stanford Research Systems Model SR830). A portion of the chopped beam is split off to a power reference photodiode to monitor instantaneous variations in the laser intensity. This allows non-simultaneous measurements of the device under test (DUT) and reference. The remainder of the chopped beam is sent through a beam expander to increase illumination uniformity and fill a precision aperture before reaching the DUT. The precision square aperture ensures that the beam precisely fills the DUT illumination aperture so that (i) the DUT and reference can each be precisely aligned to the incident illumination, (ii) the performance of the DUT is not over-predicted by failing to illuminate the sidewalls of the sample where loss is expected to be greatest, and (iii) a reference measurement does not over-predict the incident spectrum intensity by collecting more photons than the DUT. Each measurement is referenced to a set of calibrated Si and Ge photodiodes (Newport 818-ST8-UV and 818-ST2-IR, respectively) placed immediately behind the precision aperture. The specific optical configuration and calculation for each of the DUTs will be further explained in subsequent subsections.

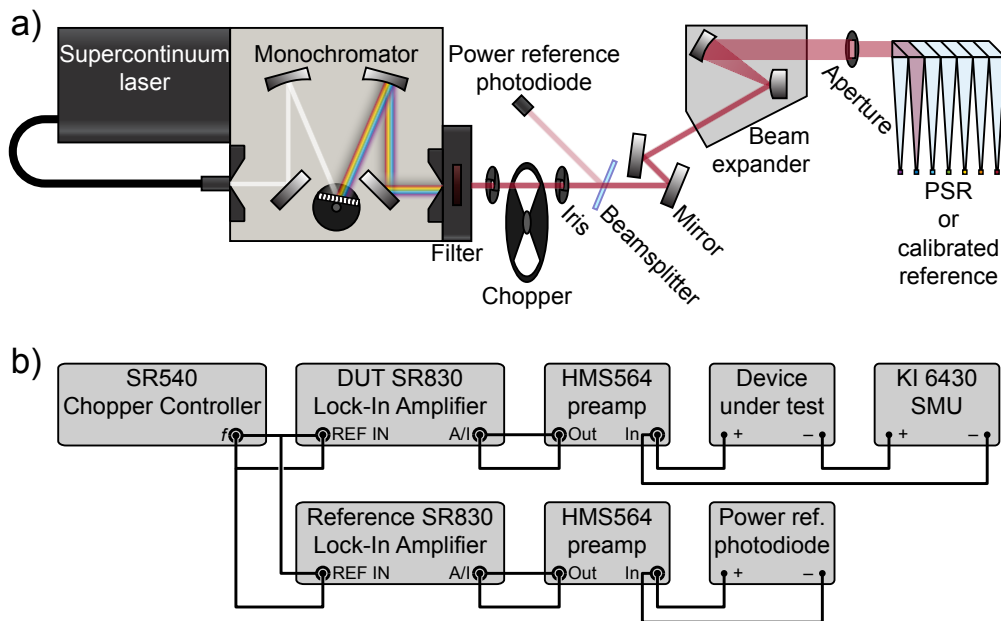


Figure 5.1: Spectrum splitting photovoltaic optoelectronic characterization system. (a) Schematic of the light path and optical components used to characterize individual optical components, free-standing subcells, and integrated PSR submodules. (b) Electrical hardware connection diagram outlining signal amplification, sample biasing, and power reference measurement.

The measurement electronics are an additional critical component of the general measurement setup and are shown in Fig. 5.1b. We are in all cases interested in device current collection at short circuit. Generally, the external circuit presents some electrical impedance to the DUT, and the operation point of the device will be where the impedance curve intersects the device current-voltage curve. This intersection typically occurs at a small non-zero voltage for a solar cell. Consequently, in order to measure the current at short circuit, we must impose an external voltage on the cell. A Source Measure Unit (SMU) (Keithley Instruments Model 6430) was used to zero the bias across the sample. Current produced by the DUT is passed to a preamplifier (HMS Elektronik Model 564) and transformed into a voltage signal with a typical gain of  $10^5$ . This voltage signal is monitored by the lock-in amplifier. The lock-in amplifier also monitors the chopping frequency from the chopper controller (Stanford Research Systems Model SR540) and uses the chopping frequency to isolate the DUT AC response to the chopped laser signal from any steady state DC response and AC line noise. Prime chopping frequencies were selected to eliminate the likelihood of higher harmonics interfering with the primary signal.

### Uncertainty estimation

The characterization system has high precision. Fig. 5.2 shows the repeatability error of the optical system across the wavelength range of interest. Eight measurements were made on both the Si and Ge calibrated reference photodiodes to determine the standard deviation ( $1\sigma$ ). There is a spike in uncertainty at the laser peak emission wavelength ( $\sim 1090$  nm), as well as across the water O–H absorption band (1350–1400 nm), where frequent fluctuations are expected to occur. Additionally, the uncertainty is slightly larger at the shortest wavelengths ( $< 500$  nm) where the laser intensity is lowest. Finally, Weighting the uncertainty by the power in the AM1.5D standard reference spectrum yields 0.58% broadband uncertainty, after accounting for the two required measurements of the incident and transmitted or reflected spectrum. This value is the relevant error for all of the optical efficiencies reported hereafter.

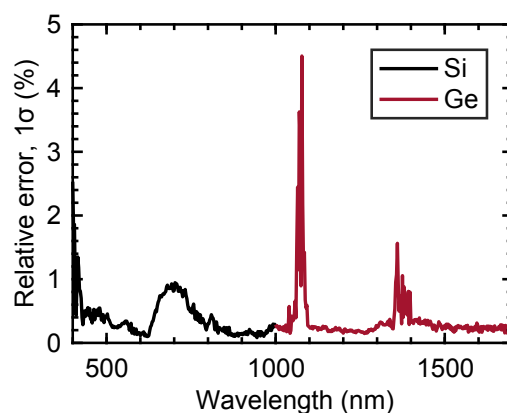


Figure 5.2: Repeatability error of the optical characterization system. The plot shows one standard deviation from each measurements each of the calibrated reference Si and Ge photodiodes. The crossover at 1000 nm is consistent with all reported data and minimizes the uncertainty in the measurement. Power-weighting by the AM1.5D solar spectrum yields 0.6% uncertainty across the entire measurement range.

The Si and Ge photodiodes are calibrated to within  $\pm 2\%$  accuracy. This is a systematic error not expected to be normally distributed about the measured values. Consequently, we report it separately. For the external quantum efficiency (EQE) and current-voltage ( $I$ – $V$ ) measurements that reference the calibration value to determine the absolute performance of a device under test, the uncertainty contains both the randomly distributed repeatability error of  $\pm 0.58\%$  and the uniform systematic error of  $\pm 2\%$ .

### Broadband anti-reflection coating

We characterized the AR coating transmission as integrated with the filter stack, which incorporates all losses associated with the integrated optics. Characterization data of the AR coating alone were provided by Reynard Corp. and were used to decouple the spectrum splitting efficacy of the filters stack from the front surface Fresnel reflection loss of the AR coating. This approach allowed both a thorough integrated measurement and a robust experimental probe into the individual optical component efficiency without limiting the AR coating performance by the uncertainty in our measurement system, which is large relative to the Fresnel loss.

### Filter stack

The transmission of integrated filter stack including the front aperture broadband anti-reflection coating was characterized as a function of wavelength at each filter output position. The calibrated photodiodes used for the reference measurement were placed at the output face of the filter stack and aligned to each filter by maximizing the short circuit current collected at a wavelength in the center of the filter band. The raw transmission of the  $i^{\text{th}}$  filter can be calculated from these measurements by

$$T_i(\lambda) = \frac{I_i^{\text{DUT}}(\lambda, t_{\text{DUT}})I_i^{\text{power}}(\lambda, t_{\text{ref}})}{I_i^{\text{ref}}(\lambda, t_{\text{ref}})I_i^{\text{power}}(\lambda, t_{\text{DUT}})}, \quad (5.1)$$

where  $I_i^{\text{DUT}}(\lambda, t_{\text{DUT}})$  is the lock-in amplifier measured current at the output of the  $i^{\text{th}}$  filter as a function of wavelength and measurement time,  $I_i^{\text{ref}}(\lambda, t_{\text{ref}})$  is the current at the input to the filter stack, and  $I_i^{\text{power}}(\lambda, t_{\text{DUT}})$  and  $I_i^{\text{power}}(\lambda, t_{\text{ref}})$  are the power reference photodiode currents measured simultaneously with the output and input measurements, respectively.

There is a Fresnel reflection in the component measurement that will not be present in the integrated submodule at the filter output face where a light pipe secondary concentrator will be attached. We correct for this Fresnel reflection to calculate the AR coated filter stack transmission by

$$T_i^{1F}(\lambda) = T_i(\lambda) \frac{1}{1 - R_F}, \quad (5.2)$$

where

$$R_F = \left| \frac{n_1 - n_2}{n_1 + n_2} \right|^2, \quad (5.3)$$

$n_i$  is the refractive index of the  $i^{\text{th}}$  medium (fused silica or air), and we assume normally incident light. This is a fairly good assumption both in characterization

and as the submodule is envisioned to be used in practice.

### Light pipe

The light pipe transmission was characterized similarly to the filter stack transmission with two notable exceptions. First, the assumption of near-normal incidence Fresnel reflection at the exit face of the light pipe is invalid. Concentrating optics necessarily trade off concentration with angular spread [70]. The mathematical relationship between the two is given by

$$A_{in}n_{in}^2 \sin^2(\theta_{in}) \leq A_{out}n_{out}^2 \sin^2(\theta_{out})$$

$$\frac{A_{in}}{A_{out}} = C \leq \frac{n_{out}^2 \sin^2(\theta_{out})}{n_{in}^2 \sin^2(\theta_{in})}. \quad (5.4)$$

The angular spread at the light pipe output is  $30^\circ$  in design, which will lead to significantly higher Fresnel reflection from the photodiode front surface than at normal incidence. Additionally, any misalignment of the optic will lead to a larger angular spread at the output. Photons exceeding the critical angle in fused silica ( $\sim 42^\circ$ ) will totally internally reflect back toward the light source and fail to be collected. To ensure neither of these effects distorts the collected signal, the light pipe is coupled directly to the output detector through a thin polydimethylsiloxane (PDMS) layer, which has a nearly identical refractive index to fused silica. The PDMS layer conforms to the surfaces of the light pipe and photodiode, which eliminates the air gap between them and mitigates the associated reflections. Consequently, this layer nearly perfectly transmits photons from the light pipe exit to the calibrated reference photodiode surface for measurement.

Use of a high refractive index interlayer leads to the second violation of assumptions made when measuring the filter stack: that the response of the reference photodiode is the same when measuring the input signal to the DUT and the output signal from the DUT. Placing the reference photodiode in contact with PDMS changes the reflection from the front surface and requires a correction. This correction factor is generated by measuring the transmission according to equation 5.2 with the PDMS on reference photodiode as the DUT <sup>1</sup>. Letting  $f_{PDMS} = T_{PDMS}$  on the reference photodiode, the transmission of the light pipe can be calculated from measured

---

<sup>1</sup>It is important to ensure that both surfaces of the PDMS layer are flat to avoid changing its scattering characteristics when measured on the calibrated reference photodiode and when compressed between the light pipe and the photodiode.

values by

$$T_{\text{LP}}(\lambda) = \frac{I_{\text{LP}}^{\text{PDMS}}(\lambda, t_{\text{DUT}}) I^{\text{power}}(\lambda, t_{\text{ref}})}{I^{\text{ref}}(\lambda, t_{\text{ref}}) f_{\text{PDMS}} I_{\text{LP}}^{\text{power}}(\lambda, t_{\text{DUT}})}. \quad (5.5)$$

We correct for the Fresnel reflection at the input face of the light pipe as before, since it will be coupled to the filter stack using a thin PDMS adhesion layer. Additionally, the PDMS correction factor contains a Fresnel reflection at the front PDMS surface that is now coupled to the light pipe. The resulting Fresnel-corrected light pipe transmission is

$$T_{\text{LP}}^{1F}(\lambda) = T_{\text{LP}}(\lambda) \frac{1 - R_{F,\text{PDMS}}}{1 - R_{F,\text{FS}}}. \quad (5.6)$$

## 5.2 Performance of spectrum-splitting and concentrating optics

The simulated and experimental optical performance of each of the submodule components can be seen plotted in Fig. 5.3. All inset scale bars are 1 cm, and coloring and line styles are consistent throughout all four subfigures. Experimental data were acquired every 2.5 nm, but markers are plotted every 25 nm for clarity.

The performance of the broadband AR coating is shown in Fig 5.3a, as characterized and simulated by Reynard Corp. The coating shows a close match between experiment and simulation, and was experimentally characterized at 98.5% optical efficiency (equation 3.2), versus 98.8% modeled. The inset shows a photograph of the AR coating on the fused silica substrate as characterized. Minimal loss is observed relative to the design, and existing loss is attributable to a slight deviation in thickness and refractive index of a subset of the deposited layers.

Fig. 5.3b shows the band allocation of the filter stack. The band cutoff wavelengths are well aligned to the design bands. Minimal sub-bandgap reflection is observed, which would direct photons into a cell where they could not be converted into electrical power. The integrated filter stack has an optical splitting efficiency of 88.1%, versus a modeled value of 92.0% excluding absorption in the fused silica. The inset shows the integrated filter stack with top broadband AR coating and visible wavelength splitting from ambient room lighting at the top two filter output faces. The largest portion of the optical losses comes from photon misallocation. The primary contribution to this effect comes from the corners of the filter faces. Each prism relies on total internal reflection to confine light at the sidewalls, making every face of the filter stack a critical optical face. In order to hold the prisms during filter deposition, each piece was suspended on holder arms that touched the four corners of the filter face. The holder caused slightly nonuniform deposition at each of these corners, resulting in regions of reduced deposition thickness over

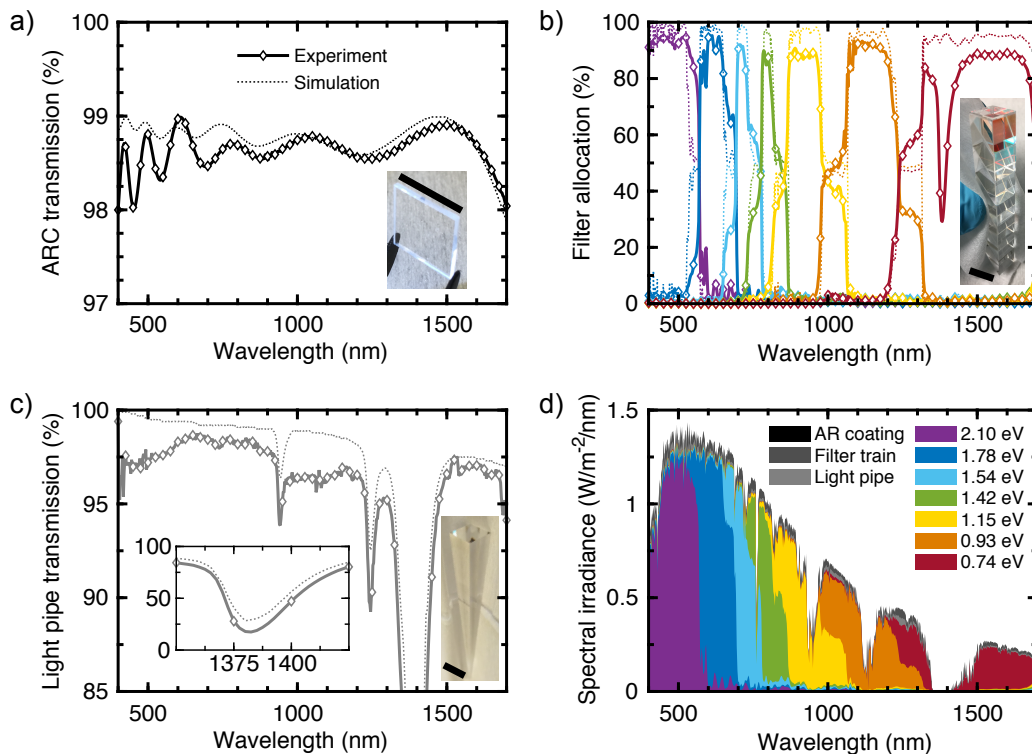


Figure 5.3: Simulated (dashed) and experimental (solid) performance of prototype polyhedral specular reflector components. Scale bars are 1 cm. Data were collected every 2.5 nm. Markers are plotted every 25 nm for clarity. (a) Anti-reflection coating transmission. (b) Filter assembly allocation. (c) 100 suns light pipe concentrator transmission. (d) AM1.5D spectral irradiance optical allocation by submodule component.

approximately 5% of the filter area. These regions contribute both to reflection of sub-band light into higher bandgap cells and transmission of in-band light to lower bandgap cells. Additional losses come from misalignment of the prisms to one another during optomechanical adhesion, as well as misalignment of the light pipes to the filter train.

Fig. 5.3c shows the transmission of the light pipe. The left inset shows a subset of the spectrum where a large O–H stretch absorption band causes the transmission to dip significantly. This absorption mechanism is present in water molecules in the atmosphere, and, consequently, it detracts negligibly from the submodule performance. Each light pipe has an optical efficiency of 97.4%, slightly lower than the modeled value of 98.9%. Experimental losses are primarily due to spectrally-independent microscale chips along the light pipe corners and scattering at adsorbed dust on the surfaces, which more strongly impacts shorter wavelengths.

Multiplying the AR coating, filter stack, and light pipe optical efficiencies yields an overall optical efficiency of 84.5%, relative to 89.9% predicted by optical modeling. As a benchmark, this experimental optical efficiency is comparable to many concentrating lenses employed in conventional concentrating photovoltaics [63], [71], [72]. The split spectral irradiance into each of the cell bands is shown in Fig. 5.3d, along with optical losses in each of the three aforementioned optical components. Clear band delineation can be seen, with the vast majority of photons reaching a cell in which they can be usefully absorbed, as is evident from the high optical efficiency.

### 5.3 PSR submodule current collection

With all of the individual optics characterized it is now left to us to understand how they couple to the subcells to produce electrical current. The external quantum efficiency (EQE), or incident photon-to-current efficiency (IPCE), is the fraction of incident photons that are converted to electrical current at a given wavelength. The EQE can be calculated from the measurements described in §5.1 by replacing  $T_i$  with  $EQE_i$  in equation 5.1, where the device under test is now a solar cell rather than the calibrated reference photodiode.

Fig. 5.4a shows the EQE of the integrated PSR submodule including optical losses, as well as the net optical transmission in each subcell band. In addition to the previously discussed optical transmission losses, the EQE curves incorporate (i) the coupling efficiency from the light pipe into the active area of the subcell, which includes (a) the Fresnel reflection at the subcell front surface, (b) the reflection from the top metallic contact electrode, and (c) light coupled outside of the cell active area; (ii) parasitic absorption losses in inactive semiconductor layers and at the back mirror; (iii) unabsorbed photons due to insufficient absorber thickness or low back mirror reflectivity; and (iv) steady-state recombination of carriers.

#### Contact grid obscuration

The top electrode geometry was optimized to balance the trade-off between light rejection by the metallized area and resistive loss during current collection, and the optimization procedure is described in detail in §2.1. Experimental contact geometries were optimized with 25  $\mu\text{m}$  fingers and 100, 50, and 25  $\mu\text{m}$  wide external busbars as depicted in Fig. 5.5. The relatively large finger width drives mutual convergence of the GaAs-based subcells to a single finger, while the InP-based subcells optimize to three fingers, resulting in a power-weighted average 6.12% obscuration and the subcell-specific obscuration fractions listed in Table 5.1.

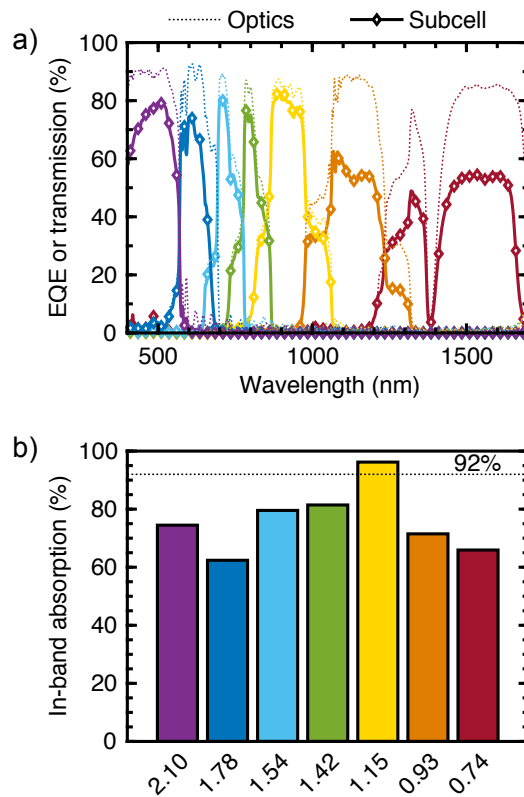


Figure 5.4: Current collection in the PSR. (a) Optical transmission in each subcell band (dashed) and subcell external quantum efficiency (solid) including optical losses. (b) Integrated in-band absorption relative to in-band optical transmission for each subcell bandgap and corrected for contact shadow losses. The dashed line at 92% represents the design target for each subcell.

This could be reduced to less than 2.5% obscuration by reducing the contact finger width to  $5 \mu\text{m}$ .

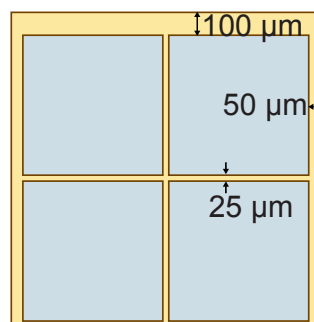


Figure 5.5: Optimized contact geometry for GaAs-based subcells with a minimum finger width of  $25 \mu\text{m}$ .

Table 5.1: PSRLP100v2 optimized subcell contact geometry parameters

$E_g$ (eV)	$n_{f,opt}$	$f_{shadow}$ (%)
2.10	1	4.64
1.78	1	4.64
1.54	1	4.64
1.42	1	4.64
1.15	3	8.94
0.94	3	8.94
0.74	3	8.94

### Subcell active area coupling efficiency

Light exiting the light pipes has a relatively high angular spread. Consequently, the illumination expands within the thickness of the interfacial PDMS layer. If the PDMS layer is sufficiently thick to allow light to reach the external busbar, light will be rejected and diminish the subcell EQE. The subcell active area ( $1.2 \times 1.2 \text{ mm}^2$ ) is oversized relative to the light pipe output ( $1 \times 1 \text{ mm}^2$ ). John Lloyd performed ray tracing simulations to determine that a PDMS thickness less than  $100 \mu\text{m}$  contributes negligible coupling loss for input angular spread up to  $3^\circ$ . We observe between 8-89  $\mu\text{m}$  thick PDMS by optical microscopy, and consequently expect coupling losses to be below the noise level in measurements of current collection.

### Subcell absorption

We will now consider parasitically absorbed and unabsorbed light making it into the subcells vis-á-vis Fig. 5.4b. Recall that the EQE for a state-of-the-art GaAs subcell [12] was analyzed to determine that 92% of in-band photons striking the active device area are converted into current, and that this fraction of ideal absorption was taken as a design target and simulation assumption for each of the III-V subcells (§3.3). Fig. 5.4b plots the fraction of ideal absorption after correcting for optical efficiency and contact obscuration for each of the subcells. While the 1.15 eV InGaAsP subcell exceeds this target, each of the other subcells falls substantially below 92% absorption. A key contributor to the 1.78 eV InGaP subcell is the slow absorption turn-on of the band edge, which causes the current collection to fall far below the optical input for wavelengths approaching the bandgap. Additionally, all of the GaAs-based subcells (1.42-2.10 eV) were designed assuming dual-pass absorption with a high reflectivity back mirror, and consequently have a thinner

absorber than an equivalent cell designed for single-pass absorption. Each of these subcells also has a 1.42 eV GaAs back contact layer to facilitate ohmic contact to the back electrode. The back contact layer will parasitically absorb above-bandgap light, which covers the full spectral range of these four subcells, leading to effectively single-pass absorption. Additionally, we expect this to have a decreasing effect with decreasing bandgap, as the GaAs layer will absorb higher frequencies more strongly. This is consistent with the experimental data with the exception of the aforementioned InGaP subcell. Future work aims to selectively etch away the GaAs layer leaving selective point contact regions, thereby substantially diminishing the parasitic absorption and allowing the back mirror to facilitate dual-pass absorption. For the InP-based subcells, there is no parasitically absorbing contact layer and gold should form an effective mirror for dual-pass absorption. We postulate that the 0.93 eV InGaAsP and 0.74 eV InGaAs subcells were grown with insufficiently thick absorbers, but lack sufficient data from Spectrolab to confirm this hypothesis.

#### 5.4 Power production and efficiency

Current-voltage device performance curves were collected for each of the subcells in the PSR submodule prototype in the dark and light under a Xenon arc lamp-based solar simulator (ABET Sun 2000) with  $1.3^\circ$  divergent illumination. The external quantum efficiency for each subcell was integrated with the AM1.5D solar spectrum to determine the device  $I_{sc}$ , and the measured light  $I$ - $V$  curve was vertically translated to align with the EQE-predicted  $I_{sc}$ . This translation corrects for intensity and spectral mismatch between the solar simulator spectrum and the standard reference spectrum. The resulting  $I$ - $V$  curves are plotted in Fig. 5.6a, and key performance parameters are recorded in Table 5.2.

#### Open circuit voltage and bandgap-voltage offset

First, we note that the subcell open-circuit voltage  $V_{oc}$  and maximum power point voltage  $V_{mpp}$  monotonically increases with bandgap. Each subcell produces greater voltage per photon than any lower bandgap and consequently justifies use of seven unique absorbers. Second, the bandgap-voltage offset  $W_{oc}$  is indicative of the quality of the device design and epitaxial material [73]. The  $W_{oc}$  is expected to be approximately 400 mV at one-sun injection levels for high quality III-V growth and should decrease by  $\sim 58$  mV per decade of concentration. The observed  $W_{oc}$  values are somewhat higher than expected at a concentration of 15-100 suns, which reflects (i) the non-uniform photon allocation and injection level as a function of

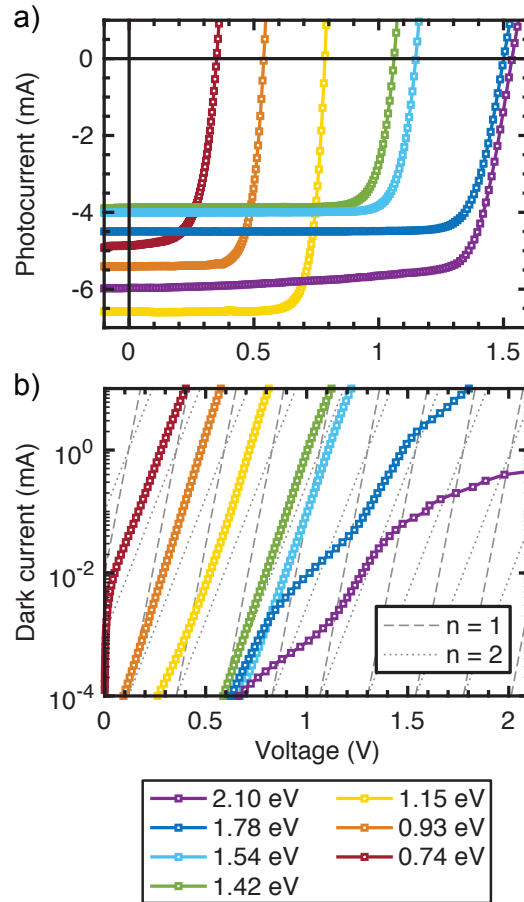


Figure 5.6: Submodule current-voltage device curves in the (a) light and (b) dark demonstrating 30.2% combined conversion efficiency.

bandgap and (ii) a significant fraction of the recombination at open circuit coming from non-radiative pathways. Fig. 5.6b provides some insight into the latter by comparison to the double diode model in equation 2.1. A slope parallel to the diode ideality  $n = 1$  grid indicates recombination occurs in the quasi-neutral region of the solar cell, which is typically dominated by radiative recombination for direct-gap semiconductors. A slope parallel to  $n = 2$  indicates recombination occurs in the depletion region at or near the junction, which is dominated instead by trap state-mediated non-radiative recombination. Each of the bottom five bandgaps exhibits an ideality between 1 and 2 without significant variation across the entire operational range, which likely indicates recombination dominated by a non-midgap trap state in the depletion region of the device. There is precedent for  $n$  closer to 1 for many of these bandgaps, and we expect that further refinement of the growth procedure will yield reduction in  $W_{oc}$ .

Table 5.2: PSRLP100v2 experimental cell performance parameters

$E_g$ (eV)	$V_{oc}$ (mV)	$W_{oc}$ (mV)	$I_{sc}$ (mA)	$FF$ (%)	$P_{mpp}$ (mW)	$\eta_{AM1.5D}$ (%)
2.10	1534	566	5.97	76.5	7.00	7.8
1.78	1501	277	4.94	82.5	5.57	6.2
1.54	1148	392	4.00	83.3	3.83	4.3
1.42	1061	359	3.88	82.1	3.38	3.8
1.15	784	331	6.58	80.6	4.16	4.6
0.94	540.	400.	5.41	74.6	2.18	2.4
0.74	350.	390.	4.87	60.7	1.04	1.2

### Short circuit current

Third, the prototype PSR submodule collects  $35.2 \text{ mA/cm}^2$ , which is 83.1% of the design target and 66.3% of the total current available in AM1.5D. This is below the design target for the reasons discussed previously, and can be enhanced further by reducing the contact grid obscuration fraction via photolithography with reduced feature size and regrowing subcells with thicker absorber layers.

### Fill factor

Devices generally exhibit good fill factors, indicating low resistive loss. We expect increasing fill factor with bandgap, which holds true apart from the 1.78 eV and 2.10 eV subcells. The fill factors of the bottom five subcells are generally consistent with diode recombination with ideality between  $n = 1.6 - 2$ . This highlights the importance of suppressing non-radiative recombination, which could lead to 5-15 percentage point increases in fill factor across these subcells. The 1.78 eV InGaP subcell shows a series resistance roll-over above 2 mA in the dark current curves, which will tend to shift the maximum power point to lower voltage by  $\Delta V = IR$ , decreasing the fill factor. This indicates a mismatch between the contact grid optimization parameters and the physical device properties, in particular the emitter sheet resistance ( $R_{sh,emitter}$ ). Re-optimization with precisely characterized on-film values is expected to yield a boost of  $\sim 3\%$ . Lastly, the 2.10 eV AlInGaP subcell violates superposition between light and dark characterization, which generally arises from disparate current pathways in each testing regime[28], [29]. This can cause carriers to interact with different trap states, generate different local applied biases, and alter the effective series resistance of the device. Further material growth

and device development are needed to achieve comparable efficacy in this subcell relative to its bandgap.

### **PSR submodule efficiency**

Submodule efficiency divides the total power output from all subcells by the 90 mW AM1.5D illumination incident on the 1 cm<sup>2</sup> input aperture of the device. Totalling the subcell efficiencies in Table 5.2, we find an integrated submodule efficiency of 30.1%. Notably, it exceeds the world record performance of a single junction solar cell at any concentration[74], which have received an order of magnitude or more funding over a substantially longer time scale. While the prototype submodule efficiency falls short of current multijunction submodule (40.4%) [22] and spectrum splitting (38.5%) [23] records, it represents an unprecedented ability to divide the solar spectrum into many ( $\geq 6$ ) spectral bands with high net optical efficiency (84.5%). This in turn enables lower thermalization losses than any other multijunction prototype. The submodule demonstrates one of the highest open circuit voltage (1534 mV) of any reported single junction cell to date, if not the highest outright. Finally, the PSR submodule stands as a proof-of-concept prototype for a design capable of module efficiency well in excess of its peers.

### **5.5 Opportunities for efficiency enhancement**

There are many design, processing and fabrication opportunities that would enable substantially increased photovoltaic conversion efficiency. The quantitative impacts are presented for those within the scope of the current work, while notional or limiting impacts are presented for improvements that would require substantial design changes.

#### **Opportunities for optical efficiency enhancement**

The optical splitting system was not co-optimized with the subcell absorption characteristics (EQE) for historic reasons having to do with simultaneous development of the optical designs by Carissa Eisler at Caltech and inverted, epitaxial lift-off compatible cell growth development by Spectrolab, Inc. Instead, the nominal subcell bandgap was used as a target for filter cutoff. Optimally and intuitively, the filter cutoffs should lie at the wavelength for which the marginal power generated by a more highly absorbing but lower voltage low bandgap subcell equals that generated by a less highly absorbing but higher voltage high bandgap subcell. Such a design would be expected to give a 30% boost in current to the 1.54 eV AlGaAs subcell

by redirecting the poorly absorbed near-bandgap photons from the 1.78 eV InGaP subcell band, which translates to a 1.3 percentage point boost in the solar conversion efficiency. Limiting absorption to the highest EQE regions of each subcell could in principle enable absorption values in excess of the 92% absorption target, which was derived from the *broadband* absorption of a GaAs subcell.

Another opportunity for optical efficiency enhancement comes from the subcell antireflection coatings. Replacing  $\text{TiO}_2$  with  $\text{Nb}_2\text{O}_3$  reduces long wavelength absorption due to a reduced extinction coefficient  $k$  (Fig. 5.7) and can increase the optical efficiency of the InGaAs ARC by 0.8%. Gains for other subcells will be more modest, though multilayer or equivalent layer coatings could offer further improvement [75].

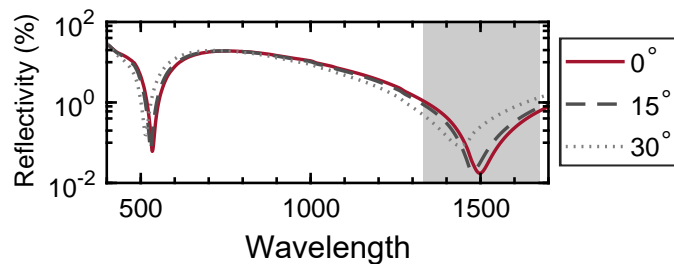


Figure 5.7: InGaAs 0.74 eV subcell  $\text{Nb}_2\text{O}_3$  antireflection coating performance.

### Opportunities for subcell performance enhancement

There is additional opportunity for efficiency enhancement via modification to the subcells themselves. Optimization of reduced finger width cell contact grids has the dual benefits of increasing current collection and reducing resistive losses, as discussed in §3.5. Optimizing for a finger width of  $5 \mu\text{m}$  predicts a 3.9% gain in current collection across the ensemble.

We expect that further inverted growth development by Spectrolab, Inc. should be able to improve the device quality and reduce the  $W_{oc}$  to close to 300 mV for all seven bandgaps. This is based on experimental  $W_{oc}$  values grown previously by Spectrolab in an upright cell configuration and the level of concentration exhibited by our system [73]. A  $W_{oc}$  of 300 mV has also been demonstrated at 1 sun illumination for a GaAs cell grown by Alta Devices [74]. A key contributor to that device achieving such a low  $W_{oc}$  is the incorporation of a high reflectivity back mirror for photon recycling within the subcell. Additional process development to incorporate low absorption, high reflectivity back mirrors presents low-hanging fruit for future work.

Current collection in the lowest two bandgap subcells is far below what was expected. Increasing these by optimizing the subcell thicknesses and back mirror reflectivity EQE of low bandgap subcells would increase the integrated efficiency by 1.1 percentage points.

New cell developments have occurred recently that expand the realistic bandgap design space. A 0.5 eV bandgap InGaAsSb cell was grown with  $>300$  mV  $V_{oc}$  at high concentration and  $V_{oc}$  of  $\sim 250$  mV at the concentration of the bottom cell in our spectrum splitting prototype [76]. This is particularly noteworthy as subcell ensemble bandgap optimizations conducted by Emily Warmann early in the project showed that the optimal bottom bandgap for ensembles with  $\geq 4$  subcells is at 0.5 eV [41].

## 5.6 Conclusion

We have demonstrated a prototype polyhedral specular reflector spectrum-splitting photovoltaic submodule with 30.1% photovoltaic conversion efficiency under the AM1.5D solar reference spectrum. Notably, this prototype submodule demonstrates 84.5% optical efficiency and is to our knowledge the first experimental demonstration of a converter with seven or more unique bandgap converters. Though somewhat bespoke to achieve maximum efficiency in its current embodiment, this submodule is a first demonstration of what could become a new class of high efficiency solar energy converter and drive down the levelized cost of electricity via high annual energy production.

*Chapter 6***DESIGN OF AN INDEPENDENTLY ELECTRICALLY  
CONNECTED SPECTRUM SPLITTING PHOTOVOLTAIC  
MODULE**

C. A. Flowers, C. N. Eisler, and H. A. Atwater, “Electrically independent sub-circuits for a seven-junction spectrum splitting photovoltaic module,” in *2014 IEEE 40th Photovoltaic Specialist Conference (PVSC)*, Jun. 2014, pp. 1339–1343. DOI: 10.1109/PVSC.2014.6925165,

©2014 IEEE

In the previous chapters we have designed and prototyped lateral spectrum-splitting photovoltaic submodules with electrically independent subcells targeting ultrahigh (>50%) efficiency and best-in-class annual energy production. Realization of the annual energy production gains associated with electrically independent subcells [16] requires electrically independent circuitry for each bandgap at the module level. Moreover, power conditioning components are needed to combine the electrically independent systems into a two-terminal output for interconnection with a load or utility distribution grid. We have designed such a system for a seven sub-cell spectrum-splitting module using commercially available electrical components. Modified detailed balance modeling of the subcells coupled with HSPICE circuit simulation results in 87.5% power-weighted average subcell-to-grid electrical efficiency. Additional analysis indicates electrical efficiencies in excess of 97% are possible with custom power conditioning components and appropriately designed contacts.

**6.1 Introduction**

Spectrum splitting has recently gained renewed interest as a means of significantly increasing both the peak efficiency of and total annual power produced by photovoltaic modules [14], [17], [77]. Lateral spectrum splitting may allow for module efficiencies in excess of 50%, which would mark a significant increase over the 35.9% concentrating photovoltaic module efficiency record as of this reporting. Recent work has quantified the benefit of removing the current-matching constraint of series-connected subcells in favor of independent electrical connection [16], [17],

[78]. This benefit can exceed 20% increased annual power generation for optimized ensembles of six or more semiconductor bandgaps. Realizing such electrical independence requires a circuit design tailored to the specific spectrum-splitting implementation.

We describe here one such circuit design to facilitate two-terminal AC output from a seven-junction module based on a polyhedral specular reflector (PSR), the optical design of which was reported in Eisler *et al.* [53]. In a single PSR submodule, shown in Fig. 6.1a, direct sunlight is incident on a primary compound parabolic concentrator (CPC), the exit of which illuminates a 45° angled parallelepiped. The angled faces of the parallelepiped are tiled with dichroic bandpass filters, each allowing the wavelength band allocated to a subcell to transmit through while reflecting other wavelengths further down the parallelepiped at approximately 90° angles. Transmitted light is concentrated further in a solid secondary CPC before reaching the subcell, which has a bandgap chosen to effectively convert the incident wavelength band. Filter pass bands are designed such that the majority of transmitted photons have energy above the illuminated subcell bandgap and below the next highest subcell bandgap, thereby minimizing thermalization losses. Submodules are tiled in a plane to comprise a module, a portion of which is shown from above in Fig. 6.1b.

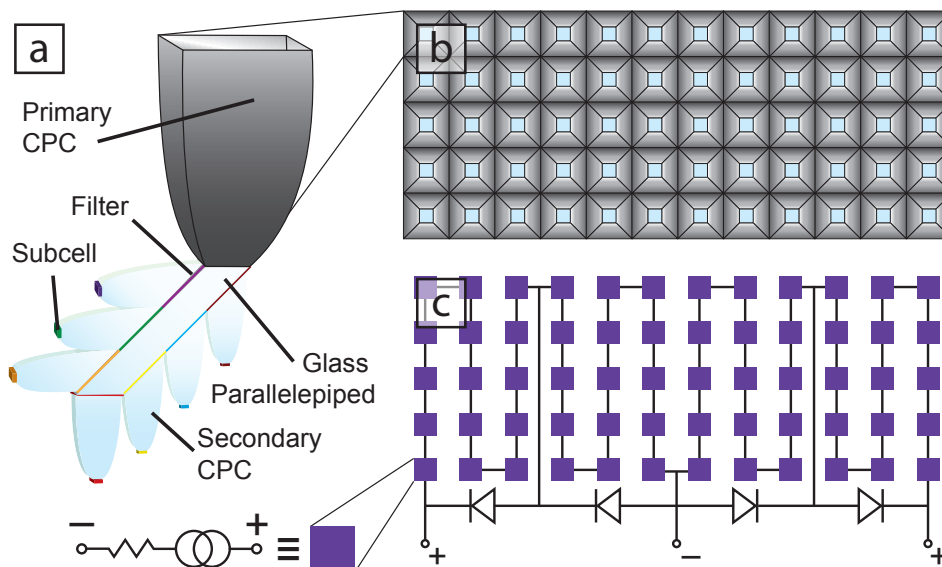


Figure 6.1: Transmissive PSR submodule with seven subcells, along with partial module and circuit schematics. Reprinted with permission from the copyright holder, ©2014 IEEE.

Subcells convert a spectral band into electrical current and deliver power with a

voltage proportional to the semiconductor bandgap. Full utilization of the generated electrical power requires an efficient electrical circuit consisting of (1) well designed contacts to extract current from individual subcells with minimal shadow losses, (2) series and parallel interconnected subcells to raise the voltage and current outputs to levels suitable for power conditioning, (3) power conditioning electronics to perform maximum power point tracking (MPPT) and (4) convert all subcell outputs to a common output voltage or current for subsequent combination and two terminal output. We perform contact, interconnect and bypass diode simulations and employ commercially available microinverters in the design of such a circuit. This allows facile matching of electrical grid AC voltage and phase, thereby accomplishing the Kirchoff voltage-matching criterion for power combination between parallel subcircuits. Simulation of the circuit utilizing this power-conditioning scheme allows us to map circuit efficiency versus concentration and subcell size. These data inform the physical implementation of the electrical system for a module using electrically independent connections to each bandgap.

## 6.2 Methods

The focus here is on module electrical design. However, this requires knowledge of all subcell output characteristics, which in turn are dependent on the optical properties of the PSR spectrum splitting element. The results of ray-tracing simulations developed in Eisler *et al.* [53], [56] were used to determine the photon flux incident on each subcell. Subcell device performance curves were calculated by de-rating the detailed balance efficiency by experimentally demonstrated material-dependent external radiative efficiencies (ERE), as discussed previously, [13], [79] and assuming a fraction  $f$  of the incident photon flux is converted to current at short circuit. Here we constrain our focus to  $ERE = 0.03$  and  $f = 0.9$ , which are consistent with 1D device physics simulations in AFORS-HET of each of the subcells considered [48].

Individual subcell  $I$ - $V$  curves from de-rated detailed balance calculations were converted to piecewise-linear current-controlled voltage source elements for simulation, and a lumped external resistance was placed in series with each subcell to account for the subcell top and back contacts, as well as the interconnect to the subsequent subcell (expansion of Fig. 6.1c). These interconnected subcells are wired in series and parallel to build up voltage and power in the optimal input range of the power conditioning equipment. STMicro STPS5045S bypass diodes with a typical leakage current of  $9 \mu\text{A}$  are placed around every 24 V substring to prevent operation of any

cell in reverse breakdown under shading conditions. Subcircuits are connected to microinverters for MPPT and output side voltage and phase matching.

An example subcircuit for the highest bandgap 2.13 eV subcell is shown in Fig. 6.1c. This subcircuit connects to the positive and negative input terminals of a single microinverter. The optimal input voltage (40-50 V) and power (300 W) ranges of the microinverter guide the overall circuit topology, where we assume use of PowerOne MICRO-0.3-I-OUTD-US-240 microinverters. Subcircuits are designed to provide each microinverter at least 86% and typically greater than 92% of the 300 W nominal rated input power for AM1.5D illumination conditions. This allows the expected annualized performance of the microinverter to be well represented by the 96.0% California Energy Commission (CEC) weighted efficiency. Matching the rated efficiency further enables the transient switching operation of the microinverter to be removed from the circuit simulation, such that a strictly DC steady-state simulation of the series-parallel and bypass diode network is performed in HSPICE, sweeping bias from short circuit to open circuit. The maximum power points from the resulting subcircuit I-V curves are used in conjunction with the microinverter efficiency to determine the efficiency for each subcircuit. Weighting each subcircuit by the respective number of microinverters and total power produced enables calculation of the module circuit efficiency, which is the ratio of total AC power delivered to the grid by all subcircuits to the total output power of all subcells. All simulations assume a contact resistivity of  $1 \times 10^{-4} \text{ } \Omega \cdot \text{cm}^2$ , consistent with prior literature [80].

### 6.3 Results and Discussion

A comprehensive module design requires a defined number of submodules, an interconnection topology, resistive losses, and the corresponding current, voltage and power production characteristics. The total number of subcells in the module was set to the fewest number for which an integer number of microinverters can receive voltage and power inputs in the optimal range. This enables the design to be as modularized as possible. For such a module, the subcell bandgap, maximum power point voltage, maximum power point current, the number of series and parallel subcells per subcircuit, corresponding subcircuit voltage and current, number of subcircuits at each bandgap, and subcircuit and total power output can be seen in Table 6.1. The specific PSR submodule considered employs 300 suns concentration and  $1 \text{ cm}^2$  subcells, and a full module incorporates 720 subcells at each bandgap. The high number of subcells per module is primarily driven by the number of series-connected low-bandgap subcells needed to accumulate voltage for a single

Table 6.1: Module interconnection circuit topology parameters using microinverters

$E_g$ (eV)	$V_{mpp}$ (V)	$I_{mpp}$ (A)	$N_{series}$	$V_{series}$ (V)	$N_{parallel}$	$I_{parallel}$ (A)	$N_{\mu inv}$	$P_{\mu inv}$ (W)	$P_{total}$ (W)
2.13	1.76	2.64	30	52.8	2	5.28	12	279	3346
1.84	1.47	1.58	30	44.1	4	6.31	6	278	1669
1.58	1.23	1.84	40	49.0	3	5.53	6	271	1628
1.42	1.07	1.44	45	48.0	4	5.77	4	277	1108
1.12	0.80	2.90	60	48.3	2	5.80	6	280.	1679
0.93	0.62	1.99	80	49.7	3	5.96	3	296	889
0.74	0.45	1.61	90	40.2	4	6.43	2	259	517

microinverter. However, this is a function of the power electronics design and not a fundamental constraint, so it could be reduced by using custom designed electronics.

#### **Point Design: 300 suns, 1 cm<sup>2</sup> subcells**

The lumped resistance in series with each subcell was varied over five orders of magnitude in successive simulations to map the resistance–efficiency space (Fig. 6.2). Circuit efficiency is plotted versus lumped resistance for all seven subcircuits, as well as for a power-weighted average. The peak in efficiency with negligible resistance is at 96%, set by the CEC weighted efficiency of the microinverter. The subcell contact geometry and corresponding resistive losses, interconnect losses, and bypass diode leakage impose a specific value of the lumped resistance and consequently determine the subcircuit efficiency. Conversely, achieving any particular circuit efficiency imposes a constraint on the maximum resistance that can be tolerated in designing the contacts and interconnects between the subcells, bypass diodes, and power conditioning electronics.

For the PSR considered, 87.5% circuit efficiency limits series resistance to no more than 0.045  $\Omega$  per subcell with subcells of identical series resistance, while 95% circuit efficiency gives only a 0.004  $\Omega$  budget. Considering subcells in a submodule mounted on a single printed circuit board (PCB), the subcell lumped series resistance is comprised of the following resistances: (i) back contact PCB trace and metallization, (ii) back contact resistivity, (iii) subcell emitter sheet resistance, (iv) front contact metallization, (v) top contact-to-PCB conductor wiring resistivity and PCB trace, (vi) interconnect wiring resistivity, and (vii) all associated solder and wire bonding resistivities.

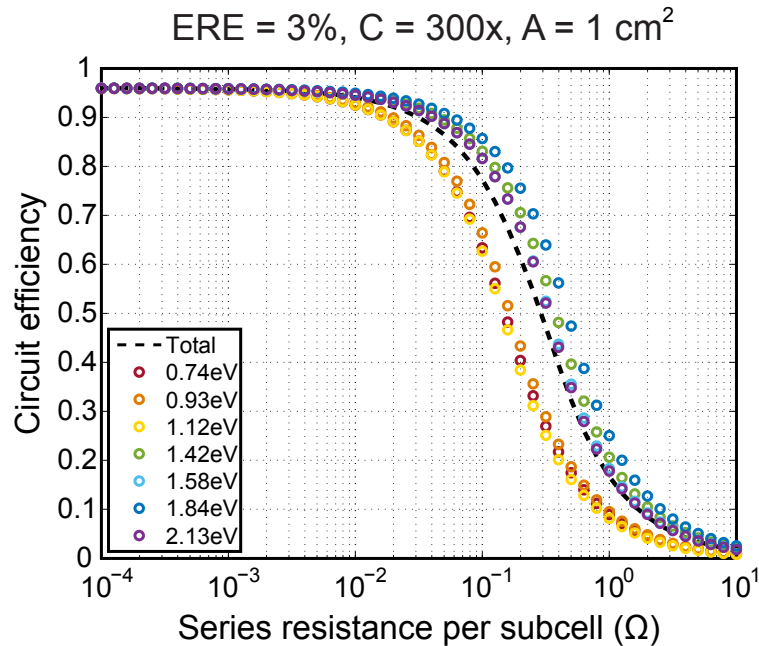


Figure 6.2: Module circuit efficiency versus lumped series resistance. Reprinted with permission from the copyright holder, ©2014 IEEE.

PCB trace thicknesses and widths, interconnect and top contact-to-PCB wiring gauges, and contact geometry were designed to enable the aforementioned lumped resistance per subcell in agreement with 87.5% circuit efficiency. Standard 1 ounce PCB copper thickness with 1 mm traces, wirebond-able 32 AWG copper contact-to-PCB conductors, and 12 AWG copper interconnects between adjacent submodules require less than ten percent of the maximum series resistance budget. This allows greater flexibility in design of cell contacts to minimize shadowing. Smaller gauge interconnect wiring can be used with minimal detriment, particularly with reduced concentration.

A geometrically constrained contact optimization was used to determine a local minimum in resistive losses in the contacts. This balances the losses due to lateral conduction in the subcell emitter layer, transport of carriers across the semiconductor-metal contact interface, and conduction through the metal contact fingers and busbar with the obscuration losses due to the contact pattern reflecting incident illumination away from the subcell. A breakdown of the various loss contributions in the contacts of each subcell is presented in Fig. 6.3. The latter so-called shadow loss is considered as part of the fraction of short circuit current,  $f$ , in the optical model and is not enumerated with the resistive losses here. Resistive losses in the busbar, contact fingers, emitter, and at the semiconductor-metal contact interface have de-

creasing relative importance. The contacts comprise the single largest resistive loss mechanism in the overall circuit. This is primarily a consequence of the currents generated at high concentration (300 suns) and large cell size (1 cm<sup>2</sup>). Reduction in subcell area will improve overall electrical performance as the resistive loss is proportional to the square of the current. The designed resistance values were fed into the HSPICE model along with a simple contact geometry optimization procedure to verify an overall circuit efficiency of 87.5% for 1 cm<sup>2</sup> subcells with a power-weighted average series resistance per subcell of 0.054 Ω. While this is greater than the 0.045 Ω mentioned previously to achieve 90% circuit efficiency, the optimization relaxes the constraint, assumed above, that the different bandgap subcells have identical external series resistance. This enables strong performance of the high power, high bandgap subcircuits to balance loss due to higher resistance in the low power, low bandgap subcircuits.

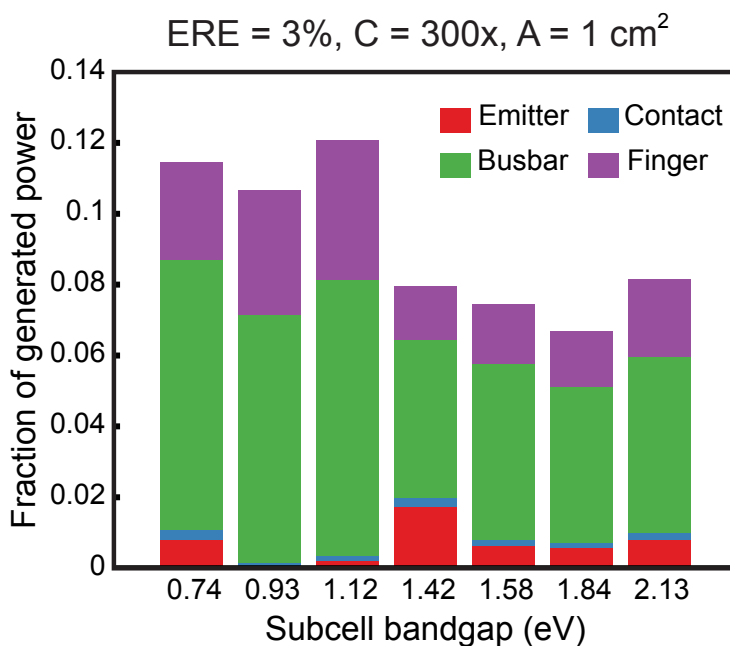


Figure 6.3: Subcell contact resistive loss contributions consistent with 87.5% electrical efficiency. Reprinted with permission from the copyright holder, ©2014 IEEE.

### Extended Design Space

Further simulations were performed to investigate additional combinations of concentration and subcell size. In practice, the tolerable series resistance makes the trade-off between contact grid resistance and shadowing overly constrained to achieve a high circuit efficiency with large (1 cm<sup>2</sup>) subcells. Increased power

electronics efficiency, decreased total concentration, or decreased subcell size allow a more facile trade-off. We leave the first to future studies and present data illustrating the impact of the latter two options in Fig. 6.4.

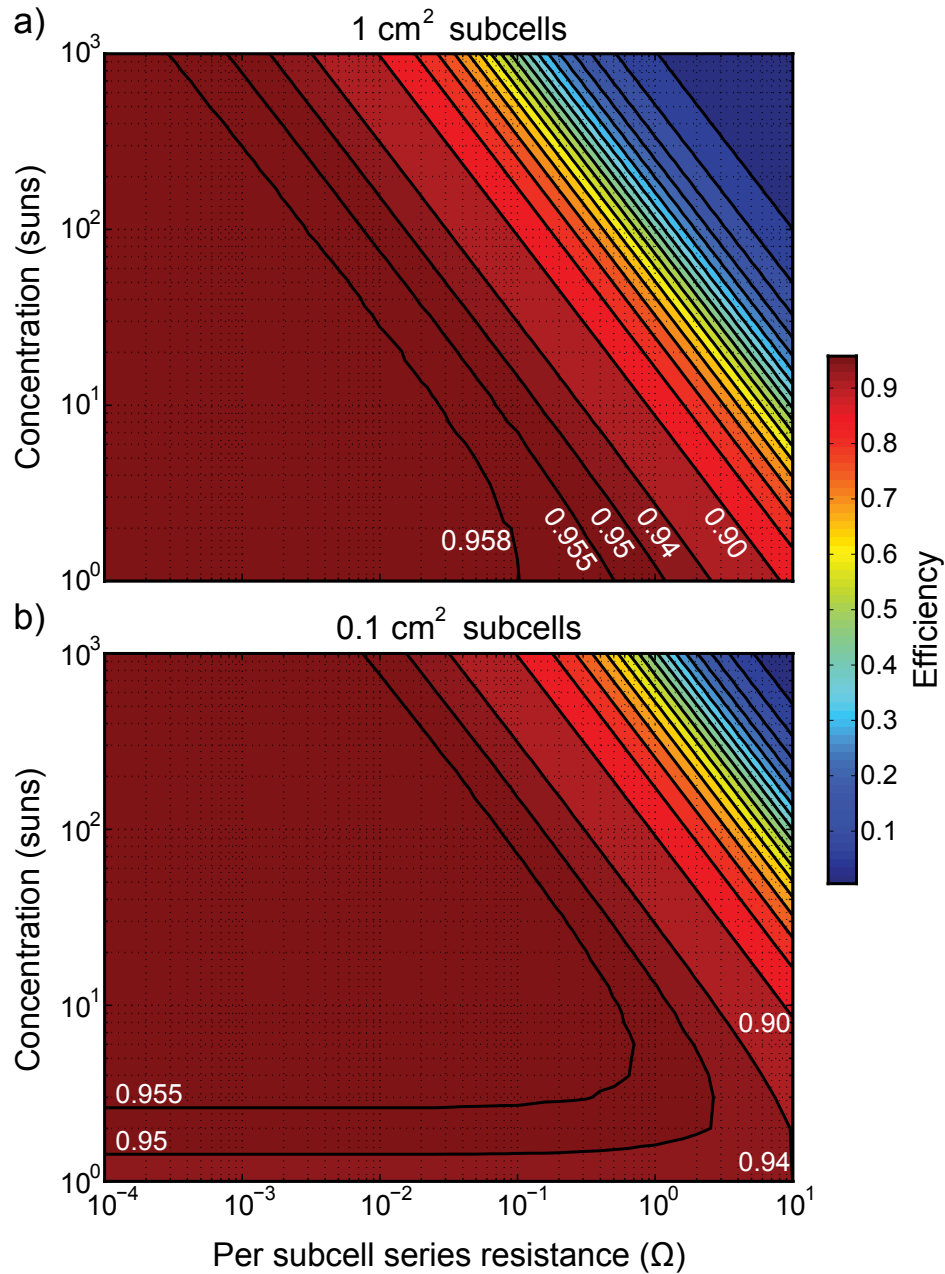


Figure 6.4: Module circuit efficiency versus concentration and lumped series resistance. Reprinted with permission from the copyright holder, ©2014 IEEE.

Concentration is allowed to freely vary, under the assumption that a microinverter can be designed with equal efficiency and input voltage to the model used previously while the microinverter input power scales linearly with the concentration consid-

ered. This permits use of a fixed circuit topology for subcells of constant size and deconvolutes subcell size effects from concentration effects.

Increasing concentration yields a slight increase in modeled subcell efficiency, while Joule-Thompson resistive losses ( $P = I^2R$ ) increase with the square of the current. The net result is a lower maximum tolerable series resistance to achieve a particular efficiency at higher concentrations. This trend is readily visualized by considering a vertical cross-section through either subplot of Fig. 6.4. In contrast, decreasing cell size from  $1 \text{ cm}^2$  (Fig. 6.4a) to  $0.1 \text{ cm}^2$  (Fig. 6.4b) offers significant advantage in the resistance design tolerance at the expense of a greater number of components. Because the subcell string voltage is fixed, the subcircuits must adopt an increased number of parallel strings in order to keep the power supplied to the power conditioning electronics at a given concentration identical to the case of Fig. 6.4a. This leads to a parallelization of resistances that enables approximately a 1:1 increase in tolerable resistance per relative decrease in cell area. The bypass diode leakage current becomes more important as cell size decreases, resulting in the drop-off in efficiency seen at low concentrations in Fig. 6.4b.

#### 6.4 Conclusions

We have described and simulated a specific circuit design capable of realizing independent electrical connection with two-terminal output for a lateral multijunction photovoltaic module. A point design capable of 87.5% circuit efficiency was described in detail, and a clear pathway to higher circuit efficiency exists through reduction in subcell area, more generalized contact geometry optimization, and development of power electronics tailored to the output voltage and power characteristics of the spectrum splitting module.

This is an enabling component of a complete spectrum-splitting photovoltaic system. Electrical independence, and a means of capturing generated power sans current-matching, effectively raises the capacity factor of the photovoltaic module. This makes the spectrum splitting module a more attractive investment, and eliminates some of the possibility for confusion between concentrating and flat plate photovoltaic technologies by normalizing the power production basis on which they previously have been erroneously compared. Finally, realizing the energy production gains from independent electrical connection is key to materializing a competitive cost (LCOE) advantage relative to more conventional monolithic concentrator geometries.

*Chapter 7*

## CONCLUSIONS

Throughout this thesis we have presented an array of research all centered around enabling technologies for achieving increased efficiency and energy yield in photovoltaic conversion of sunlight. Efficiency is a key driver for reducing the levelized cost of electricity, the pricing basis to which all electricity generating technologies are ultimately responsible. We developed modeling tools capable of providing new design space to the broader photovoltaics field, developed specific photovoltaic converter designs capable of unprecedented ( $>50\%$ ) submodule and module efficiencies, prototyped and characterized the first (to our knowledge) photovoltaic converter with seven unique bandgaps, and developed power combination topologies that are broadly enabling for independent electrical connection and spectrum-insensitive power conversion. We hope these capabilities and proof-of-concept will aid and inspire future researchers in the field to achieve still elusive ultrahigh module efficiency.

In Chapter 2 we developed a three-dimensional distributed equivalent circuit model for a solar cell. This allowed us to replicate precisely its optoelectronic response, accounting for position-dependent effects, such as junction bias, sidewall recombination, and current spreading. The improved accuracy of the model over 1D and 2D circuit models was uniquely enabling for contact optimization. We developed the capability to further refine the modified detailed balance calculation to account for realistic resistive losses within photovoltaics. We optimized time-tested inverted square contact geometries to design contacts for prototype spectrum-splitting submodules and proved out the efficacy of the designs experimentally; resistive loss did not limit the prototype PSR submodule efficiency. Finally, we began to explore blue ocean design space by combining the distributed circuit model with a genetic algorithm. Further algorithmic refinement could yield highly performing results that defy intuition.

The distributed circuit model was contextualized by integrating it with modified detailed balance, ray tracing, and lumped circuit electrical models to wholistically model and design the polyhedral specular reflector in Chapter 3. We presented the function of each of the modeling tools, and then optimized contacts for and

analyzed an array of point designs covering the design space. We predicted the power output from spectrum-splitting submodules and identified cases with the potential for ultrahigh (<50%) efficiency, including resistive losses. Guidelines were proposed for future opportunity in the concentrator photovoltaic contact design space based on what was learned in the design study.

We then developed a specific point design in Chapter 4 that was feasible to fabricate with high efficiency. The procedure to integrate such a device was presented before we described its characterization in Chapter 5. We designed optical tools to precisely characterize the broadband and split-spectrum performance of each of the constituent components and the integrated prototype polyhedral specular reflector submodule. The optical performance was exemplary; the integrated optical efficiency (84.5%) was 94% of the design value (89.9%). The prototype was characterized at 30.2% submodule efficiency, which while short of an efficiency record is still a respectable performance. The primary cause of the discrepancy between the designed and measured efficiency was the subcell performance, which presents clear steps for further improvement. Implementation of optimized contacts with smaller feature sizes on subcells with thicker absorbers will provide a substantial boost to the current. Redesign for and operation under higher concentration (~500×) will reduce the relative contribution of sidewall recombination, and will even further amplify the temperature operation advantages of lateral spectrum-splitting. Finally, incorporating high reflectivity back reflectors on patterned rear contact layers will enable improved photon recycling and radiative emission, driving up cell voltages. Even without such back mirrors, we expect submodules >40% efficiency to be achievable.

Finally, Chapter 6 developed a circuit topology, point design, and extensibility mechanism for independent electrical connection to multijunction subcells. We employed off-the-shelf power conditioning equipment to decouple independent inputs comprised of series-parallel strings at a single bandgap from voltage-synchronized outputs that can be combined in parallel to deliver power to the grid. This module circuit architecture is an enabling technology for multijunction photovoltaics with at least two independent subcells to realize the annual energy yield gains possible with independent electrical connection.

It is my hope that this work instills optimism for the prospects of very high and ultrahigh efficiency photovoltaic modules. I aspire for my children to live in a future in which electricity is both inexpensive and free of negative externalities. The

energy generating technology enabling that future, like each that has come before, must make efficient use of the giant fusion reactor a mere 8.3 minute commute away (for photons).

## BIBLIOGRAPHY

- [1] U.S. Energy Information Administration. (2016). International energy outlook 2016, [Online]. Available: [www.eia.gov/forecasts/ieo/pdf/0484\(2016\).pdf](http://www.eia.gov/forecasts/ieo/pdf/0484(2016).pdf) (visited on 12/22/2016).
- [2] P. Würfel and U. Würfel, *Physics of solar cells: From basic principles to advanced concepts*. John Wiley & Sons, 2009.
- [3] R. Perez and M. Perez, “A fundamental look at energy reserves for the planet,” *The IEA SHC Solar Update*, vol. 50, no. 2, 2009.
- [4] U.S. Energy Information Administration. (2016). What is u.s. electricity generation by energy source? [Online]. Available: <https://www.eia.gov/tools/faqs/faq.cfm?id=427&t=3> (visited on 12/22/2016).
- [5] U.S. Energy Information Administration. (2016). Electric power annual 2015, [Online]. Available: <http://www.eia.gov/electricity/annual/pdf/epa.pdf> (visited on 12/22/2016).
- [6] U.S. Energy Information Administration. (2016). Electric power monthly with data for september 2016, [Online]. Available: <http://www.eia.gov/electricity/monthly/pdf/epm.pdf> (visited on 12/22/2016).
- [7] California Independent Systems Operator. (2016). 2015 annual report on market issues & performance, [Online]. Available: <http://www.caiso.com/Documents/2015AnnualReportonMarketIssuesandPerformance.pdf> (visited on 12/22/2016).
- [8] V. Sivaram and S. Kann, “Solar power needs a more ambitious cost target,” *Nature Energy*, vol. 1, p. 16036, 2016.
- [9] U.S. Energy Information Administration. (2016). Levelized cost and levelized avoided cost of new generation resources in the annual energy outlook 2016, [Online]. Available: [http://www.eia.gov/outlooks/aeo/pdf/electricity\\_generation.pdf](http://www.eia.gov/outlooks/aeo/pdf/electricity_generation.pdf) (visited on 12/22/2016).
- [10] M. Woodhouse, R. Jones-Albertus, D. Feldman, R. Fu, K. Horowitz, D. Chung, D. Jordan, and S. Kurtz, “On the path to sunshot: The role of advancements in solar photovoltaic efficiency, reliability, and costs,” National Renewable Energy Laboratory (NREL), Golden, CO, Tech. Rep., 2016, NREL/TP-6A20-65872. [Online]. Available: <http://www.nrel.gov/docs/fy16osti/65872.pdf>.
- [11] W. Shockley and H. J. Queisser, “Detailed balance limit of efficiency of p-n junction solar cells,” *Journal of Applied Physics*, vol. 32, no. 3, pp. 510–519, 1961.

- [12] M. A. Green, K. Emery, Y. Hishikawa, W. Warta, and E. D. Dunlop, "Solar cell efficiency tables (version 40)," *Progress in Photovoltaics: Research and Applications*, vol. 20, no. 5, pp. 606–614, 2012, ISSN: 1099-159X. DOI: 10.1002/pip.2267. [Online]. Available: <http://dx.doi.org/10.1002/pip.2267>.
- [13] M. A. Green, "Radiative efficiency of state-of-the-art photovoltaic cells," *Progress in Photovoltaics: Research and Applications*, vol. 20, no. 4, pp. 472–476, 2012. DOI: 10.1002/pip.1147.
- [14] A. Polman and H. A. Atwater, "Photonic design principles for ultrahigh-efficiency photovoltaics," *Nature Materials*, vol. 11, no. 3, pp. 174–177, 2012. DOI: 10.1038/nmat3263.
- [15] F. Dimroth, T. N. Tibbits, M. Niemeier, F. Predan, P. Beutel, C. Karcher, E. Oliva, G. Siefert, D. Lackner, P. Fuß-Kailuweit, *et al.*, "Four-junction wafer-bonded concentrator solar cells," *IEEE Journal of Photovoltaics*, vol. 6, no. 1, pp. 343–349, 2016.
- [16] E. C. Warmann and H. A. Atwater, "Energy production advantage of independent subcell connection for multijunction photovoltaics," *Energy Science & Engineering*, vol. 4, no. 4, pp. 235–244, 2016.
- [17] E. Torrey, P. Ruden, and P. Cohen, "Performance of a split-spectrum photovoltaic device operating under time-varying spectral conditions," *Journal of Applied Physics*, vol. 109, no. 7, p. 074 909, 2011.
- [18] J. Geisz, D. Friedman, J. Ward, A. Duda, W. Olavarria, T. Moriarty, J. Kiehl, M. Romero, A. Norman, and K. Jones, "40.8% efficient inverted triple-junction solar cell with two independently metamorphic junctions," *Applied Physics Letters*, vol. 93, no. 12, p. 123 505, 2008.
- [19] R. M. France, J. F. Geisz, I. García, M. A. Steiner, W. E. McMahon, D. J. Friedman, T. E. Moriarty, C. Osterwald, J. S. Ward, A. Duda, *et al.*, "Design flexibility of ultrahigh efficiency four-junction inverted metamorphic solar cells," *IEEE Journal of Photovoltaics*, vol. 6, no. 2, pp. 578–583, 2016.
- [20] A. Imenes and D. Mills, "Spectral beam splitting technology for increased conversion efficiency in solar concentrating systems: A review," *Solar Energy Materials and Solar Cells*, vol. 84, no. 1, pp. 19–69, 2004. DOI: 10.1016/j.solmat.2004.01.038.
- [21] A. Mojiri, R. Taylor, E. Thomsen, and G. Rosengarten, "Spectral beam splitting for efficient conversion of solar energy—a review," *Renewable and Sustainable Energy Reviews*, vol. 28, pp. 654–663, 2013. DOI: <http://dx.doi.org/10.1016/j.rser.2013.08.026>.
- [22] M. A. Green, M. J. Keevers, I. Thomas, J. B. Lasich, K. Emery, and R. R. King, "40% efficient sunlight to electricity conversion," *Progress in Photovoltaics: Research and Applications*, vol. 23, no. 6, pp. 685–691, 2015.

- [23] J. D. McCambridge, M. A. Steiner, B. L. Unger, K. A. Emery, E. L. Christensen, M. W. Wanlass, A. L. Gray, L. Takacs, R. Buelow, T. A. McCollum, J. W. Ashmead, G. R. Schmidt, A. W. Haas, J. R. Wilcox, J. Van Meter, J. L. Gray, D. T. Moore, A. M. Barnett, and R. J. Schwartz, "Compact spectrum splitting photovoltaic module with high efficiency," *Progress in Photovoltaics: Research and Applications*, vol. 19, no. 3, pp. 352–360, 2011, ISSN: 1099-159X. DOI: 10.1002/pip.1030. [Online]. Available: <http://dx.doi.org/10.1002/pip.1030>.
- [24] M. Steiner, A. Bösch, A. Dilger, F. Dimroth, T. Dörsam, M. Müller, T. Hornung, G. Siefert, M. Wiesenfarth, and A. W. Bett, "Flatcon® cpv module with 36.7% efficiency equipped with four-junction solar cells," *Progress in Photovoltaics: Research and Applications*, vol. 23, no. 10, pp. 1323–1329, 2015.
- [25] M. A. Green, K. Emery, Y. Hishikawa, W. Warta, E. D. Dunlop, D. H. Levi, and A. W. Ho-Baillie, "Solar cell efficiency tables (version 49)," *Progress in Photovoltaics: Research and Applications*, 2016.
- [26] O. D. Miller, E. Yablonovitch, and S. R. Kurtz, "Strong internal and external luminescence as solar cells approach the Shockley–Queisser limit," *IEEE Journal of Photovoltaics*, vol. 2, no. 3, pp. 303–311, 2012.
- [27] A. Moore, "Optimized grid design for a sun-concentrator solar cell," *RCA Rev.:(United States)*, vol. 40, no. 2, pp. 140–152, 1979.
- [28] B. Galiana, C. Algora, I. Rey-Stolle, and I. G. Vara, "A 3-d model for concentrator solar cells based on distributed circuit units," *IEEE Transactions on Electron Devices*, vol. 52, no. 12, pp. 2552–2558, 2005.
- [29] B. Galiana, C. Algora, and I. Rey-Stolle, "Comparison of 1d and 3d analysis of the front contact influence on gaas concentrator solar cell performance," *Solar Energy Materials and Solar Cells*, vol. 90, no. 16, pp. 2589–2604, 2006.
- [30] I. Garcia, I. Rey-Stolle, B. Galiana, and C. Algora, "A 32.6% efficient lattice-matched dual-junction solar cell working at 1000 suns," *Applied Physics Letters*, vol. 94, no. 5, p. 053 509, 2009. DOI: [doi:http://dx.doi.org/10.1063/1.3078817](http://dx.doi.org/10.1063/1.3078817).
- [31] I. García Vara, P. Espinet González, I. Rey-Stolle Prado, E. Barrigón Montañés, and C. Algora del Valle, "Extended triple-junction solar cell 3d distributed model: Application to chromatic aberration-related losses," 2011.
- [32] Synopsys, Inc., *Synopsys HSPICE - accurate circuit simulation*, 2016. [Online]. Available: <https://www.synopsys.com/tools/Verification/AMSVeification/CircuitSimulation/HSPICE/Pages/default.aspx>.

- [33] E. C. Warmann, C. A. Flowers, J. Lloyd, C. N. Eisler, M. D. Escarra, and H. A. Atwater, "Energy production advantage of independent subcell connection for multijunction photovoltaics," *Energy Science & Engineering*, submitted,
- [34] M. Steiner, S. P. Philipps, M. Hermle, A. W. Bett, and F. Dimroth, "Validated front contact grid simulation for gaas solar cells under concentrated sunlight," *Progress in Photovoltaics: Research and Applications*, vol. 19, no. 1, pp. 73–83, 2011. DOI: [10.1002/pip.989](https://doi.org/10.1002/pip.989).
- [35] A. Antonini, M. Stefancich, D. Vincenzi, C. Malagu, F. Bizzi, A. Ronzoni, and G. Martinelli, "Contact grid optimization methodology for front contact concentration solar cells," *Solar Energy Materials and Solar Cells*, vol. 80, no. 2, pp. 155–166, 2003. DOI: <http://dx.doi.org/10.1016/j.solmat.2003.07.001>.
- [36] J. S. Ward, A. Duda, D. J. Friedman, J. Geisz, W. McMahon, and M. Young, "High aspect ratio electrodeposited Ni/Au contacts for GaAs-based III–V concentrator solar cells," *Progress in Photovoltaics: Research and Applications*, vol. 23, no. 5, pp. 646–653, 2015. DOI: [10.1002/pip.2490](https://doi.org/10.1002/pip.2490).
- [37] A. del Campo and C. Greiner, "SU-8: A photoresist for high-aspect-ratio and 3D submicron lithography," *Journal of Micromechanics and Microengineering*, vol. 17, no. 6, R81, 2007.
- [38] F. Djeflal, T. Bendib, D. Arar, and Z. Dibi, "An optimized metal grid design to improve the solar cell performance under solar concentration using multi-objective computation," *Materials Science and Engineering: B*, vol. 178, no. 9, pp. 574–579, 2013.
- [39] F. Afshinmanesh, A. G. Curto, K. M. Milaninia, N. F. van Hulst, and M. L. Brongersma, "Transparent metallic fractal electrodes for semiconductor devices," *Nano letters*, vol. 14, no. 9, pp. 5068–5074, 2014.
- [40] L. Davis, *Handbook of genetic algorithms*. Van Nostrand Reinhold, 1991.
- [41] E. C. Warmann, *Design strategies for ultra-high efficiency photovoltaics*. 2014.
- [42] C. N. Eisler, C. A. Flowers, E. C. Warmann, J. Lloyd, P. Espinet-Gonzalez, S. Darbe, M. Dee, M. Escarra, E. D. Kosten, W. Zhou, and H. A. Atwater, "The polyhedral specular reflector: A spectrum-splitting multijunction design to achieve ultrahigh (>50%) solar module efficiency," *In preparation*, 2016,
- [43] C. N. Eisler, "Supplemental placeholder," *In preparation*, 2016.
- [44] C. H. Henry, "Limiting efficiencies of ideal single and multiple energy gap terrestrial solar cells," *Journal of Applied Physics*, vol. 51, no. 8, pp. 4494–4500, 1980.

- [45] J. F. Geisz, M. A. Steiner, I. Garcia, S. R. Kurtz, and D. J. Friedman, “Enhanced external radiative efficiency for 20.8% efficient single-junction gainp solar cells,” *Applied Physics Letters*, vol. 103, no. 4, p. 041118, 2013. doi: <http://dx.doi.org/10.1063/1.4816837>.
- [46] B. M. Kayes, H. Nie, R. Twist, S. G. Spruytte, F. Reinhardt, I. C. Kizilyalli, and G. S. Higashi, “27.6% conversion efficiency, a new record for single-junction solar cells under 1 sun illumination,” in *Photovoltaic Specialists Conference (PVSC), 2011 37th IEEE*, IEEE, 2011, pp. 000004–000008. doi: [10.1109/pvsc.2011.6185831](https://doi.org/10.1109/pvsc.2011.6185831).
- [47] P. Kidd, D. Dunstan, H. Colson, M. Louren, A. Sacedo, F. Gonza, L. Gonza, Y. Gonza, R. Garci, D. Gonza, *et al.*, “Comparison of the crystalline quality of step-graded and continuously graded ingaas buffer layers,” *Journal of crystal growth*, vol. 169, no. 4, pp. 649–659, 1996.
- [48] R. Varache, C. Leendertz, M. Gueunier-Farret, J. Haschke, D. Muñoz, and L. Korte, “Investigation of selective junctions using a newly developed tunnel current model for solar cell applications,” *Solar Energy Materials and Solar Cells*, vol. 141, pp. 14–23, 2015.
- [49] R. Ahrenkiel, R. Ellingson, S. Johnston, J. Webb, J. Carapella, and M. W anl ass, “Recombination lifetime of  $\text{In}_x\text{Ga}_{1-x}\text{As}$  alloys used in thermophotovoltaic converters,” in *AIP Conference Proceedings*, vol. 460, 1999.
- [50] I. Vurgaftman, J. Meyer, and L. Ram-Mohan, “Band parameters for iii–v compound semiconductors and their alloys,” *Journal of applied physics*, vol. 89, no. 11, pp. 5815–5875, 2001.
- [51] M. Law, L. E. Greene, J. C. Johnson, R. Saykally, and P. Yang, “Nanowire dye-sensitized solar cells,” *Nature materials*, vol. 4, no. 6, pp. 455–459, 2005.
- [52] B. Sermage, J. Benchimol, and G. Cohen, “Carrier lifetime in p-doped ingaas and ingaasp,” in *Indium Phosphide and Related Materials, 1998 International Conference on*, IEEE, 1998, pp. 758–760.
- [53] C. N. Eisler, E. D. Kosten, E. C. Warmann, and H. A. Atwater, “Spectrum splitting photovoltaics: Polyhedral specular reflector design for ultra-high efficiency modules,” in *2013 IEEE 39th Photovoltaic Specialists Conference (PVSC)*, IEEE, 2013, pp. 1848–1851.
- [54] M. D. Escarra, S. Darbe, E. C. Warmann, and H. A. Atwater, “Spectrum-splitting photovoltaics: Holographic spectrum splitting in eight-junction, ultra-high efficiency module,” in *2013 IEEE 39th Photovoltaic Specialists Conference (PVSC)*, IEEE, 2013, pp. 1852–1855.
- [55] E. D. Kosten, J. Lloyd, E. Warmann, and H. A. Atwater, “Spectrum splitting photovoltaics: Light trapping filtered concentrator for ultrahigh photovoltaic efficiency,” in *2013 IEEE 39th Photovoltaic Specialists Conference (PVSC)*, IEEE, 2013, pp. 3053–3057.

- [56] C. N. Eisler, E. C. Warmann, C. A. Flowers, M. Dee, E. D. Kosten, and H. A. Atwater, "Design improvements for the polyhedral specular reflector spectrum-splitting module for ultra-high efficiency (> 50%)," in *2014 IEEE 40th Photovoltaic Specialist Conference (PVSC)*, IEEE, 2014, pp. 2224–2229.
- [57] R. J. Linderman, Z. S. Judkins, M. Shoecraft, and M. J. Dawson, "Thermal performance of the SunPower Alpha-2 PV concentrator," *IEEE Journal of Photovoltaics*, vol. 2, no. 2, pp. 196–201, 2012. DOI: 10.1109/jphotov.2011.2178397.
- [58] S. Larouche and L. Martinu, "Openfilters: Open-source software for the design, optimization, and synthesis of optical filters," *Applied Optics*, vol. 47, no. 13, pp. C219–C230, 2008. DOI: 10.1364/ao.47.00c219.
- [59] C. N. Eisler, C. A. Flowers, P. Espinet, S. Darbe, E. C. Warmann, J. Lloyd, M. Dee, and H. A. Atwater, "Designing and prototyping the polyhedral specular reflector, a spectrum-splitting module with projected >50% efficiency," in *Photovoltaic Specialist Conference (PVSC), 2015 IEEE 42nd*, IEEE, 2015, pp. 1–5. DOI: 10.1109/pvsc.2015.7356406.
- [60] W. T. Welford and R. Winston, *High collection nonimaging optics*. Elsevier, 2012.
- [61] C. N. Eisler, "Photonic and device design principles for ultrahigh-efficiency (> 50%), spectrum-splitting photovoltaics," PhD thesis, California Institute of Technology, 2016.
- [62] C. A. Flowers, C. N. Eisler, and H. A. Atwater, "Electrically independent sub-circuits for a seven-junction spectrum splitting photovoltaic module," in *2014 IEEE 40th Photovoltaic Specialist Conference (PVSC)*, Jun. 2014, pp. 1339–1343. DOI: 10.1109/PVSC.2014.6925165.
- [63] B. Furman, E. Menard, A. Gray, M. Meitl, S. Bonafede, D. Kneeburg, K. Ghosal, R. Bukovnik, W. Wagner, J. Gabriel, *et al.*, "A high concentration photovoltaic module utilizing micro-transfer printing and surface mount technology," in *Photovoltaic Specialists Conference (PVSC), 2010 35th IEEE*, IEEE, 2010, pp. 000475–000480. DOI: 10.1109/PVSC.2010.5616766.
- [64] D. C. Giancoli, *Physics for scientists and engineers with modern physics*, 4th. Upper Saddle River, New Jersey: Prentice Hall, 2009, ch. 25.
- [65] P. V. Bolotoff, *Solder alloys: Physical and mechanical properties*, 2010. [Online]. Available: [http://alasilir.com/reference/solder\\_alloys/](http://alasilir.com/reference/solder_alloys/).
- [66] SolarEdge, *Power optimizer specifications - p600 / p700*, 2015. [Online]. Available: <http://www.solaredge.com/files/pdfs/products/power-optimizers/p-series-commercial-us-application-note.pdf>.

- [67] T. J. Silverman, M. G. Deceglie, B. Marion, S. Cowley, B. Kayes, and S. Kurtz, "Outdoor performance of a thin-film gallium-arsenide photovoltaic module," in *2013 IEEE 39th Photovoltaic Specialists Conference (PVSC)*, IEEE, 2013, pp. 0103–0108.
- [68] R. B. Bird, W. E. Stewart, and E. N. Lightfoot, *Transport Phenomena, Revised 2nd Edition*, 2nd. John Wiley & Sons, Inc., Dec. 2006, ISBN: 0470115394.
- [69] M. Muller, T. J. Silverman, M. Deceglie, S. Kurtz, E. Menard, and S. Burroughs, "Optical cell temperature measurements of multiple CPV technologies in outdoor conditions," in *2013 IEEE 39th Photovoltaic Specialists Conference (PVSC)*, IEEE, 2013, pp. 3426–3430. DOI: 10.1109/PVSC.2013.6745184.
- [70] R. Winston, J. C. Miñano, P. G. Benitez, *et al.*, *Nonimaging optics*. Academic Press, 2005.
- [71] A. Nayak, G. S. Kinsey, M. Liu, W. Bagienski, and V. Garboushian, "Comparison of primary optics in amonix CPV arrays," in *8th International Conference on Concentrating Photovoltaic Systems: CPV-8*, AIP Publishing, vol. 1477, 2012, pp. 77–80. DOI: 10.1063/1.4753838.
- [72] S. Burroughs, R. Conner, B. Furman, E. Menard, A. Gray, M. Meitl, S. Bonafede, D. Kneeburg, K. Ghosal, R. Bukovnik, *et al.*, "A new approach for a low cost CPV module design utilizing micro-transfer printing technology," in *AIP Conference Proceedings*, vol. 1277, 2010, p. 163.
- [73] R. King, D. Bhusari, A. Boca, D. Larrabee, X.-Q. Liu, W. Hong, C. Fetzer, D. Law, and N. Karam, "Band gap-voltage offset and energy production in next-generation multijunction solar cells," *Progress in Photovoltaics: Research and Applications*, vol. 19, no. 7, pp. 797–812, 2011.
- [74] M. A. Green, K. Emery, Y. Hishikawa, W. Warta, and E. D. Dunlop, "Solar cell efficiency tables (version 47)," *Progress in Photovoltaics: Research and Applications*, vol. 24, no. NREL/JA-5J00-65643, 2016. DOI: 10.1002/pip.2728.
- [75] U. B. Schallenberg, "Antireflection design concepts with equivalent layers," *Applied Optics*, vol. 45, no. 7, pp. 1507–1514, 2006.
- [76] M. P. Lumb, M. Meitl, K. J. Schmieder, M. Gonzalez, S. Mack, M. K. Yakes, M. F. Bennett, J. Frantz, M. A. Steiner, J. F. Geisz, *et al.*, "Towards the ultimate multi-junction solar cell using transfer printing," in *Photovoltaic Specialists Conference (PVSC), 2016 IEEE 43rd*, IEEE, 2016, pp. 0040–0045.
- [77] A. Barnett, D. Kirkpatrick, C. Honsberg, D. Moore, M. Wanlass, K. Emery, R. Schwartz, D. Carlson, S. Bowden, D. Aiken, *et al.*, "Very high efficiency solar cell modules," *Progress in Photovoltaics: Research and Applications*, vol. 17, no. 1, pp. 75–83, 2009.

- [78] L. Z. Broderick, B. R. Albert, B. S. Pearson, L. C. Kimerling, and J. Michel, "Solar spectral variations and their influence on concentrator solar cell performance," in *SPIE Solar Energy + Technology*, International Society for Optics and Photonics, 2013, pp. 88210I–88210I.
- [79] E. C. Warmann, C. Eisler, E. Kosten, M. Escarra, and H. A. Atwater, "Spectrum splitting photovoltaics: Materials and device parameters to achieve ultrahigh system efficiency," in *2013 IEEE 39th Photovoltaic Specialists Conference (PVSC)*, Jun. 2013, pp. 1922–1925. DOI: 10.1109/PVSC.2013.6744845.
- [80] H. Cotal, C. Fetzer, J. Boisvert, G. Kinsey, R. King, P. Herbert, H. Yoon, and N. Karam, "III–V multijunction solar cells for concentrating photovoltaics," *Energy & Environmental Science*, vol. 2, no. 2, pp. 174–192, 2009.
- [81] M. Wolf, "Limitations and possibilities for improvement of photovoltaic solar energy converters: Part i: Considerations for earth's surface operation," *Proceedings of the IRE*, vol. 48, no. 7, pp. 1246–1263, 1960.
- [82] W. Blocker, "High-efficiency solar energy conversion through flux concentration and spectrum splitting," *Proceedings of the IEEE*, vol. 66, no. 1, pp. 104–105, 1978.
- [83] J. M. Russo, D. Zhang, M. Gordon, S. D. Vorndran, Y. Wu, and R. K. Kostuk, "Grating-over-lens concentrating photovoltaic spectrum splitting systems with volume holographic optical elements," in *SPIE Solar Energy+ Technology*, International Society for Optics and Photonics, 2013, pp. 882 106–882 106.
- [84] A. Vlasov, V. Khvostikov, L. Karlina, S. Sorokina, N. Potapovich, M. Shvarts, N. K. Timoshina, V. Lantratov, S. Mintairov, N. Kalyuzhnyi, *et al.*, "Spectral-splitting concentrator photovoltaic modules based on algaas/gaas/gasb and gainp/ingaas (p) solar cells," *Technical Physics*, vol. 58, no. 7, pp. 1034–1038, 2013.
- [85] P. Wang, J. A. Dominguez-Caballero, D. J. Friedman, and R. Menon, "A new class of multi-bandgap high-efficiency photovoltaics enabled by broadband diffractive optics," *Progress in Photovoltaics: Research and Applications*, vol. 23, no. 9, pp. 1073–1079, 2015.

*Appendix A***POSITIONAL IRRADIANCE MEASUREMENT:  
CHARACTERIZATION OF SPECTRUM-SPLITTING AND  
CONCENTRATING OPTICS FOR PHOTOVOLTAICS**

C. A. Flowers, S. Darbe, C. N. Eisler, J. He, and H. A. Atwater, "Positional irradiance measurement: Characterization of spectrum-splitting and concentrating optics for photovoltaics," in *High and Low Concentrator Systems for Solar Energy Applications IX*, A. P. Plesniak and C. Pfefferkorn, Eds., Proceedings of SPIE, vol. 9175, Bellingham, WA: SPIE, 2014, 91750F-1–91750F-9. DOI: 10.1117/12.2062245,

©2014 SPIE

**Abstract**

Multijunction photovoltaics enable significantly improved efficiency over their single junction analogues by mitigating unabsorbed sub-bandgap photons and voltage loss to carrier thermalization. Lateral spectrum-splitting configurations promise further increased efficiency through relaxation of the lattice- and current-matching requirements of monolithic stacks, albeit at the cost of increased optical and electrical complexity. Consequently, in order to achieve an effective spectrum-splitting photovoltaic configuration it is essential that all optical losses and photon misallocation be characterized and subsequently minimized.

We have developed a characterization system that enables us to map the spatial, spectral, and angular distribution of illumination incident on the subcell reception plane or emerging from any subset of the concentrating and splitting optics. This positional irradiance measurement system (PIMS) comprises four motorized stages assembled in an  $x$ - $z$ - $r$ - $y$  configuration with three linear degrees of freedom and one rotational degree of freedom, on which we mount an optical fiber connected to a set of spectrometers covering the solar spectrum from 280-1700 nm. In combination with a xenon arc lamp solar simulator with a divergence half angle of 1.3 degrees, we are able to characterize our optics across the full spectrum of our photovoltaic subcells with close agreement to outdoor conditions. We have used this tool to spectrally characterize holographic diffraction efficiency versus diffraction angle; multilayer dielectric filter transmission and reflection efficiency versus filter

incidence angle; and aspheric lens chromatic aberration versus optic-to-receiver separation distance. These examples illustrate the versatility of the PIMS in characterizing optical performance relevant to both spectrum-splitting and traditional multijunction photovoltaics.

## **A.1 Introduction**

Lateral spectrum splitting photovoltaics offer potential for unprecedented sunlight-to-electricity conversion efficiency [14], [81], [82]. This is enabled by the facile pathway to a larger number of junctions [44], the wider material selection with reduced lattice matching constraints relative to monolithic multijunction photovoltaics, and improved response to spectral variability with independent electrical connection to each of the subcells [17]. Despite these advantages, no spectrum-splitting embodiment to date has surpassed the record efficiency of monolithic multijunction devices. Recent interest in spectrum splitting has focused on novel optical design methods and configurations to enable improved form factors and increased efficiency [77], [83]–[85].

Fundamentally, spectrum splitting optics require precise characterization of the laterally dispersed illumination incident on each subcell, as well as any stray light lost to passive elements within the photovoltaic system. We have developed an optical characterization system that enables us to map the spatial, spectral, and angular distribution of illumination incident on an optical reception plane. The tool combines four motorized stages for three-dimensional and rotational positioning control with a fiber optic-coupled spectrometer spanning 280-1700 nm. Proof of concept has been demonstrated by using the positional irradiance measurement system (PIMS) to characterize diverse spectrum splitting and concentrating optical elements: a transmission hologram, two bandpass dichroic filters, and a concentrating aspheric lens with chromatic aberration. Hologram measurements demonstrate goniospectral characterization with varying transmission as a function of diffraction angle, dichroic filter measurements demonstrate spectral characterization with varying transmission as a function of incidence angle, and aspheric lens measurements demonstrate one dimension of spatial-spectral characterization.

## **A.2 Experimental**

### **Positional irradiance measurement system**

The PIMS is shown in Fig. A.1, and is designed to perform spatial-spectral mapping [85] on a reception plane with incident angle resolution, producing a spatially

resolved goniospectral map. The system consists of three linear and one rotational stages stacked in an  $x$ - $z$ - $r$ - $y$  configuration, where the  $z$ -axis is the axis of optical propagation. The end of an optical fiber is mounted to the  $y$ -stage in order to be rastered in two dimensions to map the optical reception plane. Angular resolution is gained by placing an aperture at the front of the optical fiber at the eucentric point to restrict the angular acceptance range and acquiring a spatial-spectral map at several angles of incidence by rotating the entire optical assembly about its  $y$ -axis. The optical fiber is trifurcated and transmitted light impinges onto three spectrometer pixel arrays to cover the spectral range of interest for spectrum splitting solar energy conversion (280-1700 nm).

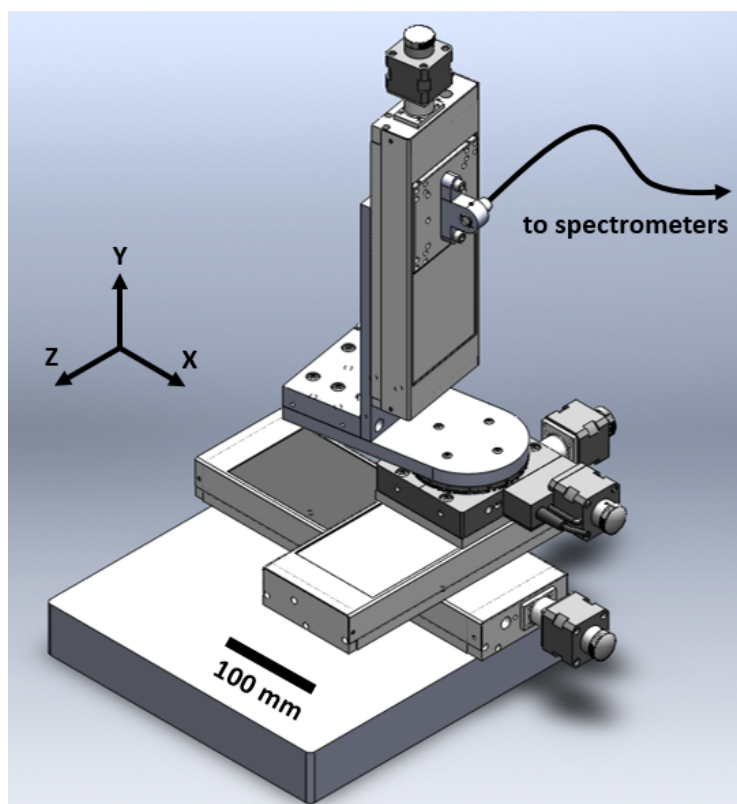


Figure A.1: Positional irradiance measurement system solid model.

Each of these capabilities is critical to properly predicting the system efficiency for a spectrum splitting photovoltaic device. The spectral response of a solar cell depends both on wavelength and angle of incidence, and an optimal anti-reflection (AR) coating will account for spectral and angular distribution. Beyond subcell illumination, validating spectrum splitting performance of the optical system requires knowledge of the input spectra to all optical elements arranged in parallel. Additionally, a thermodynamically optimal optical system will match the etendue

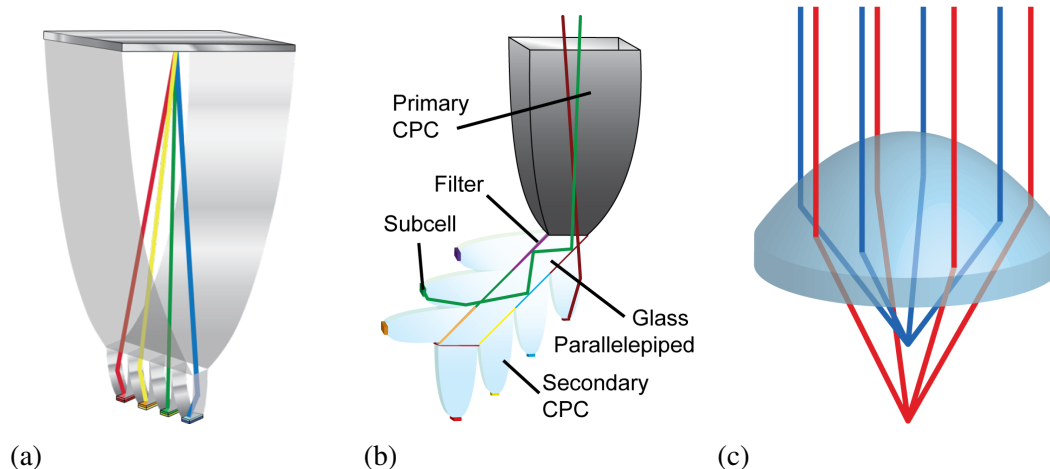


Figure A.2: Schematics of various spectrum splitting submodule optics characterized by PIMS.

between optical components connected in series. Characterizing the angular and spatial extent of the output of each optic in the system is necessary to properly design each subsequent optical element. This information also enables accounting for discrepancies between the performance of ideal components and as-fabricated components for subsequent design iterations.

### A.3 Results and discussion

#### Transmission hologram

The PIMS was used to characterize the diffractive properties of a transmission hologram designed to perform spectrum splitting in the configuration pictured in Fig. A.2a. In this design, stacked sets of holograms diffract normally incident illumination into frequency bands directed onto underlying subcells. Concentration is performed after spectrum splitting as the holograms exhibit relatively low tolerance to incident angular spread. Subcell bandgaps are each optimized for conversion of the resulting incident spectrum.

The experimentally characterized hologram was purchased off-the-shelf from Wasatch Photonics, and an in-house analytical model was used to predict the diffraction efficiency across the solar spectrum. The hologram was held fixed perpendicular to the light path while the detector was swept in  $\theta$  at constant separation distance, and a spectrum was collected at each diffraction angle. An aperture was placed at the front of the hologram to eliminate edge effects. A second aperture was placed in front of the collection fiber to limit the collected angular spread to approximately one degree. Incident illumination from a Xenon arc-lamp solar simulator with a

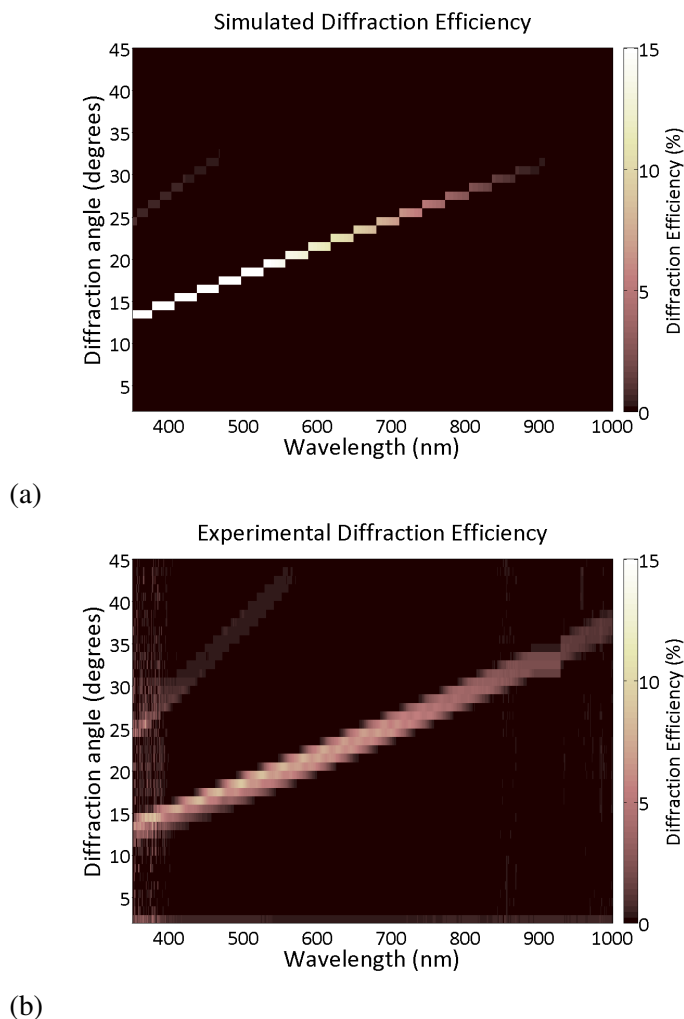


Figure A.3: Diffraction efficiency of a transmission hologram.

divergence half angle of  $1.3^\circ$  was used for experimental characterization, while a collimated beam with incidence angle of  $0.5^\circ$  off-normal was assumed in analytical modeling. Data were simulated and collected in one degree increments.

Diffraction efficiency, the ratio of intensity in a diffracted order to intensity in the incident illumination, is plotted against wavelength and angle for analytical and measured data in Fig. A.3a and b, respectively. The zeroth diffracted order is omitted for clarity. The data show strong qualitative agreement with the first and second diffracted orders occurring at the expected angle throughout the visible region of the spectrum. The trend of reduced diffraction efficiency with increasing wavelength is also consistent between the data. A peak broadening due to the finite size of the collection aperture and the angular spread of the incident beam is observed in the experimental data and accounts for some of the quantitative discrepancy observed

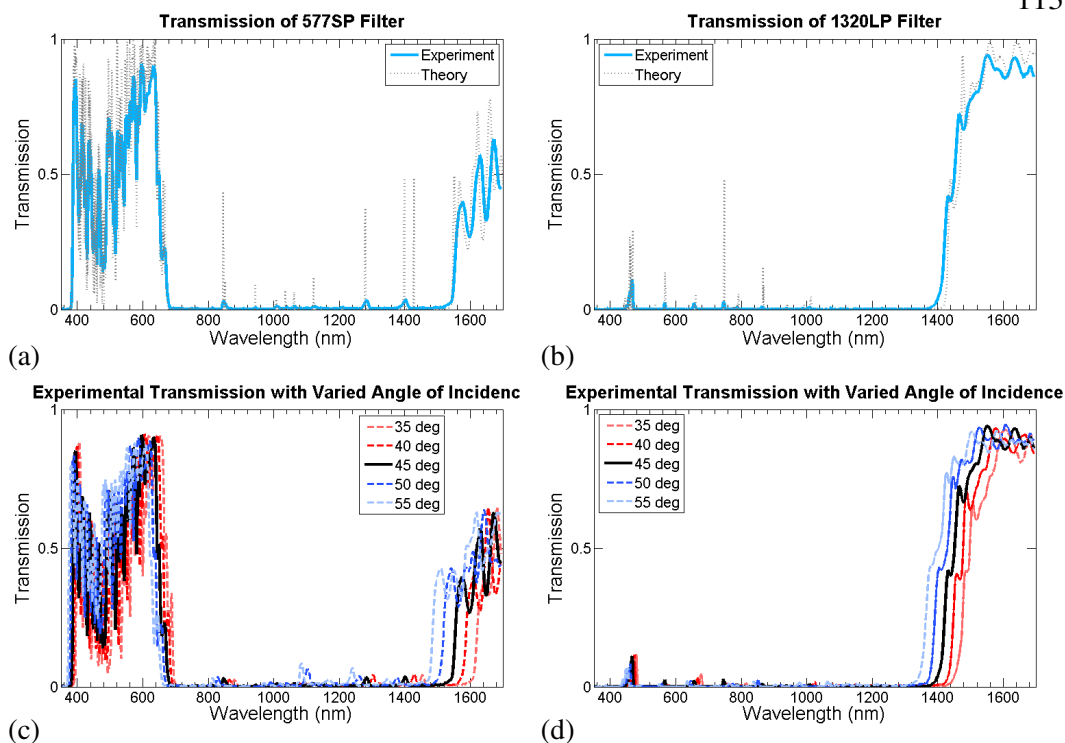


Figure A.4: Theoretical and measured transmission of dichroic filters in air.

between peak diffraction efficiency in the data. Additionally, Fresnel reflections at the front and rear surfaces of the holographic optic and volume UV absorption, not accounted for in the analytical model, account for a portion of the numerical discrepancy between the simulated and experimental data. In spite of this, the data definitively demonstrate the capability for angularly resolved characterization of spectrum splitting optics. Further refinement of the analytical calculation technique to incorporate features present in the experimental system is expected to produce excellent quantitative agreement with the experimental data.

### Dichroic filters

Dichroic filters are an additional optical element of interest for spectrum splitting. One embodiment is shown in Fig. A.2b, wherein individual frequency bands are sequentially transmitted to optimal bandgap subcells as remaining bands are reflected at approximately  $90^\circ$  along the parallelepiped stack. A small amount of concentration is tolerable prior to splitting, while significantly more concentration can be incorporated after the filters. This is due to the transmission mechanism of multilayer dielectric stacks. The band cutoff shift with varying angle of incidence leads to poor performance under illumination with large angular extent.

It is challenging to extend the reflecting band of a shortpass filter out to 1700 nm while maintaining high performance elsewhere in the spectrum. Consequently, a high efficiency longpass filter with a cutoff at 1320 nm first transmits the lowest energy infrared illumination onto a 0.73 eV subcell before short pass filters transmit frequency bands sequentially from high to low energy.

A second configuration of the PIMS was used to characterize the transmitted spectrum as a function of incidence angle for the first two dichroic filters in this optical design. These 1320 nm longpass and 577 nm shortpass filters were designed in-house in collaboration with and fabricated by Chroma Technology. Each filter was mounted to the rotation stage of the PIMS, and variable incidence angle transmission data was obtained at  $45 \pm 10^\circ$  angles of incidence in  $5^\circ$  increments. The detector was held fixed in position during all measurements.

Forty-five degree incidence transmission data for the 1320 nm and 577 nm filters are shown in Fig. A.4a and b, respectively. The filters are designed to be surrounded by a medium with a refractive index of 1.45, but the performance differs substantially when they are characterized in air. Normal incidence air-filter-air transmission is calculated and displayed for comparison. There is strong agreement between peak position in design and experiment, with peak broadening due to the  $1.3^\circ$  divergence half-angle of the illumination source. The 1320 nm filter has a power weighted average transmission of 97.0% in-band and 2.3% out-of-band, in agreement within 4.4% of the theory. The 577 nm filter has a power weighted average transmission of 96.2% in-band and 3.2% out-of-band, in agreement within 4.7% of the theory.

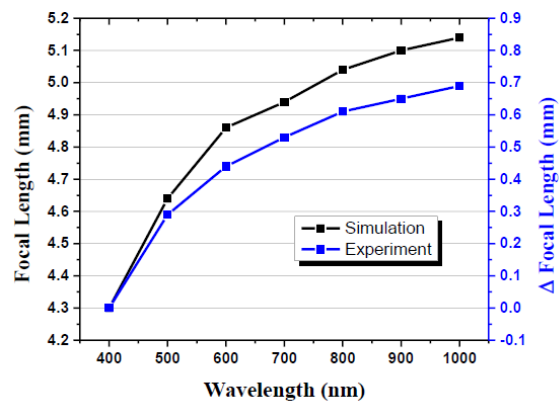
Off-design angle data for the 577 nm shortpass and 1320 nm longpass filters are shown in Fig. A.4c and d, respectively. The transmission band cutoffs blueshift and redshift at greater and lesser angles, respectively, while spectral features remain largely unaffected. This is precisely what would be expected due to the increased phase shift accumulation through each of the filter layers as the angle of incidence increases. The calculated power weighted error with respect to the theory ranges from 3.1-4.7%, in good agreement with the design angle data. This indicates that the filters will perform as calculated off of the design angle as well. Collectively, these data demonstrate the ability to spectrally characterize transmission efficiency from optical elements while varying angle of illumination.

### Aspheric lens

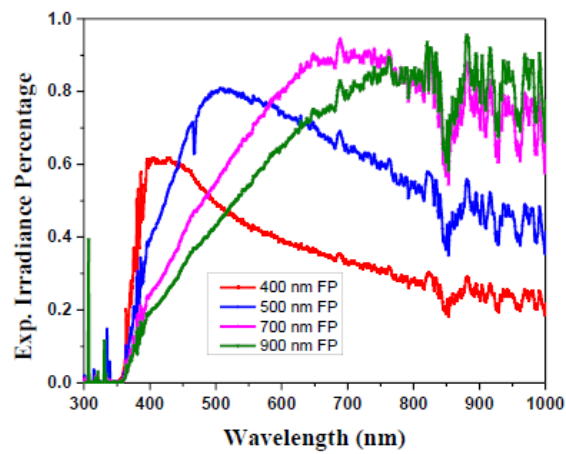
Concentrating optical elements are an essential component of nearly all terrestrial multijunction photovoltaics, including spectrum splitting devices. Imaging optics often suffer from chromatic aberration resulting from refractive index dispersion in the lens material. This phenomenon can be exploited for spectrum splitting by using small subcells separated by the difference in focal lengths between the wavelengths corresponding to the respective bandgaps of the subcells. One configuration utilizing this method of separation is pictured schematically in Fig. A.2c, wherein high and low bandgap cells would be placed in the focal planes of the blue and red light, respectively.

An aspheric lens from Edmund Optics was used as the concentrating optical element. The PIMS was used to characterize the focal length for several wavelengths and the corresponding spectral content at each focal length by scanning an aperture and detector along the  $z$ -axis. The diameters of the aspheric lens and aperture were chosen to be 15 mm and 400  $\mu\text{m}$ , respectively, such that unfocused or defocused wavelengths would not be collected by the optical fiber. Focal lengths from 400-1000 nm in 100 nm increments were determined by maximizing the collected intensity in the spectral window within 10 nm of each desired wavelength. In each case, only the  $z$ -position was adjusted while the  $x$ - and  $y$ -positions and rotation were held fixed.

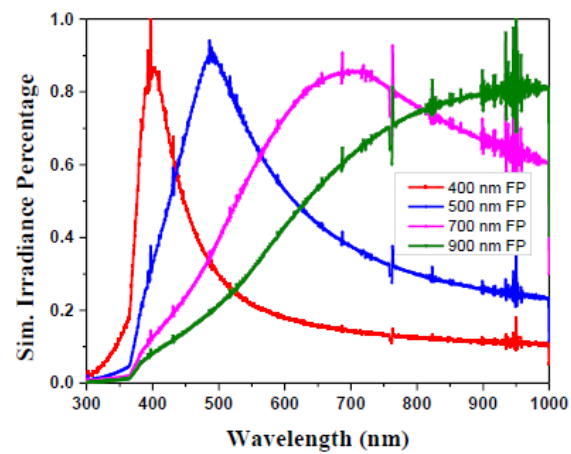
The ray-traced and experimentally measured focal lengths are plotted for each wavelength in Fig. A.5a. Chromatic aberration is more severe at the blue end of the spectrum, as expected from a Cauchy-like material. Spectra collected at each focal point and normalized to the incident spectrum are shown in Fig. A.5b and compared to ray-traced values in Fig. A.5c. The data again show strong qualitative similarity, with close agreement in peak positions. The reduced optical efficiency at the blue end of the spectrum may be partially accounted for by a reduction in transmission efficiency through the optical fiber due to the increased angular spread required for concentration at shorter focal lengths and the approximate  $\cos(\theta)$  transmission of the fiber coupler. Additionally, the discrepancy in the focal length simulation and experimental data suggest a slight angular misalignment of the optic relative to input illumination. Such a misalignment would place the collection aperture at the center of the focal spot for some wavelengths but slightly displaced in the  $xy$ -plane for others, in good agreement with the peak discrepancies observed between the experimental and simulated spectral profiles. These data demonstrate a one-dimensional



(a)



(b)



(c)

Figure A.5: Aspheric lens spectral transmission versus focal length.

spatial-spectral mapping, and analysis of additional optical elements commonly used in the concentrating photovoltaics industry will expand the applicability.

#### **A.4 Conclusions**

The three optical element characterization measurements discussed provide a proof of concept and demonstrate the versatility of a multifunctional optical characterization tool for optics for photovoltaics. Characterization of an integrated optical assembly for concentration or spectrum splitting will require simultaneous mapping of the  $xy$ -plane spatially and angularly varying spectra across each subcell. This necessitates combining linear and rotational movement of the collection fiber. An automated spectrum acquisition and raster of the collection fiber and apertures will be used to determine the spectral intensity distribution across all subcells under the polyhedral spectrum splitting optics. Acquisition of similar intensity distributions over a range of angles of incidence will be performed to facilitate optical component design validation and improvement, optimal AR coating design, and evaluation of other spectrum splitting and concentrating optical systems.